



**MICCAI 2014 BOSTON**



Joint MICCAI-Workshops on  
*Computing and Visualization for Intravascular  
Imaging and  
Computer Assisted Stenting*

MICCAI, 14.September 2014  
Boston, USA

<http://campar.in.tum.de/STENT2014/WebHome>

# Preface

This workshop brings together two very successful MICCAI-Workshop series (CVII and STENT) in order to form a common event on technological and scientific research concerned with endovascular procedures. A continuous communication between surgeons/physicians and scientific and industrial researchers is crucial for bringing forward innovative solutions to the clinics. We aim to provide an interchange platform for medical experts and technological researchers concerned with all aspects of endovascular interventions.

The workshop will focus on imaging, treatment and computed assisted technological advances in diagnostic and intraoperative imaging. Such techniques offer increasingly useful information regarding vascular anatomy and function and are poised to have dramatic impact on the diagnosis, analysis, modeling and treatment of vascular diseases. Computational vision techniques designed to analyze images for modeling, simulating and visualizing anatomy and medical devices such as stents as well as the assessment of interventional procedures are therefore playing an important role and are currently receiving significant interest.

August 2014

Su-Lin Lee  
Stefanie Demirci  
Simone Balocco  
Gozde Unal  
Petia Radeva  
Amin Katouzian  
Maria A. Zuluaga  
Geir Arne Tangen  
Markus Kowarschik

# Workshop Organizers

## **CVII General Chairs**

Gozde Unal, *PhD, Sabanci University, Turkey*

Petia Radeva, *PhD, University of Barcelona, Spain*

Amin Katouzian, *PhD, Technical University of Munich, Germany*

Maria A. Zuluaga, *PhD, University College London, United Kingdom*

## **STENT General Chairs**

Stefanie Demirci, *PhD, Technical University Munich, Germany*

Su-Lin Lee, *PhD, The Hamlyn Centre, Imperial College London, United Kingdom*

Simone Balocco, *PhD, University of Barcelona, Spain*

Geir Arne Tangen, *MSc, SINTEF, Norway*

Markus Kowarschik, *PhD, Siemens Healthcare*

## **Technical Board**

Ying Zhu, *Siemens Corporate Research, USA*

Regis Vaillant, *GE Healthcare, France*

Nenad Filipovic, *University of Kragujevac, Serbia*

Nassir Navab, *PhD, Technical University of Munich, Germany*

Razvan Ionasec, *PhD, Siemens, Germany*

Ignacio Larrabide, *University Pompeu-Fabra, Spain*

Ying Zhu, *Siemens Corporate Research, USA*

Regis Vaillant, *GE Healthcare, France*

Jasjit S. Suri, *Cardiovascular Imaging Division, AtheroPoint, USA*

## **Medical Board**

Hans-Henning Eckstein, *MD, Vascular Surgery, Germany*

Jean Bismuth, *MD, Cardiovascular Surgery, USA*

Adel Malek, *MD, Neurosurgery, USA*

Reza Ghotbi, *MD, Vascular Surgery, Germany*

Colin Bicknell, *MD, Vascular Surgery, London*

Ali Khoynzhad, *MD, PhD, Cedars-Sinai Heart Institute, USA*

## **Publicity Chair**

Tobias Benz, *MSc, Technical University of Munich, Germany*

# Contents

1. **Volume Constraint Denoising of Digital Subtraction Angiography Sequences** 6  
Richard Brosig\*<sup>1</sup>; Markus Kowarschik<sup>2</sup>, Nassir Navab<sup>1</sup>, Maximilian Baust<sup>1</sup>  
<sup>1</sup>Technical University Munich, Germany  
<sup>2</sup>Siemens Healthcare, Germany
2. **Blob enhancement filter for computer-aided diagnosis of cerebral aneurysms** 14  
Tim Jerman\*, Žiga Špiclin, Boštjan Likar, Franjo Pernuš  
University of Ljubljana, Slovenia
3. **X-ray depth maps - Towards improved interventional visualization and beyond** 22  
Wang Xiang<sup>1,2</sup>, Christian Schulte zu Berge<sup>1</sup>, Pascal Fallavollita<sup>1</sup>, Nassir Navab<sup>1</sup>, Stefanie Demirci<sup>1\*</sup>  
<sup>1</sup>Technical University Munich, Germany  
<sup>2</sup>Beihang University, China
4. **Quantitative comparison of plaque in coronary culprit and non-culprit vessel segments using intravascular ultrasound** 28  
Zhi Chen\*<sup>1</sup>, Andreas Wahl<sup>1</sup>, Richard Downe<sup>1</sup>, Shanhui Sun<sup>1</sup>, Tomas Kovarnik<sup>2</sup>, John Lopez<sup>3</sup>, Milan Sonka<sup>1</sup>  
<sup>1</sup>University of Iowa, US  
<sup>2</sup>Charles University, Prague, Czech Republic  
<sup>3</sup>Loyola University Stritch School of Medicine, US
5. **Fully automated detection of healthy wall sections in intracoronary optical coherence tomography** 36  
Guillaume Zahnd\*, Antonios Karanasos, Gijs van Soest, Evelyn Regar, Wiro Niessen, Frank Gijssen, Theo van Walsum  
Erasmus MC, Rotterdam, The Netherlands
6. **Side-branch guided registration of intravascular ultrasound pullbacks in coronary arteries** 44  
Ling Zhang\*<sup>1</sup>, Richard Downe<sup>1</sup>, Zhi Chen<sup>1</sup>, Shanhui Sun<sup>1</sup>, Andreas Wahle<sup>1</sup>, Tatiana Masiarova<sup>1</sup>, Tomas Kovarnik<sup>1</sup>, John Lopez<sup>2</sup>, Milan Sonka<sup>1</sup>  
<sup>1</sup>University of Iowa, US  
<sup>2</sup>Loyola University Stritch School of Medicine, US
7. **Using spatiotemporal patterns of the arterial wall to assist treatment selection for carotid atherosclerosis** 52  
Aimilia Gastouniotti\*, Marinos Prevenios, Konstantina Nikita  
National Technical University of Athens, Greece

8. ***Towards blood flow quantification using dense flow volumes*** 60  
Peter Maday\*<sup>1</sup>, Markus Kowarschik<sup>2</sup>, Nassir Navab<sup>1</sup>, Stefanie Demirci<sup>1</sup>  
<sup>1</sup>*Technical University Munich, Germany*  
<sup>2</sup>*Siemens Healthcare, Germany*
9. ***Higher order tensor-based segmentation and n-furcation modeling of vascular structures*** 68  
Suheyla Cetin\*, Gözde Ünal  
*Sabanci University, Turkey*

# Volume Constraint Denoising of Digital Subtraction Angiography Sequences

Richard Brosig<sup>1</sup>, Markus Kowarschik<sup>2</sup>, Nassir Navab<sup>1</sup>, and Maximilian Baust<sup>1</sup>

<sup>1</sup> Technical University Munich, Germany

{r.brosig,navab,maximilian.baust}@tum.de

<sup>2</sup> Siemens AG, Healthcare Sector, Angiography & Interventional X-Ray Systems

markus.kowarschik@siemens.com

**Abstract.** Digital Subtraction Angiography (DSA) using C-arm systems is a widely used imaging modality for the morphological and functional assessment of human vasculature. As 2D+t DSA sequences typically suffer from noise, the application of denoising algorithms is necessary for subsequent processing, e.g., in order to compute quantitative measures such as the Bolus Arrival Time (BAT). We propose a variational denoising method that accounts for the physics of the image formation process and preserves the injected amount of contrast agent (CA). We also explain how the injected amount of CA can be estimated from the DSA sequence itself and demonstrate the potential of our approach as well as its benefits for the computation of the BAT using synthetic data and phantom experiments with various geometries.

## 1 Introduction

Digital Subtraction Angiography (DSA) using C-arm systems is still one of the most widely used medical imaging techniques for human vasculature with applications ranging from diagnosis over pre-operative planning and intra-operative guidance to post-operative assessment. Current research focuses also on the quantitative study of blood flow parameters, such as the volumetric flow rate [12] or the computation of the bolus arrival time (BAT) [10], which provides an intuitive way of summarizing a DSA sequence in one picture [11]. DSA sequences are, however, relatively noisy, because low-dose X-ray imaging is noisy by nature and the background subtraction even amplifies the noise, which is a well known property of numerical differentiation. As a consequence, the application of noise removal techniques is beneficial for any kind of further processing steps, such as hemodynamic analyses [10], [1], [11]. The goal of this paper is the derivation of a variational denoising method, specifically designed for 2D+t DSA sequences, which is thoroughly motivated from a physical point of view. Thereby, we go beyond the classical approach and consider not only the energy to be minimized, but also the volume preservation of the injected contrast agent (CA). In Sec. 2 we thus introduce a variational framework which includes the proposed volume constraint, a Poissonian noise model, and a carefully chosen regularizer. We further present a numerical solution technique in Sec. 3. Finally, we demonstrate

the potential of our approach using synthetic and phantom data in Sec. 4, where we also demonstrate its benefits for BAT computation.

## 2 The Model

Let  $\Omega \subset \mathbb{R}^2$  denote the two dimensional continuous image domain and  $f_i : \Omega \rightarrow [0, 1]$  ( $i = 0, 1, \dots, N$ ) a sequence of DSA frames. Our goal is to compute a sequence of denoised frames  $u_i : \Omega \rightarrow [0, 1]$  minimizing an energy of the form

$$\sum_{i=0}^N \mathcal{D}(u_i, f_i) + \lambda \mathcal{R}(u_i), \quad (1)$$

where  $\mathcal{D}$  is a data term enforcing the solutions  $u_i$  to be close to the observations  $f_i$  (w.r.t. to a certain metric),  $\mathcal{R}$  is a regularizer ensuring regularity of the solution, and  $\lambda \in [0, \infty)$  is a real positive parameter that allows the user to adjust the trade off between data fidelity and regularity.

### 2.1 Introducing the Volume Constraint

The minimization of (1) can be performed for each frame individually by solving

$$\min_{u_i \in F_i(\Omega)} \mathcal{D}(u_i, f_i) + \lambda \mathcal{R}(u_i), \quad (2)$$

where  $F(\Omega)$  is an appropriate function space, such as the space of square integrable functions  $L^2(\Omega)$ . This canonical formulation is, however, defective in the sense that it is *not volume preserving*. At first, we note that the integral (or sum) of all intensity values in a DSA frame, denoted by  $\bar{f}_i$ , is proportional to the injected amount of CA (assuming no detector saturation), i.e.,

$$\bar{f}_i := \int_{\Omega} f_i(x) dx \propto v_i, \quad (3)$$

where  $v_i$  denotes the total volume injected (and thus visible) in the  $i$ -th frame<sup>3</sup>. Increasing the desired amount of regularity (controlled by  $\lambda$ ) this quantity may not be preserved as demonstrated in Fig. 1(b). The reason is that by increasing  $\lambda$  we trade data fidelity - and thus volume fidelity - for regularity which leads to the observed volume loss. Thus, we propose to incorporate the amount of injected CA by augmenting the function space  $F(\Omega)$  appropriately and choose

$$F_i(\Omega) = \left\{ u \in L^2(\Omega) : \int_{\Omega} u = \bar{f}_i \right\}. \quad (4)$$

It is important to note that incorporating the volume constraint in this way, has the following advantages.

<sup>3</sup> Under the assumption that there is no CA visible in the background frame.

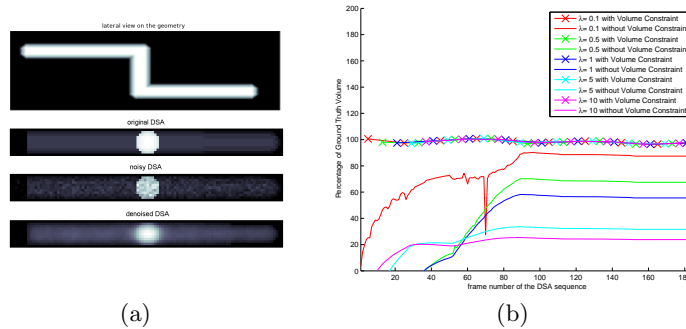


**Fig. 1. Necessity of Volume Preservation** (a) is showing a simulated dataset with a high curvature – from top to bottom: geometry and one frame of simulated DSA (top view), DSA with Poisson noise, denoised DSA, respectively. (b) shows the percentage of the conserved ground truth volume for each image frame and different levels of  $\lambda$  (the plots with volume constraint are indicated with crosses). Especially during the inflow phase (frame 1 to 90), the volume of CA is hardly conserved.

1. By using  $\bar{f}_i$  instead of  $v_i$  we do not require an attenuation calibration in order to estimate the proportionality constant in (3). The practicability of this approach is demonstrated in Fig. 2, where we observe how an automated, constant injection of CA causes an increasing intensity signal  $(\bar{f}_i)_{i=0}^N$  with a slight periodicity superimposed due to pulsatile blood flow.
2. To the best of our knowledge, there is no device or method to measure the amount of CA leaving the field of view. In contrast to this, the proposed estimation technique automatically handles this case, cf. Fig. 2(c).
3. Being incorporated into the function space, the volume constraint can be considered as a hard constraint leading to a projected gradient descent algorithm, cf. Sec. 3 and [8]. It would have been possible to enforce the volume constraint also by adding another energy term in (2), but this would facilitate trading volume fidelity for regularity again.

In Sec. 2.2 and 2.3 we discuss the choice of  $\mathcal{D}$ ,  $\mathcal{R}$  and in order to simplify the notation we will omit the dependency on the frame index  $i$  from now on.

## 2.2 Choosing the Data Term

Typical choices for data terms are smooth  $\ell_2$ -type penalties, such as the one used in the seminal work of Rudin et al. [9], or non-smooth  $\ell_1$ -type penalties, which have been advocated due their robustness w.r.t. outliers, cf. [7] for instance. The main source of noise in X-ray systems is, however, quantum noise which is Poisson distributed, cf. [6]. As Poisson noise is signal dependent, unlike Gaussian noise, it is advisable to employ an adapted data term and we thus use

$$\mathcal{D}(u, f) = \int_{\Omega} u(x) - f(x) \log(u(x)) dx \quad (5)$$

which has been derived by Le et al. [4].

### 2.3 Choosing the Regularizer

The total variation is certainly one of the most widely used as well as extensively studied regularizers for variational problems in computer vision, such as image denoising, segmentation, optical flow, etc. [2]. For denoising angiographic imaging sequences, however, we propose to use a different regularizer. Denoting the three-dimensional concentration of CA in the vessel by  $c$ , its propagation can be modeled by an advection diffusion equation of the form

$$\partial_t c = \nabla \cdot D \nabla c - \nabla \cdot \mathbf{v} c, \quad (6)$$

where  $D$  denotes the diffusivity and  $\mathbf{v}$  the velocity vector field of the flowing blood. Restricting our considerations to a fairly laminar blood flow, which is a quite common assumption for blood flow quantification tasks, cf. [12] and [10], we may assume that  $D$  and  $\mathbf{v}$  are regular enough such that the solution  $c$  at a certain point in time is an element of the Sobolev space  $H^1(\Sigma)$ , cf. [3]. This means that its  $H^1$ -norm is bounded, i.e.,

$$\|c(\cdot, t)\|_{H^1}^2 = \int_{\Sigma} |c(x, t)|^2 dx + \int_{\Sigma} \|\nabla c(x, t)\|_2^2 dx < \infty, \quad (7)$$

where  $\Sigma \subset \mathbb{R}^3$  denotes the volume of interest. In fact, the regularity of the two dimensional DSA frames is actually higher than the one of the CA distribution in three dimensions. The reason is that the image intensity in one image point  $x$  of a DSA frame corresponds to the absorption caused by the CA integrated along the respective ray through  $x$ . As the process of integration can be considered as a smoothing operation - the Radon transformation for an example is known to yield a regularity gain of order  $1/2$  [5] - it is reasonable to enforce that  $u$  has *at least*  $H^1$  regularity, in nearly all geometries. This assumption does not hold at boundaries at hard 90 degree curves along the line of sight, which can be neglected, because, first, this is very rare and second, this is a zero set in the domain. Thus, we choose

$$\mathcal{R}(u) = \int_{\Omega} \|\nabla u(x)\|_2^2 dx \quad (8)$$

as a regularizer which enforces  $u \in H^1(\Omega)$ . Note: The first order term of the norm is the data term itself

## 3 Numerical Solution

Before solving (2) we perform the following two preprocessing steps.

1. It is advisable to employ a segmentation  $\chi : \Omega \rightarrow \{0, 1\}$  of the vasculature which can be obtained via thresholding and post-processing  $U = \sum_{i=0}^N u_i$ ,

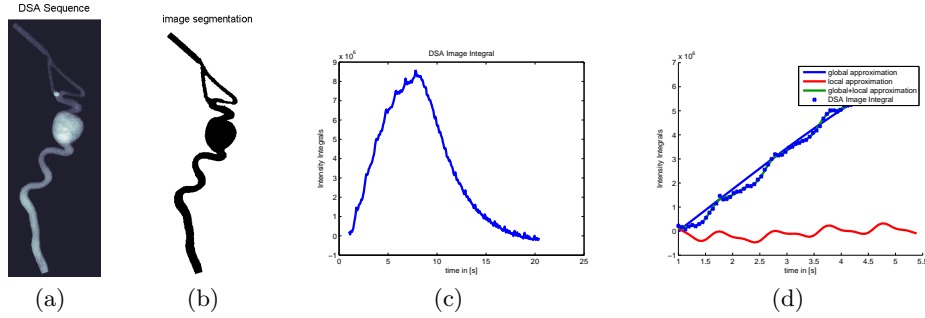


**Fig. 2. Image based Estimation of Iodine Volume** Exemplary DSA frame (a), segmentation  $\chi$  (b), signal of integrated intensity values (w.r.t. segmentation) (c), and (d) fitting of global (blue) and periodical (red) components to this signal yielding the denoised signal  $(\bar{g}_i)_{i=1}^N$  (green) shown during inflow phase.

e.g., by morphological operations. The rationale behind this step is that  $\chi$  can now be used to compute the signal  $(\chi f_i)_{i=0}^N$  which does not contain the background noise, which we do not want to take into account.

2. We further denoise the signal  $(\chi f_i)_{i=0}^N$  as described in Fig.2, because it still contains the noise present in  $\{x : \chi(x) = 1\}$ . This denoising is achieved by fitting a global component modeling the inflow, e.g., a smoothing spline, and a periodical component modeling the effects caused by the pulsatile blood flow, e.g., a linear combination of sine functions, to the data. To simplify the notation, we will denote this denoised signal by  $(\bar{g}_i)_{i=0}^N$  in the following.

Regarding the minimization of (2) we note that the frame-wise energy in (2) as well as the function space  $F$  in (4) are convex, because both the data term and the proposed volume constraint are linear in  $u$  and the regularizer is convex. Thus, we have a convex energy defined on a convex domain which guarantees a global minimum. An obvious way of solving this problem is to perform the projected gradient descent method

$$u^{t+\tau} = \mathbf{P}_F \left[ u^t - \tau \left( \frac{1}{u^t} (u^t - f) - \lambda \Delta u^t \right) \right], \quad (9)$$

where

$$\mathbf{P}_F(u) = u + \frac{\bar{g}_i - \bar{\chi}u}{\bar{\chi}} \cdot \chi, \quad (10)$$

is the projection into the function space  $F$ , cf. [8]. In order to avoid a division by 0, we also normalize  $u^t$  to the range  $[\epsilon, 1]$  with  $\epsilon > 0$  being small.

## 4 Experiments

We validated our method using synthetic and phantom<sup>4</sup> experiments in order to demonstrate the importance of the proposed volume constraint, cf. Sec. 4.1, as

<sup>4</sup> Vascular Simulations LLC <http://www.vascularsimulations.com/>

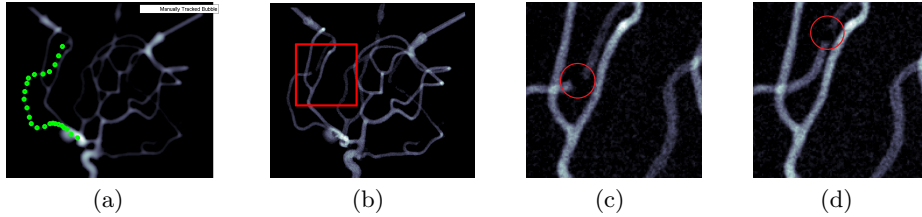


**Fig. 3. BAT Ground Truth Generation** Denoised DSA frame ( $\lambda = 1$ ) with manually tracked locations of the air bubble superimposed (a), noisy DSA frame, with the zoomed region marked (b), close-ups showing indicated air bubble (c) and (d).

well as the potential of our method for the BAT computation, cf. Sec. 4.2 and Sec. 4.3. The runtime, on a recent Mac Book Pro Retina 2013 (Core i7, 2.3GHz) was approximately 1.5 sec. for 100 iterations and a frame size of  $960 \times 400$  using unoptimized MATLAB code. Please note that all figures are best viewed in color.

#### 4.1 Volume Conservation and Denoising Capabilities

We created a synthetic dataset showing the CA propagation in a single curved vessel using an 1D-advection-diffusion simulation, cf. [12], and volume rendering corrupted by Poisson noise, cf. Fig. 1(a). The added Poisson noise is parameter free and only depends on the image intensities [4]. As mentioned in Sec. 2.1, with increasing the amount of regularity (controlled by  $\lambda$ ) the volume is less and less conserved if no volume constraint is employed, cf. Fig. 1(b), which proves the necessity of the proposed volume constraint.

#### 4.2 Quantitative Influence on the Bolus Arrival Time

Generating ground truth for BAT computation in case of non-synthetic experiments is a complicated task. We performed an experiment where CA was injected into a phantom (together with a blood-mimicking fluid) in order to generate a DSA sequence for BAT computation, using the Time To Half Peak approach[10]. Then we created a second sequence where we injected a small air bubble into the vessel of the contrasted phantom. This bubble was then tracked manually to generate a ground truth BAT based on the frame's time stamp (cf. Fig. 3). The comparison of this ground truth to the computed BAT from the noisy as well as the denoised DSA sequence for two different levels of  $\lambda$  can be observed in Fig 4. Please note that all signals in Fig. 4 may have a constant offset, but the mean slope of them should be equal in the ideal case. The offset is neglectable, since surgeons use the *time differences* between two region of interest.

#### 4.3 Qualitative Influence on the Bolus Arrival Time

Besides the quantitative evaluation, we also performed a qualitative comparison. Therefore we created a color coded BAT image computed from a noisy as well as

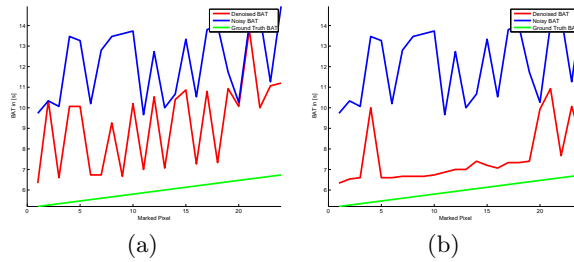


**Fig. 4. Comparison to Ground Truth BAT** BAT of noisy DSA sequence is shown in blue, BAT of denoised DSA sequence is shown in red, extracted ground truth BAT is shown in green for two levels of  $\lambda$  ( $\lambda = 0.1$  in (a) and  $\lambda = 1$  in (b)).

a denoised DSA sequence, as seen in Fig.5(a), and Fig.5(b). By using a bi-plane machine, we can also show, that the computed BAT is quite independent from the projection angle (see Fig.5(c)). In all cases we computed the time-to-half-peak intensity [10] for each pixel. It can be seen that the monotonicity of the BAT in Fig. 5(b) and Fig. 5(c) is clearly preserved in areas with laminar flow (below the aneurysm), while the effect of the turbulent flow on the BAT can still be observed within the aneurysm.

## 5 Discussion and Conclusion

We have proposed a variational method for volume constraint denoising of DSA sequences which is based on a Poissonian noise model and a  $H^1$ -regularizer. Thus, both data term and regularizer account for the physics of the whole image formation process. The advantage of the presented method is that it does not require any additional equipment or specialized protocol. We demonstrated the feasibility of the proposed approach, cf. Fig. 2, as well as its necessity, cf. Fig. 1. Moreover, we conducted several phantom experiments in order evaluate the im-

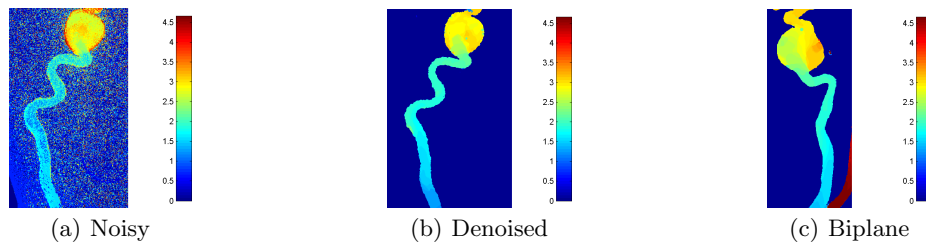


**Fig. 5. Qualitative Comparison of the BAT** Color coded BAT in seconds of a DSA (a), BAT computed from denoised DSA (b), and BAT for the same experiment, but from a different imaging plane (c). Please note that the speckle outside the vessel is removed due to the segmentation  $\chi$ .

pact of our method for quantitative analyses, such as BAT, cf. Fig. 3, Fig. 4, and Fig. 5. It is important to note that the proposed volume constraint is independent of the minimized energy and leads to a soft but physically meaningful temporal coupling without hampering the ability to parallelize the computations regarding individual frames. Although a laminar flow model was considered for the justification of the regularizer, it should also be noted that our approach yields meaningful result in case of turbulent flow, cf. Fig. 5. Future work might include the incorporation of constraints enforcing even stronger temporal consistency, which however has to be done carefully as it might obstruct the possibility to process the individual frames separately. Furthermore experiments has to focus on in-vivo studies where we expect issues in the segmentation task. Accumulation of CA due consecutive scans will be subtracted any how. Also a low SNR sequences should benefit of our method. Furthermore, if there are physically motivated volume constraint, this approach can be extended to other modalities such as MRI or CT.

**Acknowledgment:** We wish to thank Siemens AG, Healthcare Sector, Angiography & Interventional X-Ray Systems, for providing the phantom datasets.

## References

1. Bogunovic, H., Loncaric, S.: Denoising of time-density data in digital subtraction angiography. In: *Image Analysis, Lecture Notes in Computer Science*, vol. 3540, pp. 1157–1166. Springer Berlin Heidelberg (2005)
2. Chambolle, A., Caselles, V., Cremers, D., Novaga, M., Pock, T.: An introduction to total variation for image analysis. In: *Theoretical Foundations and Numerical Methods for Sparse Recovery*. De Gruyter (2010)
3. Fang, W., Ito, K.: Weak solutions for diffusion-convection equations. *Applied Mathematics Letters* 13(3), 69 – 75 (2000)
4. Le, T., Chartrand, R., Asaki, T.: A variational approach to reconstructing images corrupted by poisson noise. *J. of Math. Im. and Vis.* 27(3), 257–263 (2007)
5. Lee, N.Y., Lucier, B.: Wavelet methods for inverting the radon transform with noisy data. *IEEE Trans. on Im. Proc.* 10(1), 79–94 (Jan 2001)
6. MacOvski, A.: *Medical Imaging Systems*. Pearson Education, Limited (1983)
7. Nikolova, M.: Minimizers of cost-functions involving nonsmooth data-fidelity terms. application to the processing of outliers. *SIAM J. on Num. Anal.* 40(3), 965–994 (2002)
8. Oswald, M.R., Toeppe, E., Cremers, D.: Fast and globally optimal single view reconstruction of curved objects. In: *IEEE Conf. on Comp. Vis. and Pat. Rec. (CVPR)*. pp. 534–541. Providence, Rhode Island (Jun 2012)
9. Rudin, L.I., Osher, S., Fatemi, E.: Nonlinear total variation based noise removal algorithms. *Phys. D* 60(1-4), 259–268 (Nov 1992)
10. Shpilfoygel, S.D., Close, R.A., Valentino, D.J., Duckwiler, G.R.: X-ray videodensitometric methods for blood flow and velocity measurement: A critical review of literature. *Med. Phys.* 27(9), 2008–2023 (2000)
11. Strother, C., Bender, F., et al.: Parametric color coding of digital subtraction angiography. *American Journal of Neuroradiology* 31(5), 919–924 (2010)
12. Waechter, I., Bredno, J., Hermans, R., Weese, J., Barratt, D.C., Hawkes, D.J.: Model-based blood flow quantification from rotational angiography. *Med. Im. Anal.* 12(5), 586 – 602 (2008)

# Blob Enhancement Filter for Computer–Aided Diagnosis of Cerebral Aneurysms

Tim Jerman, Žiga Špiclin, Boštjan Likar, and Franjo Pernuš

Faculty of Electrical Engineering, Laboratory of Imaging Technologies,  
University of Ljubljana, Tržaška 25, 1000 Ljubljana, Slovenia

{tim.jerman, ziga.spiclin, bostjan.likar, franjo.pernus}@fe.uni-lj.si

**Abstract.** Several researches have established that the sensitivity of visual assessment of smaller intracranial aneurysms is not satisfactory. Computer–aided diagnosis may shorten visual inspection and increase detection sensitivity by directing a diagnostician to suspicious locations in cerebral vasculature. For detection of blob–like structures, like aneurysms, multiscale enhancement filters, based on eigenvalues of the Hessian matrix, have already been proposed. Their main drawbacks are that they produce nonuniform responses within the structures they are supposed to enhance and that they are rather slow. In this paper, we propose a blob enhancement filter, which can be directly calculated from the Hessian matrix without eigenvalue decomposition. Using two metric functions, we compared the proposed filter with other blob enhancement filters on a synthetic image and on fifteen 3D digitally subtracted angiograms. The response of the proposed filter is more uniform and is computed six times faster than the other filters.

**Keywords:** blob–like structures, cerebral aneurysms, multiscale enhancement filters

## 1 Introduction

Ruptured saccular intracranial aneurysms are the most common cause of non-traumatic subarachnoid hemorrhages causing substantial rates of mortality and morbidity. To prevent such fatal events, cerebral aneurysms should be detected as early as possible from either three–dimensional (3D) X–ray rotational angiography (3D–RA), computed tomography angiography (CTA), or magnetic resonance angiography (MRA) images, and then monitored or treated by endovascular or surgical methods [1]. Although currently the detection of aneurysms is performed visually by experienced neuroradiologists, especially the detection sensitivity of smaller aneurysms is not satisfactory. Enhancement of aneurysm sites in cerebrovascular images may shorten visual inspection and increase detection sensitivity by directing the attention of a diagnostician to suspicious locations in the cerebral vasculature. Image enhancement filters are often used in medical image analysis and visualization to enhance specific normal and pathological structures [9]. For example, vessel enhancement filters [3] are used to

enhance and visualize angiograms, while blob enhancement filters [8, 5] are used to enhance and facilitate the detection of potentially malignant nodular structures, i.e. lung nodules [9] and colon polyps. Enhancing the structures of interest may significantly reduce the valuable time that a clinician spends to effectively inspect a 3D medical image and decreases the possibility that small but important structures will be missed [9, 1]. In this paper, we focused on the problem of better enhancing blob-like structures in 3D cerebral angiograms with the aim to facilitate better detection of especially small intracranial aneurysms.

The two major limitations of current blob-enhancement filters are 1) their nonuniform response within spherical, blob-like regions, which may hamper detection of such structures and 2) their computational complexity, for which they cannot be used for real-time image visualization [9]. Therefore, a computationally more efficient blob enhancement filter is needed that would also be more robust to the variability of the structures it is aimed to enhance. In this paper, we propose a 3D multiscale blob enhancement filter, which is based on the analysis of 2nd order image intensity derivatives [3]. The proposed blob enhancement filter was quantitatively evaluated using a synthetic image and 15 cerebral angiograms of patients with aneurysms. In comparison to several other blob enhancement filters, the proposed filter had a nearly uniform response within the blob-like structures, such as the aneurysms, and its fast computation enabled real-time visualization of the enhanced images.

## 2 Background

Enhancement filters are scalar functions, which selectively amplify a certain local intensity profile or structure in an image. A large class of enhancement filters [4, 6, 3, 8, 5] is based on multiscale analysis of 2nd order image intensity derivatives. Let  $I(\mathbf{x})$  denote the 3D image intensities at coordinates  $\mathbf{x} = [x_1, x_2, x_3]^T$ . The  $3 \times 3$  Hessian matrix  $\mathcal{H}_{ij}(\mathbf{x}, s)$  of 2nd order derivatives of  $I(\mathbf{x})$  at scale  $s$  is defined as:

$$\mathcal{H}_{ij}(\mathbf{x}, s) = s^2 I(\mathbf{x}) * \frac{\partial^2}{\partial x_i \partial x_j} G(\mathbf{x}, s) \quad \text{for } i, j = 1, 2, 3, \quad (1)$$

where  $G(\mathbf{x}, s) = (2\pi s^2)^{-3/2} \exp(-\mathbf{x}^T \mathbf{x} / 2s^2)$  is a 3D Gaussian and  $*$  denotes convolution.

Enhancement of structures of specific shapes, e.g. spherical, elongated or planar, is based on the analysis of eigenvalues of the Hessian matrix  $\mathcal{H}$ . Let the three eigenvalues  $\lambda_1, \lambda_2, \lambda_3$  of  $\mathcal{H}$  be sorted according to their magnitude:  $|\lambda_1| \leq |\lambda_2| \leq |\lambda_3|$ . For spherical, blob-like structures all the eigenvalues have a high, equally signed and isotropic magnitude ( $\lambda_1 \approx \lambda_2 \approx \lambda_3 \wedge |\lambda_{1,2,3}| \gg 0$ ), whereas positive (negative) eigenvalues indicate a dark (bright) structure on a bright (dark) background. Elongated, tubular and planar structures, for example, exhibit distinctly different Hessian eigenvalue relations [3]. The eigenvalue relations for blob-like structures (or blobness) at scale  $s$  can be indicated by

several different functions  $\mathcal{B}(s) = f(\lambda_1, \lambda_2, \lambda_3)$ . Four existing blobness functions are reviewed next.

As part of a vessel enhancement filter [3], Frangi *et al.* introduced the first blobness measure  $\mathcal{R}_B = |\lambda_1|/\sqrt{|\lambda_2\lambda_3|}$  so as to suppress blob-like structures. Frangi's vesselness function [3] can be modified into a blobness function as:

$$\mathcal{B}_F(s) = \begin{cases} \left(1 - \exp\left(-\frac{\mathcal{R}_B^2}{2\beta^2}\right)\right) \left(1 - \exp\left(-\frac{\mathcal{S}^2}{2\delta^2}\right)\right) & \text{if } \lambda_3 \leq \lambda_2 \leq \lambda_1 < 0, \\ 0 & \text{otherwise,} \end{cases} \quad (2)$$

where  $\mathcal{S} = \sqrt{\lambda_1^2 + \lambda_2^2 + \lambda_3^2}$  is a 2nd order structurness measure, which distinguishes between structured and uniform regions in the image. Parameters  $\beta$  and  $\delta$  control the sensitivity of measures  $\mathcal{R}_B$  and  $\mathcal{S}$  [3].

Sato *et al.* [8] proposed a blobness function that employed only the largest and smallest of the three eigenvalues:

$$\mathcal{B}_S(s) = \begin{cases} |\lambda_3| \left(\frac{\lambda_1}{\lambda_3}\right)^\gamma & \text{if } \lambda_3 \leq \lambda_2 \leq \lambda_1 < 0, \\ 0 & \text{otherwise.} \end{cases} \quad (3)$$

Parameter  $\gamma$  controls the sensitivity to blobness and is typically set either to 0.5 or 1, which simplifies (3) to  $\sqrt{\lambda_3\lambda_1}$  and  $|\lambda_1|$ , respectively. Li *et al.* [5] proposed a similar blobness function:

$$\mathcal{B}_L(s) = \begin{cases} \frac{|\lambda_1|^2}{|\lambda_3|} & \text{if } \lambda_3 \leq \lambda_2 \leq \lambda_1 < 0, \\ 0 & \text{otherwise,} \end{cases} \quad (4)$$

which can be conceptually split into two factors:  $\lambda_1$  and  $\lambda_1/\lambda_3$ . The first factor represents the magnitude of the blobness function, while the second term represents the likelihood that a voxel is part of a spherical structure.

Multiscale filter responses are obtained by computing a given blobness function  $\mathcal{B}$  for each voxel  $\mathbf{x}$  and over a range of different scales  $s$  ( $s_{min} < s < s_{max}$ ) and taking the maximal value [3], i.e.:

$$\mathcal{B}(\mathbf{x}) = \max_{s_{min} \leq s \leq s_{max}} \mathcal{B}(\mathbf{x}, s). \quad (5)$$

The values of  $s_{min}$  and  $s_{max}$  are selected according to the minimal and maximal expected sizes of a structure of interest.

All the aforementioned blobness functions are proportional to the magnitude of  $\lambda_1$ , however, their response is typically not uniform throughout a spherical structure. For example,  $|\lambda_1|$  usually peaks at the center of a spherical structure and then progressively decreases towards the structure's periphery. This was, therefore, our motivation to devise a blobness function that would give a much more uniform response inside a blob-like structure.

### 3 Proposed Blobness Function

Several measures of structural isotropy and anisotropy have been proposed for characterization of diffusion tensors [7], which can also be used to indicate spherical structures based on multiscale Hessian analysis. We consider the following

blobness function:

$$\mathcal{B}_P(s) = \begin{cases} \lambda_1 \lambda_2 \lambda_3 \left( \frac{3}{\lambda_1 + \lambda_2 + \lambda_3} \right)^3 & \text{if } \lambda_3 \leq \lambda_2 \leq \lambda_1 < 0, \\ 0 & \text{otherwise.} \end{cases} \quad (6)$$

In a geometrical interpretation, (6) is a volume ratio [7] between an ellipsoid, with semi-axes  $\lambda_1$ ,  $\lambda_2$ ,  $\lambda_3$ , and a sphere, with radius equal to the mean of the three eigenvalues. For a spherical structure (isotropic eigenvalues) the volume ratio has value one and with increasing non-sphericity (anisotropic eigenvalues) decreases towards zero.

Considering the expressions for computing the determinant and trace of the Hessian matrix, i.e.  $\det(\mathcal{H}) = \prod_i \lambda_i$  and  $\text{Tr}(\mathcal{H}) = \sum_i \lambda_i$ , respectively, we introduce a modified and computationally very efficient blobness function:

$$\mathcal{B}_P(s) = \begin{cases} [27 \cdot \det(\mathcal{H}) \cdot \text{Tr}(\mathcal{H})^{-3}]^\gamma & \text{if } \det(\mathcal{H}) < 0 \text{ and } \text{Tr}(\mathcal{H}) < \tau, \\ 0 & \text{otherwise,} \end{cases} \quad (7)$$

where  $\tau$  is a cutoff threshold and  $\gamma \geq 1$  is used for nonlinear scaling of the response. The purpose of constraints  $\det(\mathcal{H}) < 0$  and  $\text{Tr}(\mathcal{H}) < \tau$  is to cutoff the response of  $\mathcal{B}_P(s)$  for  $\lambda_i \geq 0, i = 1, 2, 3$ . However, cases with  $\lambda_{1,2} \geq 0$  and  $\lambda_3 < 0$  may surpass the above constraints. As spherical structures exhibit isotropic, high magnitude eigenvalues ( $\lambda_{1,2,3} \ll 0$ ), the magnitude of  $\tau$  should be set high enough, for example  $\tau = 0.25 \cdot \min \text{Tr}(\mathcal{H})$ , to reliably cutoff such false responses and responses due to noise (equal and small magnitude eigenvalues).

Individual eigenvalue responses peak in the center of a blob and decrease progressively towards the structure's periphery. As the proposed blobness function is based on the ratio between the magnitudes of eigenvalues, it responds equally in the center where the magnitudes are high and at the periphery where the magnitudes are small, resulting in a uniform response throughout the structure.

## 4 Experiment and Results

The performance of the proposed (7), Frangi's [3] (2), two variants of Sato's [8], i.e. (3) for  $\gamma = 0.5$  and  $\lambda_1$  for  $\gamma = 1$ , and Li's [5] (4) blobness functions were evaluated and compared on a synthetic image containing blob-like structures and on 15 cerebral angiograms of patients with aneurysms.

**Image Datasets and Experiment Setup.** A synthetic image (Fig. 1) was created that included structures simulating those to be expected in cerebrovascular images: vessels, vessel bifurcations, and aneurysms of varying size and location. The structures coded in yellow in the synthetic image (Fig. 1) were the structures targeted by the enhancement filters. To study the influence of noise on the response of the tested blobness functions, a varying amount of Poisson noise  $\eta_P$  was added to the synthetic image  $I(\mathbf{x})$ . Several noisy realizations of the

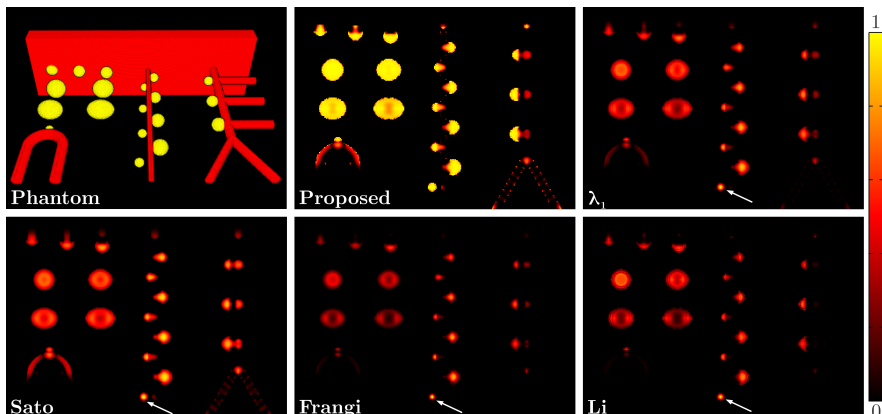


**Fig. 1.** 3D synthetic image and medial cross-sections through the normalized responses obtained by the proposed,  $\lambda_1$ , Sato [8], Frangi [3], and Li [5] filters. The proposed filter had a maximal response within several blob structures, while the arrows in other filter responses indicate the location of the maximal response.

image were obtained as  $I(\mathbf{x}, \eta_P) = \eta_P V_P(\mathbf{x}) + (1 - \eta_P)I(\mathbf{x})$ , where  $V_P(\mathbf{x})$  is a normalized image of a realization of Poisson noise, which is the noise associated with X-ray sources. Responses of enhancement filter based on the tested blobness functions were computed for  $\eta_P$  in the range from 0 (noiseless) to 1, and by maximizing the response over a range of scales (5). As the range of the proposed blobness function values is  $[0, 1]$ , the values of other functions were normalized to this range. The average noise levels on real images would normally not exceed values of  $\eta_P = 0.3$ .

Cerebral 3D digitally subtracted angiograms (3D-DSA) were acquired by a Siemens Axiom Artis dBA angiography system. Fifteen patients were imaged and each had one or more aneurysms of different sizes. The sizes ranged from 4 to 11 mm, with the majority in the range 4–6 mm. The 3D-DSA images had  $512 \times 512 \times 391$  voxels with isotropic spacing of 0.46 mm. A volume of interest (VOI) of  $200 \times 200 \times 200$  voxels was manually selected such that most of the cerebral vasculature and all the aneurysms were within a VOI. Aneurysms were manually segmented by an expert, and the obtained reference segmentations were used to quantify the performance of enhancement filters. Filter responses for all images were obtained by maximizing the response of blobness functions over scales  $s$  ranging from 0.5 to 2.5 mm with a step size of 0.5 mm.

**Evaluation criteria.** The efficacy to enhance synthetic or aneurysm blob-like structures was quantified by evaluating segmentation performance using receiver operating characteristics (ROC) analysis and by quantifying the uniformity using the median of the response distribution inside the segmented aneurysms. As the test images contained small structures and most voxels represented the background, ROC analysis was based on precision–recall curves [2]. To quantify

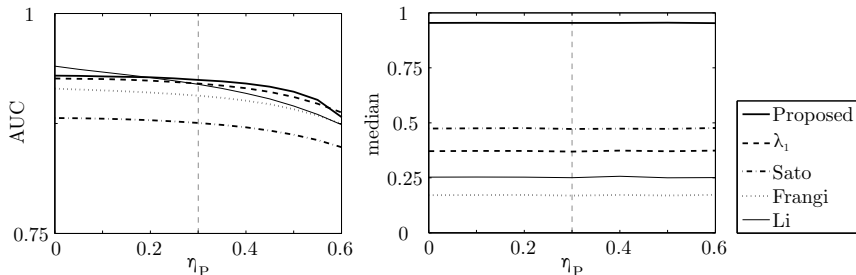


**Fig. 2.** Area under the precision–recall curve (*left*) and median of the response inside the aneurysm (*right*) with respect to noise level  $\eta_P$  added to the synthetic image. A vertical line indicates the average noise levels  $\eta_P$  on the real dataset images.

the segmentation potential of a filter, precision and recall were computed, and then the area under the precision–recall curve (AUC) was computed. Values of AUC are between zero and one, with values closer to one indicating a better correspondence between the filter response and reference segmentation.

The uniformity of the filter responses was assessed using the median (MedR) of the response within the reference segmentation. All filter responses were normalized to the range 0 to 1. A higher MedR indicates a more compact distribution of response values around the maximal value and thus a more uniform response.

**Results.** The 3D synthetic image and medial cross–sections of the 3D synthetic image enhanced with the proposed,  $\lambda_1$ , Sato’s, Li’s, Frangi’s blobness functions are presented in Fig. 1. The proposed blobness function gave the highest response, which was also quite uniform throughout the blob–like structures, irrespective of the size and shape of nearby structures. The application of other filters resulted in less uniform responses within the blob–like structures, with the highest response occurring in the centers. For ellipsoidal (nearly spherical) structures the  $\lambda_1$ , Li’s and Frangi’s blobness functions had a distinctly lower response in the ellipsoid’s center as compared to the proposed and Sato’s blobness functions. The AUC and MedR values as the function of added amount of Poisson noise  $\eta_P$  in the range 0 to 0.6 (twice the value of real images) are shown in Fig. 2. The values of AUC and MedR in the presented range are quite constant. According to the results presented in Fig. 2, the proposed filter achieved consistently achieved the highest MedR (and a large AUC), which is related to the most uniform response within blob–like structures (Fig. 1).

For the 15 filtered real 3D–DSA images, AUC and MedR values and computational times are given in Table 1. Here too, the proposed blobness function achieved the larger mean AUC and highest mean MedR. Computation times for the blobness functions reported in Table 1 were obtained using a CUDA implementation on a NVIDIA 650M GPU. Since eigenvalue decomposition of the Hessian matrix was not required to compute the proposed blobness function,

**Table 1.** The mean and standard deviation of AUC and MedR, and mean computation times for different blobness function. Values marked with \* are significantly lower ( $P < 0.05$ ) than the proposed filter values according to the Wilcoxon signed-rank test.

Filter	AUC (MEAN $\pm$ STD)	MedR (MEAN $\pm$ STD)	Time [s]
Proposed	0.26 $\pm$ 0.20	0.73 $\pm$ 0.17	1.3
Frangi	*0.19 $\pm$ 0.16	*0.20 $\pm$ 0.08	8.8
Sato	*0.16 $\pm$ 0.15	*0.49 $\pm$ 0.10	9.0
Li	0.24 $\pm$ 0.19	*0.22 $\pm$ 0.11	8.7
$\lambda_1$	0.21 $\pm$ 0.18	*0.40 $\pm$ 0.11	8.6

its computation time was at least six times faster compared to the other tested blobness functions.

## 5 Discussion and Conclusion

In this paper, we proposed a blobness function that can be used to enhance blob-like structures like aneurysms. The proposed blobness function (7) is based on volume ratio, a tensor anisotropy measure frequently used in diffusion tensor analysis [7]. A synthetic image and 15 cerebral 3D-DSA images of patients with manually segmented aneurysms were used to quantitatively evaluate the proposed and several other blobness functions. The enhancement of the targeted blob-like structures was quantified by evaluating segmentations using ROC analysis and by quantifying the uniformity using the median of the distribution inside the manually segmented aneurysms. The proposed blobness function showed improved performance over other blobness functions as it achieved a slightly larger AUC and a consistently much higher MedR. The main advantage of the proposed blobness function is reflected in its highly uniform response within the blob-like regions as seen in Fig. 1. The method has one parameter, which controls the response uniformity and the number false positives in it. For a highly uniform response also the amount of false positives is higher, which can be seen as a disadvantage. However, the balance between the uniformity and the number of false positives can be adjusted using the introduced filter parameter.

Detection of small blob-like structures in a 3D volume is often difficult even with advanced image segmentation and visualization tools. For example, in patients with cerebral aneurysms, the small aneurysms may not be segmented and thus impossible to visualize. Moreover, complex cerebral vasculature might occlude small aneurysms, thus careful manipulation of the viewing angle is required. If the blob-like structures such as small aneurysms are enhanced w.r.t. other structures, they can be immediately visualized. The proposed blobness function is computed very fast (six times faster than other blobness function) and enables real-time visualization of (small) aneurysms (Fig. 3). While some other filters have less false positives, the detection of small aneurysms is impaired by the loss of uniformity and thus loss of shape information. In the future the proposed filter could also be used for enhanced visualization of lung nodules and colon polyps.

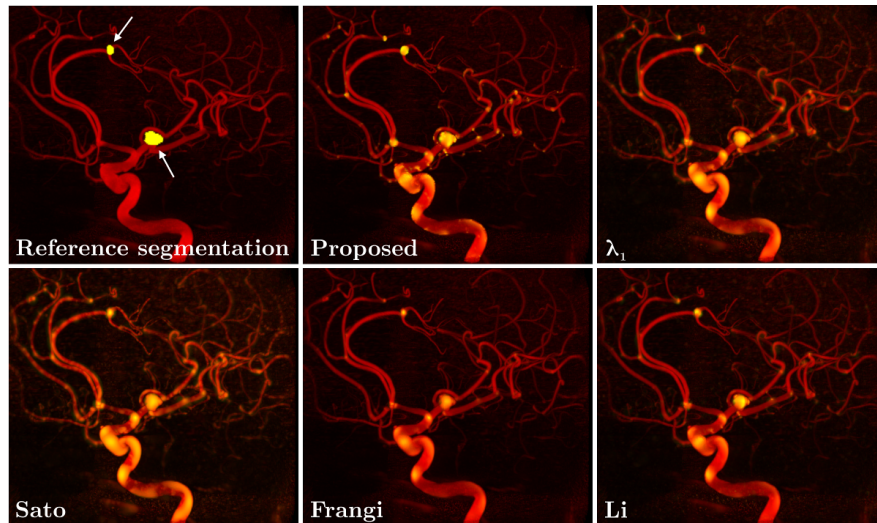


**Fig. 3.** Maximum intensity projections of a 3D-DSA with superimposed responses of the proposed ( $\gamma = 3$ ),  $\lambda_1$ , Sato [8], Frangi [3], and Li [5] blob enhancement filters. The two aneurysms are indicated by arrows.

## References

1. Brisman, Jonathan L. and Song, Joon K. and Newell, David W.: Cerebral Aneurysms. *New England Journal of Medicine*, 355(9), 928 – 939 (2006)
2. Fawcett, T.: An introduction to ROC analysis. *Pattern Recognition Letters* 27(8), 861 – 874 (2006)
3. Frangi, A., Niessen, W., Vincken, K., Viergever, M.: Multiscale vessel enhancement filtering. In: *MICCAI'98, LNCS*, vol. 1496, pp. 130–137 (1998)
4. Koller, T., Gerig, G., Szekely, G., Dettwiler, D.: Multiscale detection of curvilinear structures in 2-D and 3-D image data. In: *ICCV'95*, pp. 864–869 (1995)
5. Li, Q., Sone, S., Doi, K.: Selective enhancement filters for nodules, vessels, and airway walls in two- and three-dimensional CT scans. *Medical Physics*, 30(8), 2040–2051 (2003)
6. Lorenz, C., Carlsen, I.C., Buzug, T., Fassnacht, C., Weese, J.: A multi-scale line filter with automatic scale selection based on the Hessian matrix for medical image segmentation. In: *Scale-Space Theory in Computer Vision, LNCS*, vol. 1252, pp. 152–163. (1997)
7. Pierpaoli, C., Mattiello, J., Di Chiro, G., Le Bihan, D., Basser, P.J.: Diffusion tensor imaging of brain white matter anisotropy. *Proceedings of the International Society for Magnetic Resonance in Medicine*, 1994(S2), 1038 (1994)
8. Sato Y., et al.: Tissue classification based on 3D local intensity structures for volume rendering. *IEEE Transactions on Visualization and Computer Graphics*, 6(2), 160–180 (2000)
9. Wiemker, R., Dharaiya, E.D., Bülow, T.: Informatics in radiology: Hesse rendering for computer-aided visualization and analysis of anomalies at chest CT and breast MR imaging. *RadioGraphics*, 32(1), 289–304 (2012)

# X-ray Depth Maps - Towards Improved Interventional Visualization and Beyond

Xiang Wang<sup>1,2</sup>, Christian Schulte-zu-Berge<sup>1</sup>, Pascal Fallavollita<sup>1</sup>, Nassir Navab<sup>1</sup>, and Stefanie Demirci<sup>1</sup>

<sup>1</sup> Computer Aided Medical Procedures, Technische Universität München, Germany, `{christian.szb,fallavol,navab,demirci}@in.tum.de`,

<sup>2</sup> School of Automation Science and Electrical Engineering, Beihang University, China, `wangxiang8602@126.com`

**Abstract.** Correct depth perception is crucial for navigation and device positioning tasks in clinical interventions. Yet, many minimally-invasive interventions, such as catheterizations, are usually performed under 2D X-Ray Fluoroscopic and Angiographic guidance only. Previous attempts to integrate pre-operative 3D data of the patient by registering these to intra-operative data have led to virtual 3D renderings independent of the original X-ray appearance and planar 2D color overlays (e.g. roadmaps). Inspired by a recent introduction of improved X-ray visualization, this paper presents a novel technique to create depth maps for interventional X-ray images. Assuming a patient-specific pre-operative 3D scan to be aligned with an interventional image of the same patient, our method employs GPU ray casting together with a novel gradient magnitude based transfer function to yield a 2D range image of the anatomy. The accuracy of X-ray Depth Maps was tested and analysed for three relevant clinical scenarios covering different anatomical aspects and targeting different levels of interventional expertise. Therefore, original 3D distances in between apparent anatomical landmarks have been compared to respective values extracted from corresponding X-ray Depth Maps.

## 1 Introduction

The replacement of conventional open surgery with minimally-invasive techniques for various diseases have had dramatic impact on patient survival rate. However, this development has also increased the importance of intraoperative imaging guidance that involves harmful ionizing radiation (X-ray) in particular for endovascular interventions where catheters and guide wires are inserted into the patient's vascularity in order to treat cardiovascular diseases. Though providing fast and reliable anatomy information in decent resolution, the harmful side effects of ionizing radiation (X-ray) and contrast agents (vessel highlighting) affect both patients and surgical team. Despite the latest findings in intra-operative 3D cone beam CT (CBCT) reconstructions, 2D X-ray Fluoroscopy and Angiography is still the state-of-the-art interventional imaging modality for catheterization procedures. The missing depth information due to the 2D nature

of these image sequences, is compensated by the interventionalist acquiring multiple X-ray sequences from varying angulations and then mentally recovering the 3D information. This yields an increase in radiation and use of contrast agent likewise, as vessels need to be made visible within the X-ray images.

Improved and adapted visualization of X-Ray images has received very little attention in clinical practice as well as in the medical and technological research community. Apart from some very recent work on *Colored X-rays* [10, 1], the loss of 3D information during medical interventions has mostly been addressed in terms of 2D-3D image registration. Here, an interventional 2D X-ray image is aligned with the pre-operatively acquired 3D data (i.e. CT or MRI) of the patient [7]. Yet, the output of such algorithms is a projection matrix that, by itself, does not yield any meaningful visualization. In most cases, such registration algorithms are used as an intermediate step for locating interventional devices and instruments and showing their positions within a 3D rendering of the patient, or for volume reconstruction if several 2D X-ray images from varying viewpoints are available.

In this paper, we present the novel concept of X-ray Depth Maps. Assuming a pre-operative 3D patient data being registered to the current interventional 2D image, our method employs a novel volume rendering technique with a single transfer function to yield projections with depth encoded intensity representation. Besides facilitating depth-enhanced visualization during minimally invasive procedures, X-ray Depth Maps provides a variety of possibilities ranging from specific distance measurements to constraints for ill-posed image-guided interventions concepts.

The remainder of the paper is organized as follows: In section 2, we introduce the framework of our methodology and give details in various subsections. Our performed evaluations and experiments are explained and systematically discussed within section 3. Finally the paper is concluded and ideas for future work are presented in section 4.

## 2 Methodology

Assuming the pre-operative 3D patient to be optimally aligned to the current interventional X-ray image, we propose a depth rendering scheme to yield a corresponding X-ray Depth Map. The details of this compositing will be described in the remainder of this sections. Although not within the focus of this paper, we will give more details on available 2D-3D registration methods to align pre- and intra-operative images, within section 3.

### 2.1 Simulation of X-ray Images

The concept of *Digitally Reconstructed Radiographs* (DRR) essentially describes the digital simulation of X-ray images.

## 2.2 Depth Composition

In volume rendering, the compositing scheme specifies the accumulation of individual contributions from the sample points along the ray through a volume [8]. Two existing depth compositing schemes can be found in the literature. Aichert et al. [1] proposed a volume rendering employing a 2D depth-intensity-based transfer function that encodes depth in color during rendering of an emission-only model (depth integral method). The transfer function was decoupled into two 1D transfer functions - one for the mapping from depth to color and one for the mapping of the voxel values to the corresponding intensity (the standard DRR transfer function). Along the casting ray, the two transfer functions were multiplied and yielded a weighted accumulation of the different colors along the ray. Second, another depth compositing scheme is represented by maximum intensity projection (MIP), which acquires the maximum contribution along the ray. It is mainly used for virtual angiography - the display of vessel structures in medical images [6, 5, 9].

Figure 3 depicts the differences and drawbacks of the mentioned existing schemes. It can be clearly seen in Figure 3(a) that depth integral causes a merging of depth where different tissues overlap. In locations outlined by two circles (yellow and green), where skull and vessel overlap, a new hue - indigo has appeared, which is a combination of blue and violet. No matter which tissue is in front, the combined hue will not change. It only relates to the transfer function result of these tissues. This can be also deduced from the mathematical operation of depth integration. Figure 3(b) shows the rendering result of colored DRR using MIP compositing. Although it gives clear cues to perceive depth, there are misleading occlusions, which have been outlined by three circles (cyan, yellow, green). In locations where skull and vessels overlap, the depth color of skull is shown, since the intensity of bone is bigger than that of vessels (yellow and green circles). However, these vessels are in fact located in front of this particular skull part, since in the presented color space, objects colored in purple are nearer to the observer than blue colored structures. The cyan circle shows an example of false vessel overlap. Because purple is nearer than violet, the vessel colored in violet should be occluded by vessel colored in purple. However, due to different intensity distribution (the original intensity of the violet vessel is higher than that of the purple vessel), the colored DRR shows the violet vessel. As stated by Ware [27], occlusion is probably the strongest cue for depth perception. Thus, it is difficult for the observers to correct wrong occlusion by color cues. Hence, depth compositing by MIP usually gives a false depth intuition. In order to obtain a legible, lucid and intuitive colored DRR, we propose a gradient-based depth compositing scheme, which uses gradient values of the transfer function to obtain material boundaries: (2) The term  $Z(D)$  is the depth compositing result through the process of ray casting (enter the volume at position  $s = 0$  and leave the volume at  $s = D$ ),  $TF$  represents the transfer function and  $t$  is a given threshold for gradient. We choose this compositing scheme mainly for two reasons. In general, people observe distance or depth information of an object by the reflectance of light from the object surface, in addition to the principal

of binocular vision. Hence, people are more sensitive to edges formed between different objects. There are various tissues in human body with different densities and the transfer function can separate these and assign them to ranges of values in the source data that correspond to features of interest. Thus, with the gradient of transfer function along a ray, we can obtain material boundaries between different tissues. Second, a specific threshold  $t$  is introduced to control specific boundary selections. Assuming that vessels have higher intensity curvature than bone, bone in front of vessels will be shown with a lower threshold. In contrast, bone can be ignored using a higher threshold. It can be seen in Figure 3(c) that our proposed method is able to correct the occlusion of overlapping tissues. Compared to render results of existing methods, parts of the skull are occluded by front vessels (yellow and green circles). Also the purple vessel shown within the cyan circle now correctly occludes the violet vessel.

### 2.3 Rendering

## 3 Experiments & Results

### 3.1 Setup & Preparation

The first step in our framework consists in aligning a corresponding 3D patient volume acquired prior to the intervention (CT or MRI), to the current interventional X-ray image. 2D/3D registration has been subject of many research initiatives and the reader is referred to Markelj et al. [7] for a complete overview. One common approach is intensity-based image registration where the alignment of a 3D volume  $V$  and a 2D image  $I$  is performed via

$$\hat{\mathbf{P}} = \arg \max_{\mathbf{P}} \mathcal{S}(\mathbf{P} \circ V, I) \quad (1)$$

where  $\mathbf{P} = K[R|t]$  presents a projective transformation combining the 6-DOF extrinsic parameters rotation  $R$  and translation  $t$  and the 4-DOF intrinsic imaging parameters  $K$ . The projection of the 3D volume (denoted by delimiter  $\circ$ ) is generally realized via the concept of digitally reconstructed radiographs (DRR). Essentially, this describes a virtual simulation of an X-ray by ray casting employing a single render pass to map CT Hounsfield units to X-ray attenuation values. As shown by previous works, this concept can be implemented efficiently using GPU computing power. We aim at registering interventional images that may introduce outliers such as image dissimilarities induced by medical instruments that are not present in the pre-operative 3D data, or by the varying presence of injected contrast agent. Hence, we opted for an approach combining disocclusion-based registration [2] and DRR masking [3]. For registering a contrasted pre-operative patient volume to a non-contrasted X-ray fluoroscopy image, a segmentation of the contrasted vessel within the preoperative volume is obtained by using readily available tools such as ITK-SNAP<sup>3</sup>. During DRR

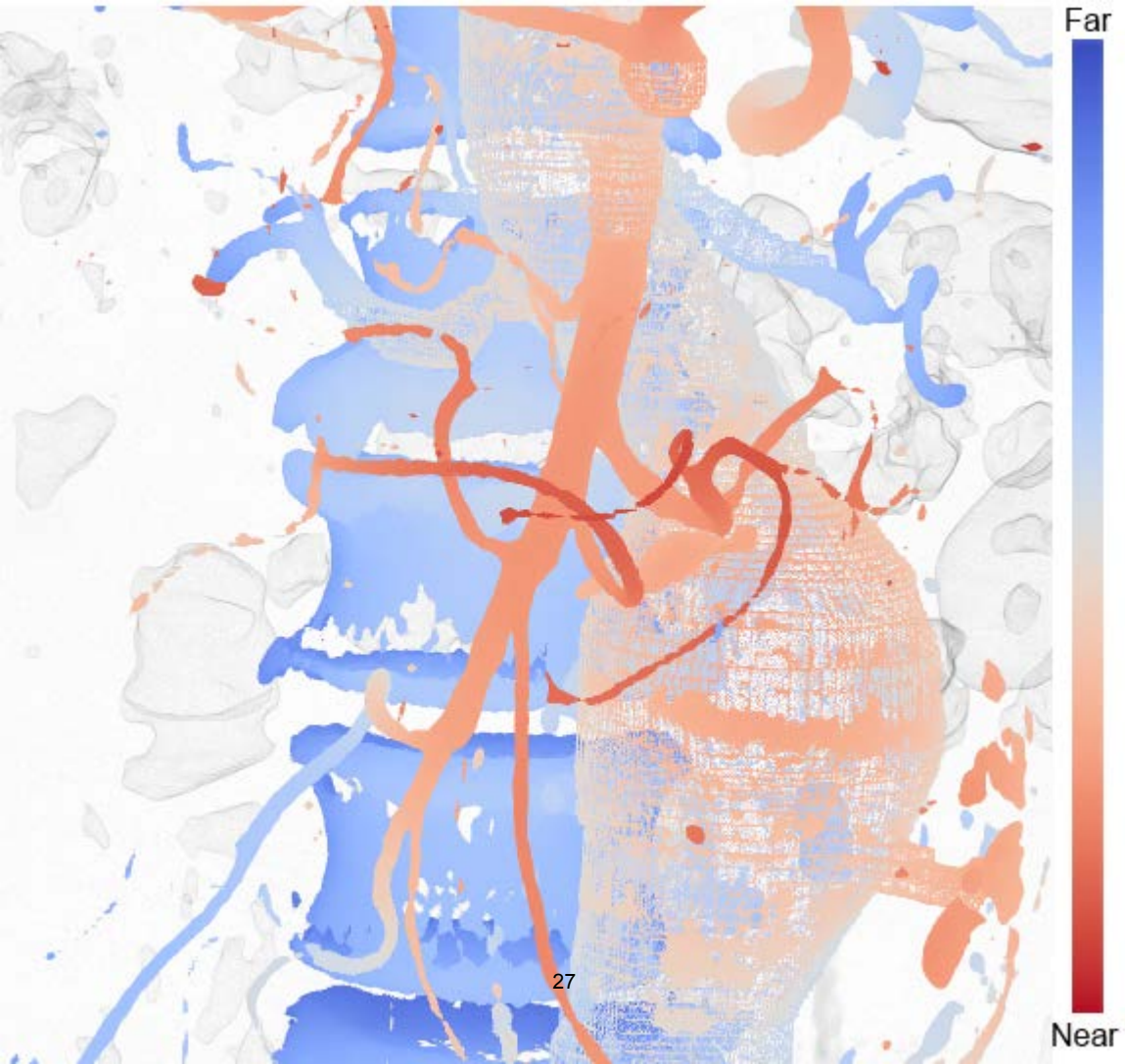
<sup>3</sup> ITK-SNAP - <http://www.itksnap.org/pmwiki/pmwiki.php>

ray casting, only those voxels that are not part of the segmented structures are accumulated. On the other hand for contrasted X-ray images the segmentation is neglected during DRR rendering. Our algorithm extracts the information whether a specific interventional X-ray image is contrasted (angiography) or non-contrasted (fluoroscopy) from dedicated, standardized tags within the image header (DICOM). Depending on the type of image, the algorithm performs the registration to the interventional X-ray with either the masked or the conventional DRR [3]. Once instruments are present within the interventional X-ray scene, the occluded region is outlined automatically [4] and reconstructed with an adapted Poisson editing technique [2]. For subsequent registration to the pre-operative volume, only the reconstructed 2D image is used.

## 4 Conclusion

## References

1. Aichert, A., Wieczorek, M., Wang, J., Wang, L., Kreiser, M., Fallavollita, P., Navab, N.: The colored x-rays. In: Linte, C.A., Chen, E.C., Berger, M.O., Moore, J.T., III, D.R.H. (eds.) *Augmented Environments for Computer-Assisted Interventions*. LNCS, vol. 7815, pp. 45–54. Springer (2012)
2. Demirci, S., Baust, M., Kutter, O., Manstad-Hulaas, F., Eckstein, H.H., Navab, N.: Disocclusion-based 2d-3d registration for angiographic interventions. *Computers in Biology and Medicine* 43(4), 312–322 (May 2013)
3. Demirci, S., Kutter, O., Manstad-Hulaas, F., Bauernschmitt, R., Navab, N.: Advanced 2d-3d registration for endovascular aortic interventions: Addressing dissimilarity in images. In: Miga, M.I., Cleary, K.R. (eds.) *SPIE Medical Imaging: Visualization, Image-guided Procedures, and Modeling*. vol. 6918, pp. 69182S–69190S (2008)
4. Demirci, S., Manstad-Hulaas, F., Navab, N.: Interventional 2d-3d registration in the presence of occlusion. In: *XIII Mediterranean Conference on Medical and Biological Engineering and Computing 2013*. pp. 277–280. Springer (2014)
5. Díaz, J., Vázquez, P.: Depth-enhanced maximum intensity projection. In: *Proc. IEEE/EG Int Conf on Volume Graphics*. pp. 93–100. Eurographics Association (2010)
6. Kersten-Oertel, M., Chen, S.J.S., Collins, D.L.: An evaluation of depth enhancing perceptual cues for vascular volume visualization in neurosurgery. *IEEE Trans Vis Comput Graph* 20(3), 391–403 (2014)
7. Markelj, P., Tomaževič, D., Likar, B., Pernuš, F.: A review of 3d/2d registration methods for image-guided interventions. *Med Image Anal* 16(3), 642–661 (April 2012)
8. Preim, B., Botha, C.: *Visual Computing for Medicine*. Elsevier, 2 edn. (2013)
9. Ropinski, T., Steinicke, F., Hinrichs, K.: Visually supporting depth perception in angiography imaging. In: Butz, A., Fisher, B., Krüger, A., Olivier, P. (eds.) *Smart Graphics*. LNCS, vol. 4073, pp. 93–104. Springer (2006)
10. Wang, X., Schulte zu Berge, C., Demirci, S., Fallavollita, P., Navab, N.: Improved interventional x-ray appearance. In: *Proc. Int. IEEE Symp. on Mixed and Augmented Reality*. In Press (2014)



# Quantitative Comparison of Plaque in Coronary Culprit and Non-culprit Vessel Segments using Intravascular Ultrasound

Zhi Chen<sup>1</sup>, Andreas Wahle<sup>1</sup>, Richard Downe<sup>1</sup>, Shanhui Sun<sup>1</sup>, Katie Porcaro<sup>2</sup>,  
Anoop Agrawal<sup>2</sup>, Taishi Hirai<sup>2</sup>, Vibhav Rangarajan<sup>2</sup>, John Kaminski<sup>2</sup>,  
Stephen Hawn<sup>2</sup>, Tomas Kovarnik<sup>3</sup>, Milan Sonka<sup>1</sup>, and John Lopez<sup>2</sup>

<sup>1</sup> Department of Electrical and Computer Engineering, The University of Iowa, Iowa City IA,  
U.S.A.

<sup>2</sup> Department of Medicine, Cardiology, Loyola University Stritch School of Medicine, Maywood IL,  
U.S.A.

<sup>3</sup> 2nd Department of Internal Medicine, Cardiology and Angiology, 1st Faculty of Medicine,  
Charles University, Prague, Czech Republic.

**Abstract.** Coronary culprit and non-culprit site comparisons have typically been based on manually selected IVUS frames. A novel method for automated selection of culprit and non-culprit frames is reported, based on analyzed distribution of atherosclerotic plaque burden. Comparison of plaque characteristics including presence of thin-cap fibroatheroma (TCFA) in proximal and distal vessel locations was performed relative to the culprit lesion. In 80 patients undergoing coronary catheterization, the study demonstrates that proximal and distal non-culprit frames are substantially different from each other considering both morphology and plaque composition. We have further demonstrated that the range-based comparison increases the analysis robustness.

**Keywords:** Coronary artery, Atherosclerosis, Culprit site, Plaque burden, Intravascular ultrasound, Segmentation, Thin-cap fibroatheroma.

## 1 Introduction

Coronary atherosclerosis is by far the most frequent cause of ischemic heart disease. Rupture of vulnerable plaque or occlusive coronary disease causes the acute coronary syndromes of unstable angina, myocardial infarction, and sudden death [5]. Some autopsy studies suggest that composition and structure of plaque are key determinants of propensity of human atherosclerotic lesions to provoke clinical events [10]. For example, fibroatheromas with a large necrotic core component and thin-cap fibroatheroma (TCFA) that is in extensive contact with the lumen seem particularly prone to rupture, resulting in thrombosis and sudden cardiac death [2, 9, 12].

Modern invasive imaging systems have provided a much more detailed plaque visualization previously only possible through autopsy. Intravascular ultrasound (IVUS) allows tomographic cross-sectional visualization of the full luminal wall

and enables in-vivo assessment of plaque morphology. High ultrasound frequencies are used, typically at 20 to 40 MHz range, providing excellent theoretical resolution. Moreover, spectral analysis of IVUS radiofrequency backscattered signals, known as virtual histology IVUS (VH-IVUS), has been developed to characterize coronary tissues. A more detailed description of the quantitative assessment for different plaque types through VH-IVUS — fibrosis, fibro-fatty, necrotic core, and dense calcium — are provided in [8].

When trying to evaluate the severity of coronary plaque and determine the lesion characteristics, most studies focally examine just a culprit frame instead of the whole vessel. Clinically, a culprit frame is defined as the frame of maximal plaque burden. The potential contributing factors of lesion formation can also be evaluated through the comparison of culprit and non-culprit frames. However, non-culprit frames are usually chosen by experts and the selection varies from person to person; the culprit vs. non-culprit comparison is typically based on analyzing 3 consecutive frames at each of the two locations and may suffer from a lack of generality.

In this paper, we report a new method in which culprit and non-culprit frames are chosen automatically, and in which the subsequent comparison is range-based. To better evaluate non-culprit frames, we also separate them into two groups — distal and proximal, based on their locations along the vessel.

## 2 Method

### 2.1 IVUS Segmentation

IVUS segmentation of lumen and adventitia surfaces in coronary vessels, combined with follow-up VH analysis, is essential to quantitative assessment of atherosclerotic plaque-morphological characteristics. However, most of previous IVUS image segmentation methods with reliable results required substantial user interaction.

Sun et al. recently presented a new graph-based approach for simultaneous dual-surface segmentation of coronary vessels in IVUS images [11]. The approach consists of a fully automated segmentation stage and an efficient user-guided computer-aided refinement stage. During the initial automated segmentation stage, this dual-surface segmentation problem was transformed into a graph optimization problem using the LOGISMOS framework [7]. The two surfaces were simultaneously segmented as the minimum-cost closed set in a weighted graph. During the refinement stage, weights of the previously built graph were updated in response to expert-user’s indication of desired correction and the graph optimization repeated in close-to-real time.

This new segmentation method delivered significantly better results compared to the previous work [4], and the accuracy of automated stage alone was superior to other automated methods that have previously been evaluated using a IVUS challenge database [1]. More importantly, it allowed the user to generate high quality segmentation results with the average operation time reduced from

several hours to several minutes. Our implementation and the interface of this IVUS segmentation method is displayed in **Fig. 1**.

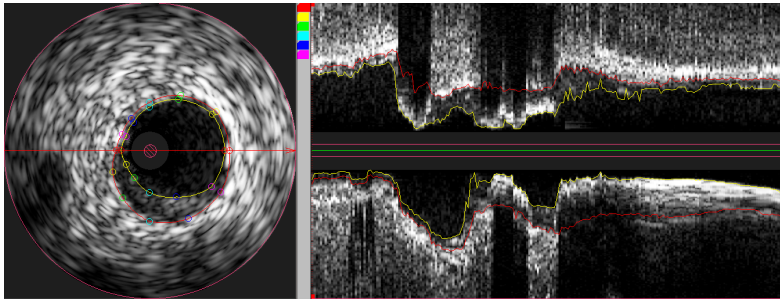


**Fig. 1. Interface of IVUS segmentation.** The left panel is the frame view while the right panel is the longitudinal view along the vessel. User-guided refinement can be done on both views after initial automated segmentation step.

## 2.2 TCFA Definitions

One of the most important features in coronary plaque morphology is thin-cap fibroatheroma (TCFA). The atherosclerotic plaque has a core containing lipids and lipid-rich debris from dead cells. Surrounding it, a layer of smooth muscle cells and a collagen-rich matrix stabilize the plaque. This layer of fibrous connective tissue is called fibrous cap, which is thicker and less cellular than the normal intima [6].

TCFA condition implies that the vessel lesion is at risk of rupture. Based on the actual cap thickness of autopsy specimens, TCFA was defined as a lesion with a fibrous cap  $< 65 \mu\text{m}$  thick and infiltrated by macrophages [2]. A typical IVUS-derived definition of TCFA lesion requires satisfying the following 3 criteria in 3 consecutive frames: 1) confluent necrotic core (NC) in contact with lumen is  $\geq 10\%$  of plaque area; 2) there are  $>30^\circ$  of NCs abutting lumen; 3) plaque burden (PB, plaque area divided by the adventitial cross-sectional area) is  $\geq 40\%$  of the lumen

## 2.3 Morphological Feature Definition

Besides TCFA, various important morphological features are quantified. The frame-based definitions of those features are defined as follows:

- **Adventitia Area:** the area within the outer border of vessel.
- **Lumen Area:** the area within the inner border of vessel.
- **Plaque Area:** the area between inner border and outer border.
- **Plaque Thickness:** each frame is divided into 360 circumferential wedges centered at the centroid of lumen. For each wedge, plaque thickness is defined

as the distance from the adventitia border point to the corresponding lumen border point. For the entire vessel, plaque thickness is defined as the average plaque thickness over all wedges.

- **Plaque Burden:** the ratio of plaque area to adventitia area.
- **Plaque Composition by VH subtype (%)** the percentage of each plaque component (NC/DC/FF/F) over the entire plaque area.
- **Eccentricity:** measured as the ratio of minimal wedge plaque thickness to maximal wedge plaque thickness, which quantifies the asymmetric distribution of atherosclerotic plaque.

## 2.4 Automated Culprit and Non-culprit Selection

As mentioned above, traditional culprit vs. non-culprit studies are subject to limitations: non-culprit frames are usually chosen manually and the culprit vs. non-culprit comparison is based on only 3 consecutive frames at each of the two locations. To improve objectivity and generality, we developed a new method to choose culprit and non-culprit frames automatically, and to explore the difference between them in terms of ranges instead of focal frames:

**Step 1** Location of culprit frame (i.e., maximal plaque burden) is initially determined for each vessel.

**Step 2** All vessels are aligned in longitudinal direction and centered at the culprit frame. For other frames, the distance from culprit is calculated accordingly.

**Step 3** Plaque burden of all frames against the frame distance from culprit are graphed in one single chart for all vessels and a locally weighted scatterplot smoothing (LOESS) regression line is fitted. LOESS is a non-parametric regression method following the logic that points near each other are more likely to be related by using the tri-cube weight function [3]:

$$w(d) = (1 - |d|^3)^3, \text{ where } d \text{ is distance away from point of estimation. (1)}$$

For each data point in graph, a low-degree polynomial is fitted to a subset of the data. Subset size is determined by a smoothing parameter  $\alpha$ , which is in the range  $[\frac{\lambda+1}{n}, 1]$ .  $\lambda$  is the degree of polynomial while  $n$  is the size of dataset. The value of  $\alpha$  is the proportion of data used in each fit and has been set to 0.75 in our case.

**Step 4** Then, a second-derivative test is applied on the LOESS regression line used to determine the critical points, which represent the **local maximal decreasing rate** of plaque burden. The proximal / distal non-culprit zone is defined as the range from such a critical point to end / start of the vessel (**Fig. 2**).

Thereafter, three groups — 3-frame culprit (C), distal (D) and proximal (P) non-culprit are generated and can be compared with each other. Note that the terms of “distal” and “proximal” are defined with respect to the coronary ostium position. Besides C vs. D, C vs. P, C vs. D&P comparison, a new comparison assessing the difference between D and P groups was performed to evaluate non-culprit frames characteristics at different locations along the vessel.

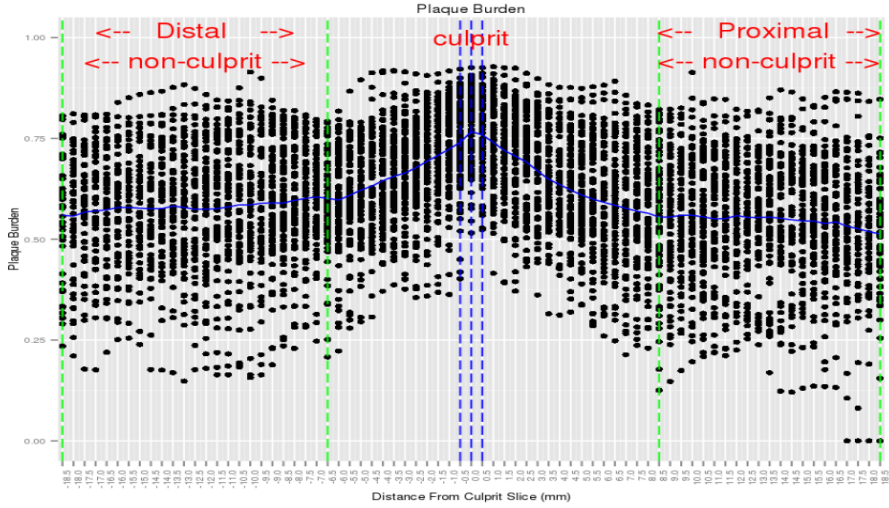


**Fig. 2.** Plaque burden continuous distribution with LOESS regression line (dark blue) for all frames of 80 patients after culprit-centered alignment is shown. Points in each vertical line represent plaque burden values of all IVUS frames positioned at the same distance from the culprit frame. Light blue lines show the 3-frame culprit while green lines show the range of non-culprit. The second derivative cut-off points [distance, plaque burden] are [-6.5mm, 60.1%] and [8.5mm, 55.5%].

### 3 Results & Discussion

The reported analyses were performed in 80 IVUS pullbacks from 80 subjects who underwent coronary catheterization. After aligning the pullbacks at their respective culprit frames, the range of all frames is from -18.5 mm to +18.5 mm (with the culprit frame being centered at 0.0 mm) as shown in Fig. 2. Based on the above-mentioned automated non-culprit frames selection method, the two second derivatives of plaque burden LOESS regression line are -6.5 mm and +8.5 mm respectively. Therefore, the distal non-culprit frames would be represented by frames between -18.5 mm and -6.5 mm; the proximal non-culprit frames would be between +8.5 mm and +18.5 mm.

In summary, there are a total of 258 culprit frames, 1627 distal non-culprit frames and 1474 proximal non-culprit frames. The average distance of distal frames from the culprit location is  $11.9 \pm 3.6$  mm while the average distance of proximal frames is  $13.3 \pm 3.0$  mm.

#### 3.1 TCFA Comparison

The statistical results of TCFA for 3 different groups are shown in Table 1 and the Fisher's exact test results (p-values) are shown in Table 2. Even though culprit frames do contain more TCFA frames (37%) compared to distal frames (33%) and proximal frames (34%), the Fisher's exact test indicates that there are no significant locational differences based on the employed TCFA definition.

**Table 1.** TCFA Analysis of 3 Groups — Culprit (C) / Distal (D)/ Proximal (P)

TCFA =	True	False	Total
Culprit	96 (37%)	162 (63%)	258
Distal	529 (33%)	1098 (67%)	1627
Proximal	503 (34%)	971 (66%)	1474
Distal&Proximal	1032 (33%)	2069 (67%)	3101

**Table 2.** Fisher’s exact Test of 3 Groups TCFA

	C vs. D	C vs. P	D vs. P	C vs. D&P
p-value	0.15	0.36	0.36	0.21

### 3.2 Morphological Comparison

The statistical results of morphology for 3 different groups are shown in Table 3 and the respective unpaired Student’s *t*-test results (p-values) are shown in Table 4. As expected, culprit frames contain significantly larger plaque burden (0.76) compared to non-culprit frames — distal (0.58), proximal (0.55) and distal&proximal (0.57). Moreover, culprit frames exhibit significantly larger plaque thickness and plaque CSA, which is leading to a smaller lumen CSA. Something more interesting concerns adventitial CSA and eccentricity features comparison:

- **Adventitia CSA:** The *t*-test’s p-value shows that culprit and non-culprit (proximal&distal) frames have no significant difference over adventitia CSA (15.81 vs. 15.92  $mm^2$ ). However, culprit frames have actually a larger adventitia CSA than distal non-culprit frames but a smaller adventitia CSA than proximal frames.
- **Eccentricity:** The culprit frames are prone to have a smaller eccentricity compared to non-culprit frames. In other words, plaque accumulation in culprit frames are distributed more evenly than in non-culprit frames.

We summarize below the comparison over plaque components — necrotic core (NC), dense calcium (DC), fibrofatty (FF) and fibrotic plaque (F):

- **NC:** the significant difference was observed for on culprit vs. distal frames (p-value = 0.033) and culprit vs. distal&proximal (p=0.044). However, NC percentage is not significantly different between culprit and proximal. Thus, it can be concluded that the NC% significant difference between culprit and distal&proximal is derived from differences between culprit and distal locations alone; NC% of the culprit frames is higher than that of distal frames but similar to proximal frames.
- **DC:** culprit frames have a lower DC% than non-culprit frames.
- **FF:** FF% of culprit frames is higher than that of distal frames but similar to proximal frames.
- **F:** culprit frames have a higher F% than non-culprit frames.

**Table 3.** Morphological Analysis of 3 Groups — Culprit (C) / Distal (D) / Proximal (P)

Mean $\pm$ Std	Culprit (C)	Distal (D)	Proximal (P)	Distal&Proximal
Plaque Burden	0.76 $\pm$ 0.10	0.58 $\pm$ 0.14	0.55 $\pm$ 0.15	0.57 $\pm$ 0.15
Plaque Thickness ( <i>mm</i> )	1.13 $\pm$ 0.35	0.77 $\pm$ 0.34	0.81 $\pm$ 0.33	0.79 $\pm$ 0.34
Plaque CSA ( <i>mm</i> <sup>2</sup> )	12.14 $\pm$ 5.00	8.56 $\pm$ 4.82	9.96 $\pm$ 4.85	9.22 $\pm$ 4.89
Lumen CSA ( <i>mm</i> <sup>2</sup> )	3.67 $\pm$ 1.86	5.44 $\pm$ 2.54	8.08 $\pm$ 4.39	6.69 $\pm$ 3.78
Adventita CSA ( <i>mm</i> <sup>2</sup> )	15.81 $\pm$ 5.55	14.00 $\pm$ 6.13	18.03 $\pm$ 6.58	15.92 $\pm$ 6.65
Eccentricity	0.64 $\pm$ 0.19	0.67 $\pm$ 0.18	0.69 $\pm$ 0.17	0.68 $\pm$ 0.17
Necrotic Core (%)	22.35 $\pm$ 11.48	20.68 $\pm$ 12.38	21.01 $\pm$ 12.14	20.84 $\pm$ 12.26
Dense Calcium (%)	7.70 $\pm$ 8.36	10.70 $\pm$ 11.85	10.39 $\pm$ 10.46	10.55 $\pm$ 11.21
Fibrofatty (%)	12.35 $\pm$ 9.95	10.03 $\pm$ 11.48	11.04 $\pm$ 11.18	10.51 $\pm$ 11.35
Fibrotic Plaque (%)	57.60 $\pm$ 13.43	52.87 $\pm$ 21.28	55.52 $\pm$ 17.80	54.13 $\pm$ 19.75

**Table 4.** Statistical Comparison among 3 Groups Using t-test

p-value	C vs. D	C vs. P	D vs. P	C vs. D&P
Plaque Burden	$\ll$ 0.01	$\ll$ 0.01	$\ll$ 0.01	$\ll$ 0.01
Plaque Thickness ( <i>mm</i> )	$\ll$ 0.01	$\ll$ 0.01	0.004	$\ll$ 0.01
Plaque CSA ( <i>mm</i> <sup>2</sup> )	$\ll$ 0.01	$\ll$ 0.01	$\ll$ 0.01	$\ll$ 0.01
Lumen CSA ( <i>mm</i> <sup>2</sup> )	$\ll$ 0.01	$\ll$ 0.01	$\ll$ 0.01	$\ll$ 0.01
Adventita CSA ( <i>mm</i> <sup>2</sup> )	$\ll$ 0.01	$\ll$ 0.01	$\ll$ 0.01	0.776
Eccentricity	0.013	$\ll$ 0.01	0.003	0.001
Necrotic Core (%)	0.033	0.086	0.462	0.044
Dense Calcium (%)	$\ll$ 0.01	$\ll$ 0.01	0.442	$\ll$ 0.01
Fibrofatty (%)	0.001	0.056	0.013	0.005
Fibrotic Plaque (%)	$\ll$ 0.01	0.031	$\ll$ 0.01	$\ll$ 0.01

### 3.3 Non-culprit: Proximal vs. Distal

Above comparisons between culprit and non-culprit frames have already exhibited some differences between proximal and distal non-culprit frames over features like adventitia area, NC% and DC%. A closer look at Table 3 and Table 4 shows that morphological structures of distal and proximal non-culprit frames are substantially different from each other. Compared to proximal frames, distal ones have smaller lumen CSA and smaller adventitial CSA, which could be caused by the natural shape of the vessels. The larger plaque burden value of distal frames may indicate a faster relative plaque-accumulation rate than proximal frames. As for plaque components, FF% and F% are different between distal and proximal non-culprit frames as well, with both values being lower in distal frames.

## 4 Conclusion

Previous studies of culprit and non-culprit comparisons were mainly based on manually chosen frames, which could belong to either proximal or distal segments or the combination of both. In contrast, our approach selects the culprit and non-culprit frames automatically. Our results have shown that proximal and distal non-culprit frames are substantially different from each other considering both morphology and plaque composition. We have further demonstrated that the range-based comparison increases the analysis robustness. Even though we revealed many morphological differences, the TCFA definition we implemented

failed to separate culprit and non-culprit frames. One possible reason could be that the axial resolution of IVUS (100-150  $\mu\text{m}$ ) is not good enough to detect TCFA (cap thickness  $< 65 \mu\text{m}$ ) directly and IVUS-derived TCFA definition is based on environmental characteristics rather than features of cap itself. A further exploration on variations of IVUS-derived TCFA definitions is required.

## References

1. Balocco, S., Gatta, C., Ciompi, F., Wahle, A., Radeva, P., Carlier, S., Unal, G., Sanidas, E., Mauri, J., Carillo, X., et al.: Standardized evaluation methodology and reference database for evaluating ivus image segmentation. *Computerized Medical Imaging and Graphics* 38(2), 70–90 (2014)
2. Burke, A.P., Farb, A., Malcom, G.T., Liang, Y.h., Smialek, J., Virmani, R.: Coronary risk factors and plaque morphology in men with coronary disease who died suddenly. *New England Journal of Medicine* 336(18), 1276–1282 (1997)
3. Cleveland, W.S., Devlin, S.J.: Locally weighted regression: an approach to regression analysis by local fitting. *Journal of the American Statistical Association* 83(403), 596–610 (1988)
4. Downe, R., Wahle, A., Kovarnik, T., Skalicka, H., Lopez, J., Horak, J., Sonka, M.: Segmentation of intravascular ultrasound images using graph search and a novel cost function. In: *Proceedings of 2nd MICCAI Workshop on Computer Vision for Intravascular and Intracardiac Imaging*, New York, NY. pp. 71–79 (2008)
5. Epstein, F.H., Fuster, V., Badimon, L., Badimon, J.J., Chesebro, J.H.: The pathogenesis of coronary artery disease and the acute coronary syndromes. *New England Journal of Medicine* 326(4), 242–250 (1992)
6. Hansson, G.K., Libby, P.: The immune response in atherosclerosis: a double-edged sword. *Nature Reviews Immunology* 6(7), 508–519 (2006)
7. Li, K., Wu, X., Chen, D.Z., Sonka, M.: Optimal surface segmentation in volumetric images—a graph-theoretic approach. *Pattern Analysis and Machine Intelligence, IEEE Transactions on* 28(1), 119–134 (2006)
8. Nair, A., Kuban, B.D., Tuzcu, E.M., Schoenhagen, P., Nissen, S.E., Vince, D.G.: Coronary plaque classification with intravascular ultrasound radiofrequency data analysis. *Circulation* 106(17), 2200–2206 (2002)
9. Sangiorgi, G.M., Clementi, F., Cola, C., Biondi-Zoccai, G.: Plaque vulnerability and related coronary event prediction by intravascular ultrasound with virtual histology: it’s a long way to tipperary? *Catheterization and Cardiovascular Interventions* 70(2), 203–210 (2007)
10. Stary, H.C.: Natural history and histological classification of atherosclerotic lesions an update. *Arteriosclerosis, thrombosis, and vascular biology* 20(5), 1177–1178 (2000)
11. Sun, S., Sonka, M., Beichel, R.: Graph-based IVUS segmentation with efficient computer-aided refinement (2013)
12. Virmani, R., Burke, A.P., Farb, A., Kolodgie, F.D.: Pathology of the vulnerable plaque. *Journal of the American College of Cardiology* 47(8s1), C13–C18 (2006)

# Fully automated detection of healthy wall sections in intracoronary optical coherence tomography

Guillaume Zahnd<sup>1</sup>, Antonios Karanasos<sup>2</sup>, Gijs van Soest<sup>3</sup>, Evelyn Regar<sup>2</sup>,  
Wiro Niessen<sup>1</sup>, Frank Gijssen<sup>3</sup>, and Theo van Walsum<sup>1</sup>

<sup>1</sup> Biomedical Imaging Group Rotterdam, Departments of Radiology and Medical Informatics, Erasmus MC, P.O. Box 2040, 3000 CA Rotterdam, The Netherlands

[g.zahnd@erasmusmc.nl](mailto:g.zahnd@erasmusmc.nl)

<sup>2</sup> Department of Interventional Cardiology, Thorax Center, Erasmus MC, Rotterdam, The Netherlands

<sup>3</sup> Department of Biomedical Engineering, Erasmus MC, Rotterdam, The Netherlands

**Abstract.** Automated processing of intracoronary optical coherence tomography (OCT) images represents an important issue. The aim of the present study is to introduce a fully automated method to differentiate healthy tissues from diseased regions of the coronary wall in *in vivo* OCT imaging. A two-step framework is proposed. First, an original contour segmentation scheme is performed to simultaneously extract the interfaces of the intima and media layers. Second, a set of local features is extracted at the estimated location of the interfaces, and a classification method is applied. Evaluated on a dataset of 50 images acquired from 10 different patients, the present detection framework demonstrated a sensitivity and specificity of 80 % and 81 %, respectively, while the agreement between manual annotations performed by two analysts was 86 %.

**Keywords:** Optical coherence tomography, Contour segmentation, Classification, Coronary artery

## 1 Introduction

Intravascular optical coherence tomography (OCT) is an emerging catheter-based imaging modality that enables tissues to be visualized *in vivo* at a high spatial resolution (10–20  $\mu\text{m}$ ) and in a minimally invasive fashion. Investigation of the inner circumference of the vessel is performed by the probe spinning along its axis while being pulled back. The emission and reception of near-infrared light at each angular step yields the acquisition of so called A-lines, whose echo time and intensity are then converted into a single gray-scale image. During the pullback acquisition, a stack of consecutive cross-sectional images is generated along the length of the assessed artery segment.

Although OCT images are acquired online and can provide the clinician useful visual insight during the intervention, image analysis is currently performed

manually offline (Tearney et al, 2012). Such manual procedure is generally time consuming as well as subject to variability between different analysts (Kubo et al, 2007). Accordingly, automated processing of OCT images remains an important issue, as it would allow clinicians to use quantified information directly during the intervention.

Various (semi)automated computerized methods have recently been introduced to tackle this challenge, and have addressed several clinical applications. Stent strut apposition, coverage and re-endothelialization was assessed by means of strut shadow detection (Gurmeric et al, 2009), active contours (Kauffmann et al, 2010) and peak intensity location (Ughi et al, 2012). Fibrous cap thickness was quantified with contour segmentation approaches based on front-propagation (Wang et al, 2012; Zahnd et al, 2014). Tissue type classification was investigated by exploiting the backscattering coefficient (Xu et al, 2008), the attenuation coefficient (van Soest et al, 2010), and image texture (Ughi et al, 2013).

The aim of this study is to propose a fully automated method to detect healthy tissues from diseased sections of the wall in *in vivo* OCT images. The main contribution of the present work is the introduction of a novel segmentation method, based on a four-dimensional (4D) front propagation scheme, and devised to simultaneously extract the contours of the intima and media layers. A number of texture- and geometry-based local features are then generated at the location of the extracted contours, then a traditional classification approach is performed to differentiate healthy and diseased tissues. The proposed framework is finally evaluated in a set of 50 OCT images from 10 patients against the reference annotations performed by two analysts.

## 2 Methods

The present framework consists of two main steps. First, a segmentation step is carried out to extract both intima and media layers. Second, a classification step is performed, using several features locally provided by the segmented contours. Our rationale is the following: forcing the segmentation in diseased regions where intima and media layers can not be perceived is likely to result in contours with an irregular shape located on poorly contrasted regions, yielding features that are significantly different from those extracted from healthy and contrasted regions.

### 2.1 Multi-layer segmentation

Healthy regions are defined as regions without plaque, where intima, media and adventitia layers can be clearly perceived. From a single A-line perspective, the interfaces of the intima, media and adventitia layers correspond to regions with strong positive and negative intensity gradient, as depicted in Figure 1. The lumen-intima interface (uppermost positive gradient,  $G_0$ ) can easily be extracted by a classical gradient search. However, the intima-media and media-adventitia interfaces are significantly more challenging to assess due to a number of factors,

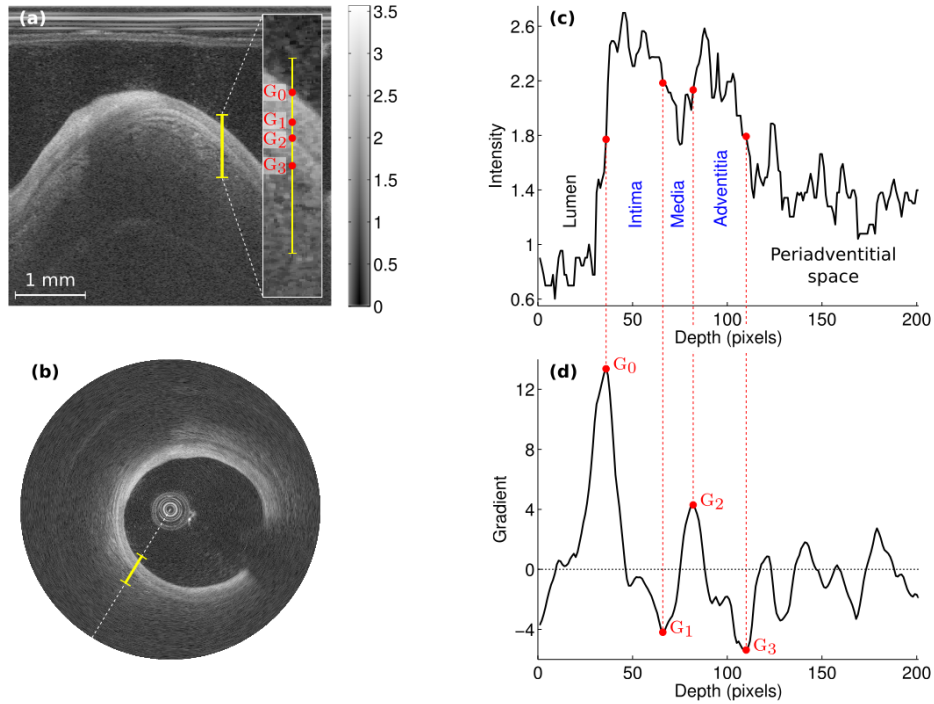


**Fig. 1.** OCT imaging of a human coronary artery *in vivo*. (a) Polar image. (b) Corresponding Cartesian image. The yellow line in (a) corresponds to the yellow line in (b). (c) Intensity profile of healthy wall tissues, corresponding to the A-line section delimited by the yellow line in (a). (d) Corresponding gradient, with the extrema  $G_0$ ,  $G_1$ ,  $G_2$  and  $G_3$  delimiting the intima, media and adventitia layers (red points).

such as a weaker gradient magnitude, a lower signal-to-noise ratio, the absence of the layers in diseased regions, and a potential variation of intima thickness.

To cope with this challenge, the present segmentation method is devised to simultaneously extract the location of the uppermost negative ( $G_1$ ), lowermost positive ( $G_2$ ), and lowermost negative ( $G_3$ ) gradients. The proposed method is designed to process 2D images in polar coordinates (Fig. 2a). The fast marching methodology (Cohen, 2005) was adopted to introduce a specific unidirectional 4D front-propagation scheme. Here, the 4D space corresponds to the direction of the propagation along the circumference, plus the depth location of the three contours (Fig. 2). This approach is ruled by three characteristics. First, the paths should be located on gradient extrema. For this purpose, an image data term  $C$  is used, corresponding to the vertical gradient image normalized between 0 and 1. Second, the paths should be (nearly) parallel to the lumen-intima interface. A spatial transformation is thus applied to generate a sub-image where the lumen-intima interface is a straight horizontal line (Zahnd et al, 2013, 2014) and a

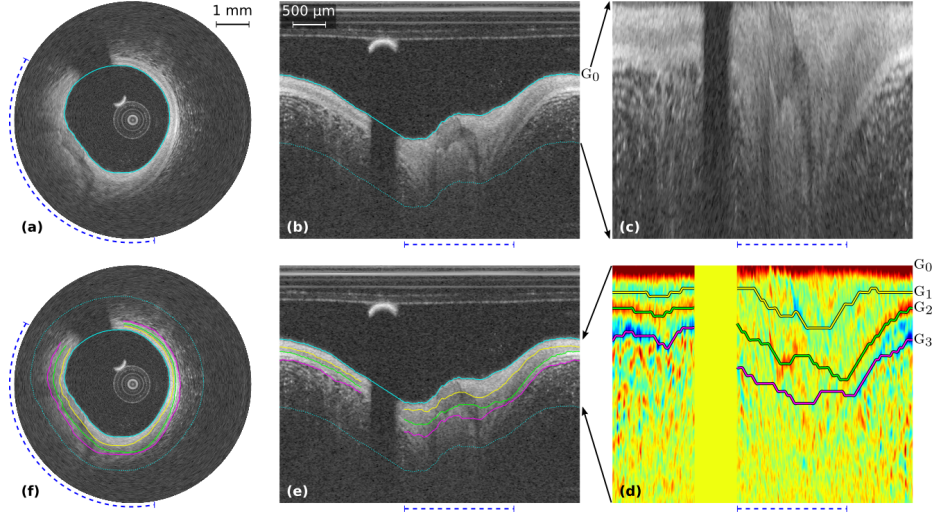


**Fig. 2.** Multi-layer segmentation framework. (a) Cartesian image, with the lumen segmentation (cyan solid line,  $G_0$ ). The outer circumference of the diseased section of the wall is indicated by the blue dashed line. The intima, media and adventitia layers are clearly visible in the healthy section. (b) Corresponding polar image. The cyan dashed line indicates the depth of the investigated region. (c) Transformed sub-image, where the lumen interface  $G_0$  is a straight horizontal line. (d) Cost image  $C$  of vertical gradients, with the three estimated paths  $G_1$ ,  $G_2$  and  $G_3$  running along the extrema. (e) Resulting polar image. (f) Corresponding Cartesian image.

penalty is then applied to non-horizontal displacements. Third, the paths should describe concentric layers. Therefore, a non-crossing constraint is applied.

To simultaneously extract the optimal location for all three contours  $G_1$ ,  $G_2$  and  $G_3$ , a single 4D cumulated cost function  $\mathcal{C}$  is then iteratively generated as:

$$\begin{aligned} \mathcal{C}(y_1, y_2, y_3, x) = \min_{dy_1, dy_2, dy_3} & \left\{ \mathcal{C}(y_1 + dy_1, y_2 + dy_2, y_3 + dy_3, x - 1) \right. \\ & + \sqrt{1 + \kappa_a \cdot dy_1^{\kappa_b}} \cdot \omega \cdot \mathcal{C}(y_1, x) + \sqrt{1 + \kappa_a \cdot dy_2^{\kappa_b}} \cdot (1 - \mathcal{C}(y_2, x)) \\ & \left. + \sqrt{1 + \kappa_a \cdot dy_3^{\kappa_b}} \cdot \mathcal{C}(y_3, x) \right\}, \end{aligned} \quad (1)$$

with  $y_{i+1} > y_i + m$ ,  $y_i$  being the depth of the  $i^{\text{th}}$  path  $G_i$  in a given A-line  $x$  and  $m$  being the vertical margin between two paths;  $dy_i \in \{-n, \dots, 0, \dots, n\}$ ,  $n$  being the number of reachable neighbors;  $\kappa_a$  and  $\kappa_b$  the smoothness constraint terms; and  $\omega \in [0, 1]$  a weighting factor preventing the uppermost path from running along the location of the lowermost media-adventitia interface.  $\mathcal{C}$  is initialized to zero, and a null cost is attributed to the A-lines corresponding to the region shadowed by the guidewire. This front-propagation scheme is run twice, namely from left

to right and from right to left. A seed is then determined as the point where the two fronts first collide. Finally, the optimal solution is found by back-tracking in  $\mathcal{C}$  from the seed to each border of the image. A graphical representation of the segmentation framework is displayed in Figure 2.

## 2.2 Classification

After the segmentation step has been carried out, a classification step is performed. The adaptive boosting (AdaBoost) predictive algorithm (Freund and Schapire, 1997; Freund et al, 1999) is used for classification. Briefly, the underlying principle of AdaBoost consists in iteratively adapting the weights of simple weak classifiers in the aim to finally generate a strong classifier that is well correlated with the ground truth annotations (*i.e.* the binary “*healthy*” or “*diseased*” label manually attributed to each A-line of the image). In the present implementation, 8 features characterizing a typical healthy wall profile (Fig. 1c) are extracted from each A-line:

- The intensity gradient magnitude  $\{g_1, g_2, g_3\}$  at the location of each of the three extracted paths  $G_1, G_2$  and  $G_3$ ;
- The depth-wise distance  $\{d_{1,2}, d_{1,3}, d_{2,3}\}$  between each of the three extracted paths, compensated with the penetration angle of the beam in the tissues;
- The mean absolute gradient magnitude  $\{G\}$  within the A-line;
- The index of monotonic decrease  $\{M\}$ , calculated as the mean absolute distance of all piece-wise permutations required to sort the intensity values of the A-line in a monotonically decreasing fashion.

The image intensity is normalized between 0 and 1 prior to feature extraction. To improve the robustness of the method when investigating the  $k^{\text{th}}$  frame of the pullback, the classification is also carried out in the  $k - 1^{\text{st}}$  and  $k + 1^{\text{st}}$  frames, and the the resulting label of each A-line is determined by means of majority voting. Finally, a morphological opening and closing operation is performed to aggregate similar labels and get rid of outliers.

## 2.3 Data collection

OCT pullbacks were acquired at the Thoraxenter, Erasmus MC (Rotterdam, The Netherlands), using the C7XR frequency-domain system and the Dragonfly intracoronary imaging catheter (Lightlab/St Jude, Minneapolis, MN, USA). Image acquisition was performed with a previously described non-occlusive technique (Tearney et al, 2012). Pullbacks were acquired over a total length of 54 mm along the vessel at 105 frames/s. The central bandwidth of the near-infrared light was 1310 nm. The spatial resolution of the system was 20  $\mu\text{m}$  and 30  $\mu\text{m}$  in the axial and lateral directions, respectively. The depth of the scan range was 4.3 mm. Acquired images were sampled at  $968 \times 504$  pixels.

## 2.4 Image analysis procedure

For each pullback, a set of representative frames was selected by the analyst  $\mathcal{A}_1$ . A ground truth reference was then manually generated by  $\mathcal{A}_1$ , by applying a

binary label (*i.e.* healthy or diseased) to each A-line of all analyzed frames. To further train the classifier, manual annotations were also performed on the two temporally adjacent (*i.e.* previous and next) frames in the pullback. Inter-observer variability was also assessed by a second analyst  $\mathcal{A}_2$  carrying out the same annotation procedure, blinded to the results of  $\mathcal{A}_1$ . A leave-one-out validation was realized to evaluate the automated classification framework against the generated ground truth reference labels.

## 2.5 Parameter settings

The present framework was applied to all images with the following parameter settings, determined by means of a leave-one-out strategy. Smoothness constraint terms,  $\kappa_a = 0.3$  and  $\kappa_b = 0.5$ , weighting factor,  $\omega = 0.1$ , minimal margin between two paths,  $m = 75 \mu\text{m}$ , number of reachable neighbors,  $n = 10$ , length of the gradient filter:  $95 \mu\text{m}$ , kernel size of the morphological opening and closing: 7 and 60 A-lines, respectively, number of iterations for AdaBoost: 100.

## 3 Results and discussion

Ten patients suffering from coronary artery disease were involved in the study. For each pullback, 5 representative and non-consecutive frames were arbitrarily selected by  $\mathcal{A}_1$  to be analyzed. Among the 50 analyzed images, the proportion of healthy sections, as annotated by  $\mathcal{A}_1$ , was 51 % (*i.e.* 11247 A-lines over 22000). The layer segmentation method was applied to all analyzed images. In healthy sections of the wall, the resulting contours corresponded well with the anatomical interfaces for the majority of the frames (*i.e.* 45 out of 50), as visually assessed. In the remaining 5 cases, failure was provoked by the presence of bright and contrasted tissues behind a thin intima-media complex, shifting all three segmentation contours towards a deeper location. Evaluated against the tracings performed by  $\mathcal{A}_1$ , the sensitivity and specificity of the detection framework was 80 % and 81 %, respectively. This is to be compared with the agreement of both analysts when performing the manual annotation, which was 86 %. Examples of detection results are displayed in Figure 3. In misclassified regions, the main cause of failure of the framework is due to occasional overlapping between healthy and diseased feature values. We also observed that the performances of the method were associated with the degree of agreement between the two analysts  $\mathcal{A}_1$  and  $\mathcal{A}_2$ . In regions that were assigned the same label by  $\mathcal{A}_1$  and  $\mathcal{A}_2$ , the sensitivity and specificity of the detection framework was 82 % and 86 %, respectively, whereas in regions that were assigned two different labels, the performances decreased to 51 % and 65 %, respectively. By forcing the segmentation in diseased regions where the anatomical layers can not be perceived, the method is expected to yield features that can easily be differentiated from those extracted from healthy regions. Further studies will focus on the application of the present segmentation method to segmenting the contours of different tissue types, such as calcified plaques and thin cap fibroatheromas.

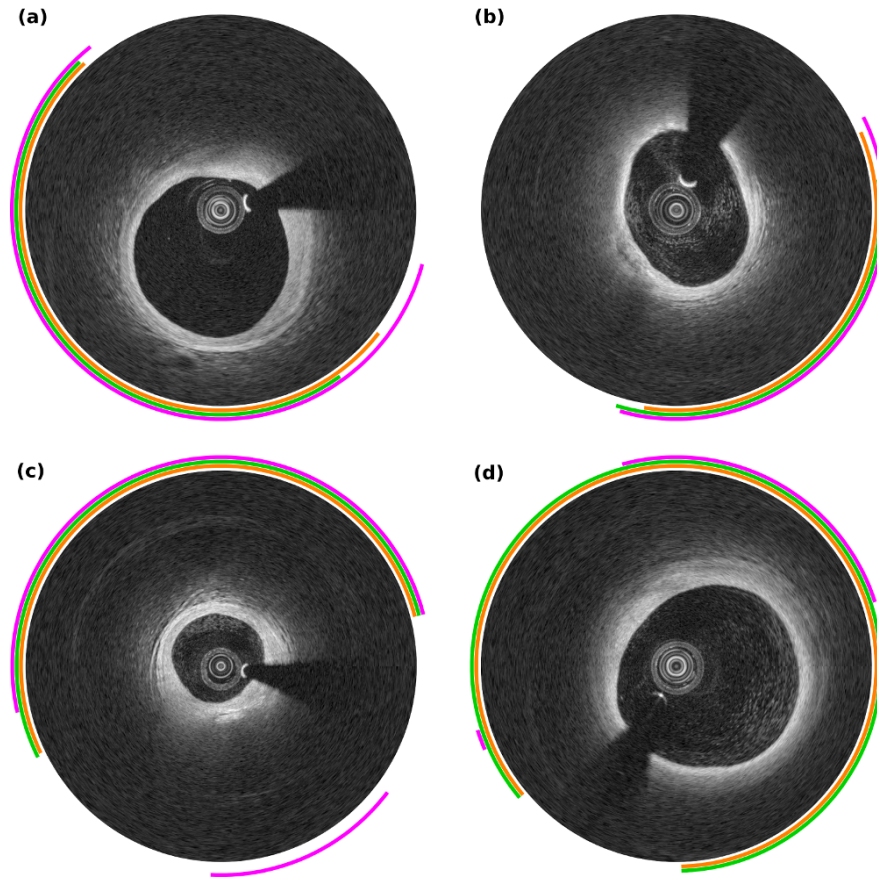


**Fig. 3.** Representative examples of healthy wall detection, for the automatic classification method (magenta), compared to the manual annotations performed by the two analysts (green and orange), in OCT pullbacks acquired in four different patients, for successful detection of the healthy section (a,b) and failures (c,d). The specificity in (c) is poor, as the diseased region in 4-6 o'clock presents a contrasted and heterogeneous pattern that is detected as healthy layers. The sensitivity in (d) is poor, as most of the healthy region (3-11 o'clock) presents diffuse layers with weak gradient magnitudes.

## 4 Conclusion

A fully automated method to detect healthy sections of the wall in OCT images was presented. The introduced framework relies on an original multi-layer segmentation approach, devised to locally extract texture- and geometry-based features that describe the intima and media interfaces. With performances close to inter-analyst variability, the proposed framework represents a promising approach to assist clinicians with quantified information during intervention.

## Bibliography

- Cohen L. Minimal paths and fast marching methods for image analysis. *Mathematical Models in Computer Vision: The Handbook*. 2005:97–111.
- Freund Y, Schapire RE. A decision-theoretic generalization of on-line learning and an application to boosting. *Journal of Computer and System Sciences*. 1997;55(1):119–139.
- Freund Y, Schapire RE, Abe N. A short introduction to boosting. *Journal of Japanese Society for Artificial Intelligence*. 1999;14(5):771–780.
- Gurmeric S, Isguder GG, Carlier SG, Unal G. A new 3-D automated computational method to evaluate in-stent neointimal hyperplasia in in-vivo intravascular optical coherence tomography pullbacks. *MICCAI*. 2009:776–785.
- Kauffmann C, Motreff P, Sarry L. In vivo supervised analysis of stent reendothelialization from optical coherence tomography. *IEEE Transactions on Medical Imaging*. 2010;29(3):807–818.
- Kubo T, Imanishi T, Takarada S, et al. Assessment of culprit lesion morphology in acute myocardial infarction: Ability of optical coherence tomography compared with intravascular ultrasound and coronary angiography. *J Am Coll Card*. 2007;50(10):933–939.
- Tearney GJ, Regar E, Akasaka T, et al. Consensus standards for acquisition, measurement, and reporting of intravascular optical coherence tomography studies. *J Am Coll Card*. 2012;59(12):1058–1072.
- Ughi GJ, Adriaenssens T, Onsea K, et al. Automatic segmentation of in-vivo intra-coronary optical coherence tomography images to assess stent strut apposition and coverage. *Int J Cardiovasc Imaging*. 2012;28(2):229–241.
- Ughi GJ, Steigerwald K, Adriaenssens T, et al. Automatic characterization of neointimal tissue by intravascular optical coherence tomography. *J Biomed Opt*. 2013;19:021104.
- van Soest G, Goderie T, Regar E, et al. Atherosclerotic tissue characterization *in vivo* by optical coherence tomography attenuation imaging. *J Biomed Opt*. 2010;15:011105–1–9.
- Wang Z, Chamie D, Bezerra HG, et al. Volumetric quantification of fibrous caps using intravascular optical coherence tomography. *Biomed Opt Express*. 2012;3:1413–1426.
- Xu C, Schmitt JM, Carlier SG, Virmani R. Characterization of atherosclerosis plaques by measuring both backscattering and attenuation coefficients in optical coherence tomography. *J Biomed Opt*. 2008;13:034003.
- Zahnd G, Karanasos A, van Soest G, Regar E, Niessen WJ, Gijzen FJH, van Walsum T. Semi-automated quantification of fibrous cap thickness in intracoronary optical coherence tomography. *IPCAI*. 2014:78–89.
- Zahnd G, Orkisz M, Sérusclat A, Moulin P, Vray D. Simultaneous extraction of carotid artery intima-media interfaces in ultrasound images: assessment of wall thickness temporal variation during the cardiac cycle. *IJCARS*. 2013;9(4):645–658.

# Side-Branch Guided Registration of Intravascular Ultrasound Pullbacks in Coronary Arteries

Ling Zhang<sup>1</sup>, Richard Downe<sup>1</sup>, Zhi Chen<sup>1</sup>, Shanhui Sun<sup>1</sup>, Tatiana Masiarova<sup>1</sup>,  
Tomas Kovarnik<sup>2</sup>, John Lopez<sup>3</sup>, Milan Sonka<sup>1</sup>, and Andreas Wahle<sup>1</sup>

<sup>1</sup> Department of Electrical and Computer Engineering, University of Iowa, Iowa City, IA, USA

<sup>2</sup> 2<sup>nd</sup> Department of Internal Medicine, Cardiology and Angiology, 1<sup>st</sup> Faculty of Medicine,  
Charles University, Prague, Czech Republic

<sup>3</sup> Department of Medicine, Cardiology, Loyola University Stritch School of Medicine,  
Maywood IL, USA

**Abstract.** Studies on the natural course of plaque progression require serial comparisons of local measurement between baseline and follow-up Intravascular Ultrasound (IVUS) pullback imaging data. In this paper, we consider the problem of automatically estimating the spatiotemporal registration between IVUS pullback pairs. Unlike the existing methods, which rely on coronary vascular morphology and plaque composition, we present a novel approach that is guided by side-branches. Since side-branches are the only landmarks that provide consistent correspondence in two time points, we use them as anchors to control the follow-up pullback: to scale the coordinates along the longitudinal direction by using a piecewise transform, and to generate rotational shift within the cross-sectional image by applying a Catmull-Rom spline. Experimental results on 31 *in-vivo* IVUS pullback pairs show that our method is efficient, and can significantly reduce discrepancies between pullback pairs.

## 1 Introduction

Prediction of the coronary vasculature at high risk of atherosclerotic disease progression has the potential of affecting treatment options or allowing novel pre-emptive approaches to treat patients with subclinical atherosclerosis. Studies of the relationships between local coronary morphology, plaque composition, blood flow dynamics, and atherosclerotic plaque progression at several-month intervals can offer insights in the natural course of plaque development, consequently enabling predictions about atherosclerotic disease progression from initial imaging of coronary vessel [1-3]. Intravascular ultrasound (IVUS) is a valuable and clinically available imaging tool to examine the progression of coronary artery disease [1-3]. For the purposes of serial measurement comparisons, the baseline and follow-up IVUS data must be registered.

Due to the difficulties of IVUS registration task (such as motion artifacts, changes in blood pressure, vessel morphology, plaque composition etc.), most previous studies registered IVUS pullbacks manually, which is a tedious and time consuming process. Automated registration has attracted research interests in recent years. Alberti et al. [4] first presented an automated framework for the temporal alignment of IVUS pull-

backs. They developed a dynamic time warping technique which utilized multiple temporal profiles representing vessel area and plaque composition. Different from their work, Timmins et al. [5] focus on the co-registration of two aligned cross-sectional IVUS frames. Their method is mainly based on image parameters including arterial thickness, Virtual Histology (VH)-IVUS defined plaque constituents [6], and VH-IVUS perivascular imaging data. Both of these methods try to use vessel area and plaque composition to register IVUS pullbacks. However, using these features is not recommended in general, especially when the degree of disease progression, which may cause pronounced changes to the plaque appearance from baseline to follow-up. To alleviate these problems, Vukicevic et al. [7] propose to use vessel shape as the matching criterion. The basis for measuring all the before-mentioned features relies on the segmentation of lumen and adventitia of IVUS images, which is a user-dependent and error-prone task. Furthermore, the accuracy of the VH correlation of plaque constituent characterization has recently been called into question [2, 3].

Unlike previous methods, our method does not rely on the segmentation of luminal and external elastic lamina borders or the identification of plaque components. We propose a simple but effective approach to automatically align and register the baseline and follow-up IVUS pullbacks. Considering that the side-branches provide the most information and are also the only landmarks that provide consistent correspondence in two time points, we use them as anchors to control the follow-up pullback to scale the coordinates along the longitudinal direction and to generate rotational shift within the cross-sectional image. We evaluated our method on baseline and follow-up IVUS pullbacks for one vessel of 31 patients each.

## 2 Methods

### 2.1 Semi-Automated Identification of Side-branches

After gating the IVUS pullbacks by R-wave of electrocardiogram (ECG) signal, side-branches are identified using a semi-automated approach [8] with the center of bifurcation, distal point on the branching vessel, and one or more intermediate control points interactively identified. A 3-D trajectory of the side-branch is generated by computing a uniform cubic B-spline over the range of user-identified control points. The control points are adjusted based on the segmentation, and the spline is recomputed. Finally, a 3-D side-branch is constructed around the spline as a generalized cylinder, using the radius computed from the 2-D segmentation.

### 2.2 Registration of Baseline and Follow-up Arterial Segments

Because the IVUS space is in cylindrical coordinates, corresponding to a longitudinal value  $Z$  and an angular value  $\theta$ , a rubber sheet transform similar to an affine transform in the cylindrical IVUS space is sufficient for registration. However, if there exists more than one side-branch, a single affine transform is inadequate to represent possible multiple directions of rotational distortion. Attempting to construct the transform

mations piecewise presents a significant problem in the form of dependencies between the pieces. It was demonstrated that a piecewise affine technique is robust in medical image registration task [9]. Thus our registration task has been broken into two components, computed separately: a longitudinal alignment transform, computed along the length of the pullback, with a scaling term computed separately for each pair of landmarks; and a cross-sectional rotational transform, computed using a Catmull-Rom spline [10] with a control point set at each pair of landmarks. This registration design is in accordance with the fact that the scale difference is driven by catheter speed, while the rotational distortion by catheter motion and/or initial position. Note that we chose Catmull-Rom spline because it ensures the spline curve cross the control points.

**Alignment.** Given the  $z$  coordinates of two adjacent landmarks  $lm(i)_{bl}$ ,  $lm(i+1)_{bl}$  from the baseline pullback:  $Z(lm(i)_{bl})$  and  $Z(lm(i+1)_{bl})$ , and the  $z$  coordinates of corresponding follow-up coordinates (landmarks):  $Z(lm(i)_{fu})$  and  $Z(lm(i+1)_{fu})$ , treating the baseline as the reference, the alignment relationship between baseline and follow-up is defined by the following equations:

$$Z^*(j_{fu}) = Z(lm(i)_{fu}) + \frac{Z(j_{bl}) - Z(lm(i)_{bl})}{\delta(lm(i), lm(i+1))} , \quad (1)$$

$$\delta(lm(i), lm(i+1)) = \frac{lm(i+1)_{bl} - lm(i)_{bl}}{lm(i+1)_{fu} - lm(i)_{fu}} , \quad (2)$$

where,  $Z(j_{bl})$  represents the  $z$  coordinate of the  $j$ th image frame located between the two baseline landmarks  $lm(i)_{bl}$ , and  $lm(i+1)_{bl}$ , and  $Z^*(j_{fu})$  is the corresponding  $z$  coordinate in the follow-up pullback.

**Rotation.** The control points for the Catmull-Rom spline are selected by first finding the centroid of the aligned bounding box surrounding each marked side-branch, then computing the angle between the centroids (follow-up is subtracted from base-line). From this angle, a control point value is selected based on the criteria of minimizing the change in angle from the previous control point (i.e., given the circular wrapping nature of angles, if 4 different representations of an angle all transform the follow-up side-branch centroid to the baseline's position, the correct angle should be the one that requires the minimal amount of movement from the previous control point location). The procedure is described in detail in Table 1.

Once obtaining the Catmull-Rom spline interpolation function  $f_b(\cdot)$  based on the control points, it can be used to estimate the rotational distortion  $\theta = f_b(Z^*(j_{fu}))$  for each aligned coordinate  $Z^*(j_{fu})$ .

**Table 1.** Procedure for identifying control points for rotation spline

Given all marked landmarks  $LM \in (lm(i)_{bl}, \dots, lm(N)_{bl}, lm(i)_{fu}, \dots, lm(N)_{fu})$ , where  $N$  is the number of landmarks in a pullback.  
for  $i = 1 : N$ ,  
    Compute the side-branch angles for each landmark pairs:  $\theta(i)_{bl} = \arctan(C\_y(i)_{bl}, C\_x(i)_{bl})$ ,  $\theta(i)_{fu} = \arctan(C\_y(i)_{fu}, C\_x(i)_{fu})$ , where  $C\_y$  and  $C\_x$  are the y and x coordinates of side-branch centroids, respectively;  
    Compute:  $\Delta_0 = \theta(i)_{bl} - \theta(i)_{fu}$ ,  $\Delta_1 = \Delta_0 + 360$ ,  $\Delta_2 = \Delta_0 - 360$ ;  
     $\theta_{\Delta_i} = \underset{\Delta_k, k \in \{1,2,3\}}{\operatorname{argmin}} (\Delta_k - \theta_{\Delta_{i-1}})$ ;  
    ControlPoints[i] =  $\theta_{\Delta_i}$ ;  
end

### 3 Experiments

#### 3.1 Data

Data used in this study were taken from the HEAVEN study [11] which contains paired baseline and twelve-month (9-21 months) follow-up IVUS data from patients with stable angina. The IVUS phased-array 20MHz probe (Eagle Eye, Volcano Corporation, Rancho Cordova, CA, USA) with automatic pullback (research pullback, model R-100) at 0.5 mm/s was performed through the coronary artery. A subset of 31 cases (one vessel per patient) where the data was of sufficient image and R-wave gating quality, with a minimum of 25 mm overlap between baseline and follow-up pullbacks, was selected to perform our registration experiment.

#### 3.2 Software Tool

We developed a semi-automated software tool for IVUS registration. For the current version, only side-branches are used as anchors. Other landmarks are identified in terms of the user defined locations, but the identification is coarser. With our tool, upon load, a list of both baseline and follow-up branches previously obtained as described in section 2.1 is displayed. When the user selects a branch, the program navigates to it, and then highlights all branches in the opposite pullback as cursors which can be selected to indicate a match. Once a sufficient number of corresponding branches have been marked by the user, the frame correspondences are determined by our automated registration method (if two branches overlap along the longitudinal direction, it is unnecessary to mark both). Fig. 1(a) shows the software interface and the pullback images before registration, while Fig. 1(b) shows the appearance of the image after the registration transform.

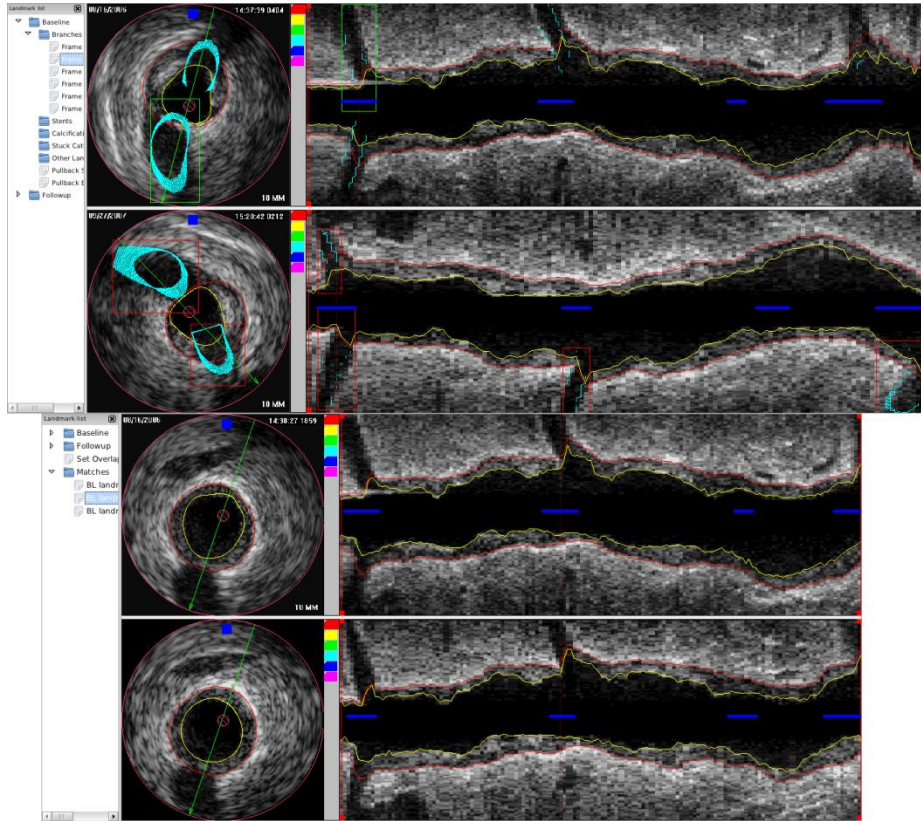


**Fig. 1.** IVUS registration. Upper figure: Tool used to capture landmark correspondence. The upper part is the baseline pullback and the lower one is the original follow-up pullback. Green boxes mark the branch selected from the tree control on the left. Red boxes represent all available branches in the opposite pullback for matching. Light blue contours are 3D branch meshes overlaid on 2D cross-sectional images. Lower figure: Patient depicted in the upper figure, after the registration transform is applied to the follow-up pullback, cropping both pullbacks to the overlapping region.

### 3.3 Results

**Sample Qualitative Results.** Verification of the registration algorithm was first performed by visually examining the image warping and border displacement that was performed with the computed transformation. The lumen and adventitia borders were obtained using a well validated computer-aided IVUS segmentation tool [12] by expert cardiologist. Fig. 2 shows two examples of registration results in longitudinal view. In Fig. 2(a), the visual inspection looks correct even when artifact exists in the lumen region. In Fig. 2(b), registration errors which may have been caused by a stuck/accelerated transducer can be observed in the right part (i.e., the proximal end) of the pullbacks. Corresponding to Fig. 2, Fig. 3 provides examples of registration results obtained in cross-sectional view. For example, in Fig. 3(a), from left to right

are baseline image frame (located at the green dash lines in Fig. 2(a)), unregistered follow-up frame (the same z coordinate with baseline frame), linear fitting frame (as mentioned in [4]), and our registered frame, respectively. Since pullbacks are approximately one year apart, and therefore some physiological change is inevitable, we do not expect a zero error registration. However, we seek to demonstrate a successful minimization of that error.

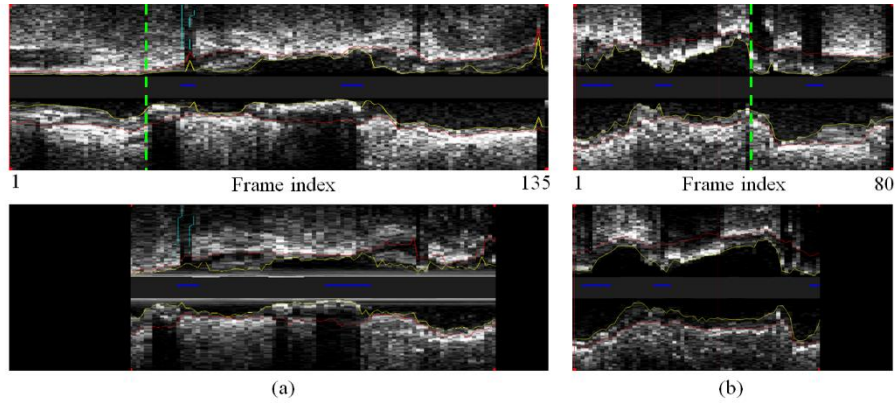


**Fig. 2.** Two examples of registration results in longitudinal view. Upper images are the baseline pullbacks, lower ones are the follow-up pullbacks. (a) A good result. (b) Registration error.

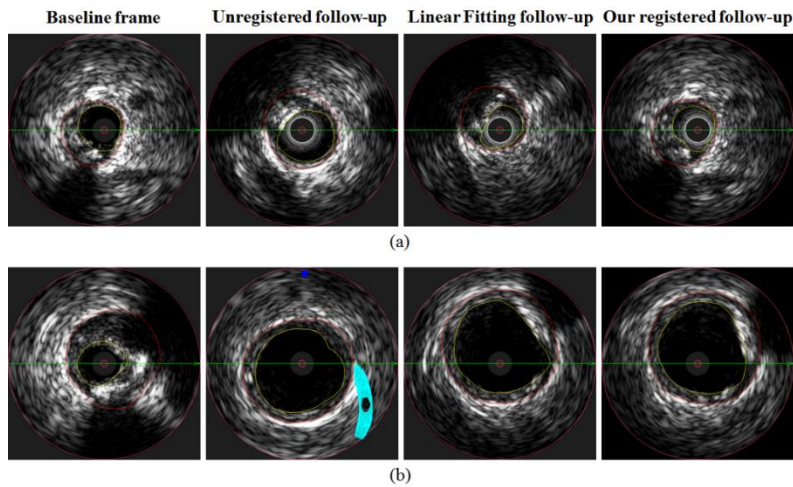


**Fig. 3.** Cross-sectional IVUS images. (a) From left to right: a baseline frame indicated by the green dash line in Fig. 2(a); its corresponding follow-up unregistered frame, linear fitting frame, and our registered frame, respectively. (b) Corresponds to the case in Fig. 2(b).

**Quantitative Results.** For quantitative evaluation, the metrics of the registration accuracy are built upon a comparison of the morphological and VH indices between baseline and follow-up post registration. Most of the indices are those generally ac-

cepted as reflecting local vascular disease severity and were utilized in the analysis of coronary wall properties in previous studies [1-3, 13]. Registered and unregistered differences are evaluated in our analysis. Fig. 4 shows all these indices registered versus unregistered on all 31 IVUS pullback pairs, normalized against the maximum value of each to facilitate visual comparison. It is quite clear that the discrepancies between pullbacks are dramatically reduced by our proposed registration. Note that these quantitative indices were based on the identified lumen/plaque and media/adventitia interfaces in 2D/3D also by using [12]. We run our C++ code on a 64-bit Windows 7 PC, which has a 3.33 GHz Xeon CPU and 24 GB of RAM. For a gated pullback pair with identified side-branches, the average computation time is less than 3 seconds.

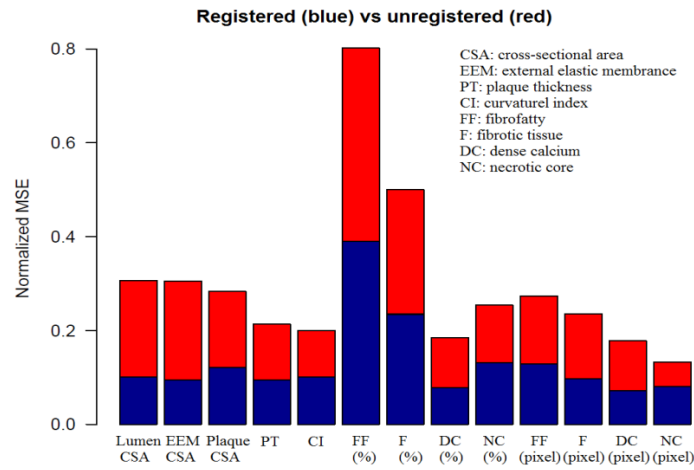


**Fig. 4.** Registered versus unregistered differences across all morphologic and VH indices. Note that all these indices are calculated in wedge-like image sector with 5° central angle.

## 4 Conclusion

In this paper, we propose a two-step approach which first uses a piecewise transform to scale the coordinates along the longitudinal direction and then applies a Catmull-Rom spline generated rotational shift to compensate for rotational variation between the baseline and follow-up IVUS pullbacks. Experimental results on 31 IVUS pullback pairs demonstrate that the proposed method is efficient and robust, which is achieved by registration guided by side-branches, given existing techniques more often rely on the segmentation of IVUS images and the recognition of plaque components. Hence our method is more efficient, and robust to morphologic and plaque component variations frequently present in longitudinal studies. In our future work, we plan to use image matching approaches to refine the unreliable alignment and rotation results which are caused by stuck/accelerated transducer pullback and/or angular twisting between consecutive images.

## Reference

1. Stone, G. W., Maehara, A., Lansky, A. J., de Bruyne, B., Cristea, E., Mintz, G. S., Mehran, R., McPherson, J., Farhat, N., Marso, S. P., et al.: A prospective natural-history study of coronary atherosclerosis. *New England Journal of Medicine*, 364(3), 226-235 (2011)
2. Samady, H., Eshtehardi, P., McDaniel, M. C., Suo, J., Dhawan, S. S., Maynard, C., Timmins, L. H., Quyyumi, A. A., Giddens, D. P.: Coronary artery wall shear stress is associated with progression and transformation of atherosclerotic plaque and arterial remodeling in patients with coronary artery disease. *Circulation*, 124(7), 779-788 (2011)
3. Stone, P. H., Saito, S., Takahashi, S., Makita, Y., Nakamura, S., Kawasaki, T., Takahashi, A., Katsuki, T., Nakamura, S., Namiki, A., et al.: Prediction of progression of coronary artery disease and clinical outcomes using vascular profiling of endothelial shear stress and arterial plaque characteristics: the prediction study. *Circulation*, 126(2), 172-181 (2012)
4. Alberti, M., Balocco, S., Carrillo, X., Mauri, J., Radeva, P.: Automatic Non-rigid Temporal Alignment of Intravascular Ultrasound Sequences: Method and Quantitative Validation. *Ultrasound in Medicine and Biology*, 39(9), 1698-1712 (2013)
5. Timmins, L., Suever, J., Eshtehardi, P., McDaniel, M., Oshinski, J., Samady, H., Giddens, D.: Framework to Co-register Longitudinal Virtual Histology-Intravascular Ultrasound Data in the Circumferential Direction. *IEEE Transactions on Medical Imaging*, 32(11), 1989-1996 (2013)
6. Nair, A., Kuban, B. D., Tuzcu, E. M., Schoenhagen, P., Nissen, S. E., Vince, D. G.: Coronary plaque classification with intravascular ultrasound radiofrequency data analysis. *Circulation*, 106(17), 2200-2206 (2002)
7. Vukicevic, A. M., Stepanovic, N. M., Jovicic, G. R., Apostolovic, S. R., Filipovic, N. D.: Computer methods for follow-up study of hemodynamic and disease progression in the stented coronary artery by fusing IVUS and X-ray angiography. *Medical & Biological Engineering & Computing*, 52(6), 539-556 (2014)
8. Downe, R. W., Wahle, A., Garvin, J., Kovárník, T., Hofk, J., Lopez, J. J., Sonka, M.: Identification and 3-D modeling of coronary branches in intravascular ultrasound. In *MICCAI Workshop in Computation and Visualization for (Intra) Vascular Imaging*, CVII 2011, pp. 15-22 (2011)
9. Audette, M. A., Brooks, R., Funnell, R., Strauss, G., Arbel, T.: Piecewise affine initialized spline-based patient-specific registration of a high-resolution ear model for surgical guidance. In *MICCAI Workshop in Image Guidance and Computer Assistance for Soft-Tissue Interventions*, IGSTI 2008, pp. 1-10 (2008)
10. Catmull, E., Rom, R.: A class of local interpolating splines. *Computer Aided Geometric Design*, 74, 317-326 (1974)
11. Kovarnik, T., Mintz, G. S., Skalicka, H., Kral, A., Horak, J., Skulec, R., Uhrova, J., Martasek, P., Downe, R. W., Wahle, A., et al.: Virtual histology evaluation of atherosclerosis regression during atorvastatin and ezetimibe administration. *Circulation Journal*, 76(1), 176-183 (2011)
12. Sun, S., Sonka, M., Beichel, R.: Graph-Based IVUS Segmentation with Efficient Computer-Aided Refinement. *IEEE Transactions on Medical Imaging*, 32(8), 1536-1549 (2013)
13. Wahle, A., Lopez, J. J., Olszewski, M. E., Vigmostad, S. C., Chandran, K. B., Rossen, J. D., Sonka, M.: Plaque development, vessel curvature, and wall shear stress in coronary arteries assessed by X-ray angiography and intravascular ultrasound. *Medical image analysis*, 10(4), 615-631 (2006)

# Using spatiotemporal patterns of the arterial wall to assist treatment selection for carotid atherosclerosis

Aimilia Gastouniotti, Marinos Prevenios, and Konstantina S. Nikita

School of Electrical and Computer Engineering, National Technical University of Athens, Greece, [gaimilia@biosim.ntua.gr](mailto:gaimilia@biosim.ntua.gr)

**Abstract.** This work addressed a major clinical challenge, namely valid treatment planning for carotid atherosclerosis (CA). To this end, it introduced a novel computer-aided-diagnosis (CAD) scheme, which relies on the analysis of ultrasound videos to stratify patient risk. Based on Hidden Markov Models (HMM), it is guided by spatiotemporal patterns representing motion and strain activity in the arterial wall and it acts as a voice-recognition analogue. The designed CAD scheme was optimized and evaluated on a dataset of 96 high- and low-risk patients with CA, by investigating patterns with the strongest discrimination power and the optimal HMM parameterization. It was concluded that the optimized CAD scheme provides a CAD response with accuracy between 76% and 79%. The introduced CAD scheme may serve as a valuable tool in the routine clinical practice for CA toward personalized and valid therapeutic decision for the disease.

**Keywords:** carotid atherosclerosis; computer-aided diagnosis; ultrasound; motion patterns; Hidden Markov Models

## 1 Introduction

Carotid atherosclerosis (CA) is a chronic degenerative disease, gradually resulting in the formation of lesions (plaques) in the inner lining of the carotid artery. The fact that (a) CA is the main cause for stroke, (b) the morbidity, disability and mortality rates associated with stroke are increased, and (c) the current clinical practice for treatment selection (TR1: carotid revascularization or TR2: conservative therapy) has proved insufficient, poses the development of computer-aided-diagnosis (CAD) schemes for CA among the current major clinical needs [1].

Traditionally, vascular physicians select ultrasound (US) examination in diagnosis and follow-up for patients with CA. Moreover, the use of affordable imaging techniques, such as US, in CAD is a crucial factor. Therefore, US image analysis allows to upgrade the potential of a low-cost routine examination into a powerful tool for objective and personalized clinical assessment, i.e. risk stratification in atherosclerotic lesions. As a result, the development of CAD schemes,

which are based on US image analysis, is considered a grand challenge by the scientific community [2].

Although arterial wall dynamics constitute the direct mechanism for neurological disorders of CA, the role of motion features in CAD remains almost unexplored [2]. A few studies have investigated potential motion-based risk indices [3], while the incorporation of such indices in CAD schemes was recently attempted for the first time [4]. However, none of the related studies has investigated the role of motion patterns of the arterial wall in discriminating vulnerable atherosclerotic lesions.

This study focuses on arterial-wall spatiotemporal patterns, rather than mere motion indices, in an attempt to further elucidate the potential of arterial wall dynamics in CAD for CA toward enhancing validity in treatment planning. To this end, it designs a novel CAD scheme, which combines the analysis of US image sequences (videos) with Hidden Markov Models (HMM) and it is guided by spatiotemporal patterns representing kinematic and strain activity in the arterial wall. The designed CAD scheme is applied to US video recordings of 96 high- and low-risk patients with CA to identify the optimal parameterization for HMM and the spatiotemporal patterns with the strongest discrimination power.

## 2 Material & Methods

The proposed CAD scheme relies on ultrasound-video-based spatiotemporal patterns of the arterial wall to characterize a patient as high- or low-risk, and accordingly advise on the most suitable therapy (Fig. 1). In correspondence with a voice-recognition system, the arterial wall dynamics which account for stable or vulnerable atherosclerotic lesions vary among patients, in the same way as identical words can be pronounced in different ways by humans with different voices. The spatiotemporal patterns correspond to the words (sets of phonemes) and a lexicon attributes the label "high-risk" or "low-risk" patient (or equivalently "TR1" or "TR2") to each word. The design principles of the CAD scheme, as well as the optimization and evaluation procedures which were followed to investigate its potential, are hereafter presented in detail.

### 2.1 Design Issues

Motion analysis is performed for five regions of interest (ROIs) on a B-mode US video of a longitudinal section of the arterial wall (Fig. 1). The particular imaging modality allows the estimation of tissue motion in two dimensions, namely longitudinal, i.e. along the vessel axis, and radial, i.e. along the vessel radius. The five ROIs are the posterior (PWL) and anterior wall-lumen (AWL) interfaces, the plaque top (PTS) and bottom surfaces (PBS), and the plaque region which is contoured by PTS and PBS.

All pixels composing the five ROIs are selected as motion targets. From the target-wise radial and longitudinal motion waveforms which are produced using  $ABM_{KF-K2}$  [3], 146 spatiotemporal patterns (120 kinematic and 26 strain

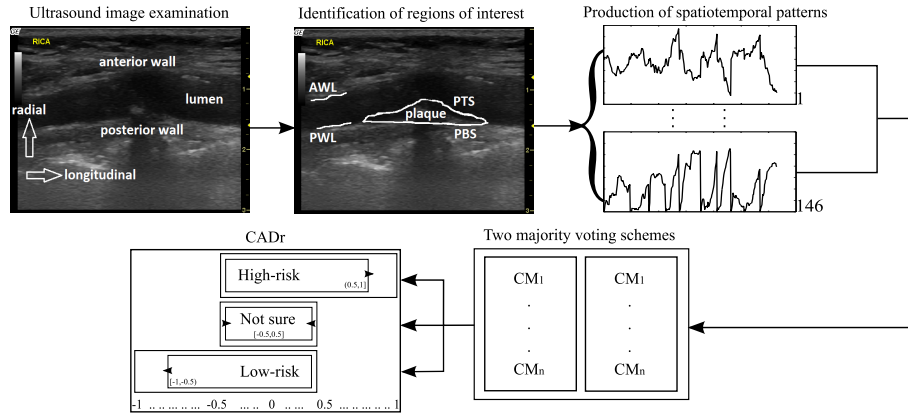


Fig. 1: Workflow for generating a CAD response (CADr) using ultrasound-video-based spatiotemporal patterns of the arterial wall. CM: classification model.

waveforms) are estimated according to the schematic representation in Fig. 2. Specifically, 24 kinematic waveforms are produced for each ROI by estimating target-wise velocity and displacement waveforms and then computing the mean and median waveforms over space (Fig. 2(a)). Based on similar steps and recently published mathematical formulas [5], strain waveforms are produced to express relative movements between (a) PWL and AWL, (b) PBS and PTS, (c) PBS and PWL or AWL, and (d) PTS and PWL or AWL (if the plaque was located at the posterior or the anterior wall, respectively), and local deformations in PWL, AWL, and PTS (Fig. 2(b)).

The stage of patient characterization as "high-risk" or "low-risk" is implemented with two majority voting schemes, each of which is fed with a subset of  $n$  spatiotemporal patterns (with  $n \leq 146$ ) and is based on  $n$  classification models (one for each spatiotemporal pattern). Each classification model is an implementation of an HMM, a stochastic state automaton, which, if properly trained, can decode an observation sequence (word) and hence recognize its underlying patterns [6]. Due to the periodic nature of arterial wall motion, the spatiotemporal patterns are periodically reproduced. Therefore, a left-to-right HMM, consisting of five states, was considered a suitable choice [7].

The first voting scheme generates the probability of the patient belonging in the "high-risk" group ( $V_1$ ), while the second one estimates the probability to be in "low-risk" ( $V_2$ ). The vote of each scheme ( $V_j$ , with  $j \in \{1, 2\}$ ) is estimated using the classification outputs,  $p \in \{0 : \text{false}, 1 : \text{true}\}$ , and some weights,  $w \in [0, 1]$ , of the classification models (eq. (1)). The final CAD response (CADr) is produced using eq. (2), with "-1", "0", and "1" representing "low-risk", "not sure", and "high-risk" potential results, respectively. The values of the parameters  $n$  and  $w$  were defined based on the optimization and evaluation results (for more details, see sections 2.2 and 3).

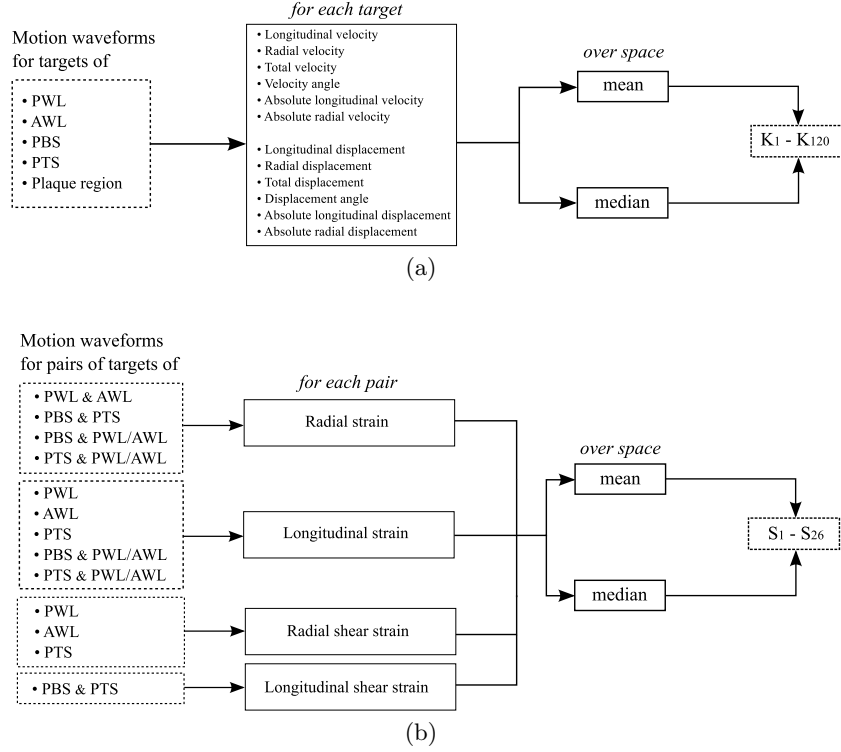


Fig. 2: Schematic representation of the production of (a) 120 kinematic and (b) 26 strain waveforms. PWL, AWL, PBS, and PTS are defined in text.

$$V_1 = \left[ \frac{\sum_{i=1}^n (p_i w_i)}{n} \right] \in [0, 1], \quad V_2 = - \left[ \frac{\sum_{i=1}^n (p_i w_i)}{n} \right] \in [-1, 0] \quad (1)$$

$$CADr = \text{round\_to\_integer} \left( V_1 + V_2 \right) \in \{-1, 0, 1\} \quad (2)$$

## 2.2 Optimization & Evaluation

The optimization and evaluation of the designed scheme relied on spatiotemporal patterns for 96 patients (aged 50–90 years) with established CA (stenosis >50%) [4]. For each patient, the carotid artery was scanned in the longitudinal direction according to a standardized protocol (transducer, linear array 12 MHz; dynamic range, 60 dB; persistence, low) and a B-mode US video was recorded at a rate higher than 25 frames/s for at least 3 (2–3 consecutive cardiac cycles). Among those patients, 20 had experienced an ischemic cerebrovascular event (stroke or transient ischemic attack) associated with the carotid stenosis (“high-risk”

group), while 76 had no neurological symptoms ("low-risk" group) within a 6-month time period from the time of examination.

HMMs were implemented using the HTK Speech Recognition Toolkit, in which input signals are first sampled and converted to Mel-frequency cepstral coefficients; training is achieved through the Baum-Welch method, which has been employed successfully in cardiovascular applications [7,8]. In this study, a separate HMM model was implemented for each type of spatiotemporal pattern and it was fed with the corresponding waveforms for all patients. Each HMM was parameterized in terms of (a) the implementation with monophones or triphones, where each word consists of three or nine phonemes, respectively, and (b) the preprocessing stage. The latter parameter involved two scenarios, in which the spatiotemporal patterns were (1) scaled and (2) not scaled in time to the maximum video duration among all patients. The optimization of each HMM lied in the maximization of the classification accuracy (i.e. percentage of correctly classified cases) for the corresponding spatiotemporal pattern, which was measured using leave-one-out cross validation [9]. In leave-one-out, a single observation (patient) is used as the testing sample, and the remaining observations compose the training dataset; this is repeated (round robin) such that each observation is used once as the testing sample.

### 3 Results

Fig. 3 is a graphical presentation of the maximum classification accuracy, which was achieved for each spatiotemporal pattern by the corresponding optimized HMM. The classification performance ranged between 57% and 81%, and the average performance (over the 146 spatiotemporal patterns) was 70%.

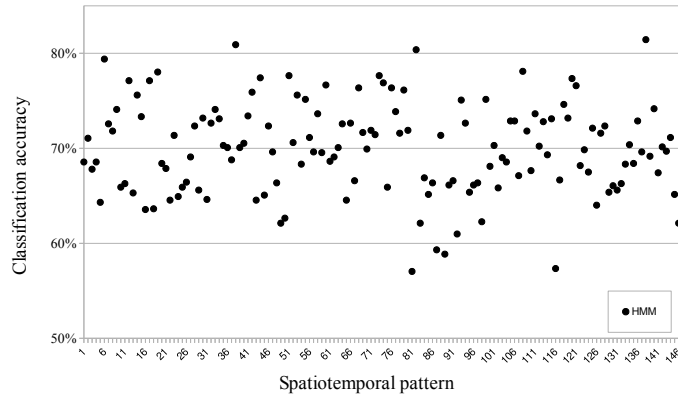
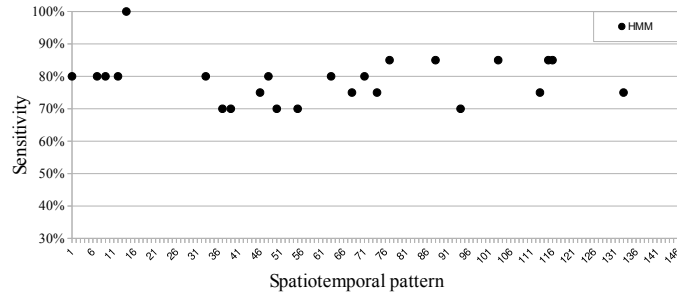


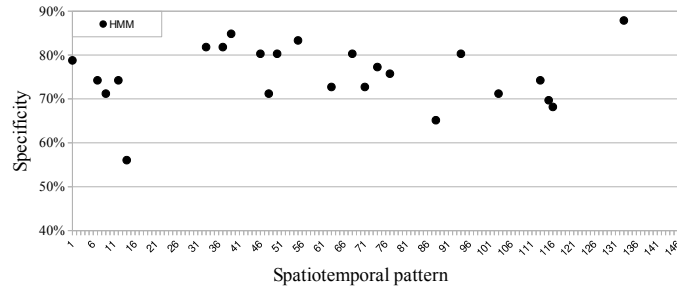
Fig. 3: Maximum classification accuracy for each type of spatiotemporal pattern of the arterial wall, using the corresponding optimized HMM.

Among all spatiotemporal patterns, we identified those with the strongest discrimination power (fig. 4), i.e. those which yielded a high ( $> 75\%$ ) average value of specificity (i.e. correctly classified "low-risk" cases) and sensitivity (i.e. correctly classified "high-risk" cases). For those  $n = 24$  spatiotemporal patterns, Table 1 includes a short description, the most suitable HMM parameterization according to the optimization procedures, and the corresponding sensitivity and specificity results.

Based on the above results, the majority voting schemes of the final CAD scheme are fed with the spatiotemporal patterns of Table 1, they consist of the corresponding optimized HMMs, and the weights  $w$  in  $V_1$  and  $V_2$  (eq. (1)) equal the corresponding sensitivity and specificity values, respectively.



(a)



(b)

Fig. 4: Zoom in the (a) sensitivity and (b) specificity values for the spatiotemporal patterns with the strongest discrimination power.

## 4 Discussion

This work addressed a major clinical challenge, namely valid treatment planning for CA. In this direction, it introduced a novel image-driven CAD scheme, which

Table 1: 24 spatiotemporal patterns with the strongest discrimination power. For each case, the encoding of the pattern according to Fig. 2, a short description, and the specificity and sensitivity values which were achieved by the corresponding HMM (together with the corresponding parameterization) are presented.

Spatiotemporal pattern				Performance		HMM
#	Description			Specificity	Sensitivity	parameterization
K1	PWL	[mean]	LV	80.30%	70.00%	nt1
K18	PWL	[median]	abs. RV	71.21%	85.00%	ts1
K20	PWL	[median]	RD	74.24%	75.00%	ts1
K21	PWL	[median]	TD	68.18%	85.00%	ts1
K24	PWL	[median]	abs. RD	69.70%	85.00%	ts1
K36	AWL	[mean]	abs. RD	87.88%	75.00%	ts1
K57	PBS	[mean]	TD	80.30%	75.00%	ts1
K60	PBS	[mean]	abs. RD	83.33%	70.00%	ts1
K64	PBS	[median]	VA	72.73%	80.00%	ts1
K68	PBS	[median]	RD	72.73%	80.00%	ts1
K69	PBS	[median]	TD	77.27%	75.00%	ts1
K76	PTS	[mean]	VA	81.82%	80.00%	ts1
K88	PTS	[median]	VA	84.85%	70.00%	ts1
K90	PTS	[median]	abs. RV	81.82%	70.00%	ts1
K91	PTS	[median]	LD	80.30%	75.00%	ts1
K94	PTS	[median]	TD	80.30%	70.00%	ts1
K95	PTS	[median]	abs. LD	71.21%	80.00%	ts1
K100	plaque	[mean]	VA	78.79%	80.00%	nt1
K104	plaque	[mean]	RD	71.21%	80.00%	ts1
K105	plaque	[mean]	TD	74.24%	80.00%	ts1
K112	plaque	[median]	VA	74.24%	80.00%	nt1
K115	plaque	[median]	LD	56.06%	100.0%	ts1
S1	PWL & AWL	[mean]	RS	65.15%	85.00%	ts1
S18	PTS & PWL	[median]	LS	75.76%	85.00%	nt1
<b>Average value</b>				<b>76%</b>	<b>79%</b>	

L: longitudinal; R: radial; T: total; (for  $x=\{L,R,T\}$ )  $xS$ :  $x$  strain;  $xD$ :  $x$  displacement;  $xV$ :  $x$  velocity; DA: displacement angle; VA: velocity angle; **HMM**  $\{(ts1)$ : monophones, time-scaling;  $(nt1)$ : monophones, no time-scaling $\}$ ;

incorporates spatiotemporal patterns of the arterial wall, in a framework of a voice-recognition analogue. This implementation allowed for elucidating the role of motion features, and in particular kinematic and strain patterns rather than mere mobility indices, in risk stratification in CA. To the best of the authors' knowledge, no similar attempts have been reported in the literature.

The proposed CAD scheme is able to assist treatment selection with accuracy between 76% and 79% (Table 1). Given the results presented by related studies in the field [2] and the CAD performance of the existing clinical practice on the same dataset [4], the aforementioned results are very encouraging for the potential of arterial-wall-motion patterns in CAD for CA. The final CAD scheme relies on 22 kinematic and 2 strain patterns which are related with the mobility of all the selected ROIs. This conclusion further reinforces the argument that the motion activity of the atherosclerotic lesion itself and healthy parts of the wall close to the lesion are equally important in risk stratification in the disease [3], [4].

A significant contribution of this study with respect to the related literature is that it suggested that the phenotype of high- and low-risk CA differs in terms of not only mobility indices describing motion properties, but also in motion trajectories and strain patterns. This conclusion remains to be further investigated in future studies on larger datasets, which will reveal the full potential of the

presented approach. In the same line of work, the effect of input variability (ex. frequency and frame rate in US image recordings) on HMM performance will be examined, as well.

In conclusion, the introduced CAD scheme may serve as a valuable tool in the routine clinical practice for CA, while it could be further enriched with other temporal features, such as the arterial pressure and heart rate. Both the design principles and the results of this study are expected to motivate the incorporation of motion analysis and spatiotemporal patterns in future related studies designing CAD tools for CA toward valid discrimination of patients in high-risk for stroke, which need to undergo carotid revascularization to prevent neurological disorders, from low-risk ones, who should avoid unnecessary interventions.

**Acknowledgements.** This work was supported in part by the Operational Program "Competitiveness and Entrepreneurship" and Regional Operational Programmes of the National Strategic Reference Framework 2007-2013 and "SYNERGASIA: Collaborative projects of small and medium scale". The work of A. Gastounioti was supported in part by a scholarship from the Hellenic State Scholarships Foundation.

## References

1. A. Ross Naylor, "Time to rethink management strategies in asymptomatic carotid artery disease," *Nat Rev Cardiol*, vol. 9, pp. 116–124, 2012.
2. S. Golemati, A. Gastounioti, and K. S. Nikita, "Toward novel noninvasive and low-cost markers for predicting strokes in asymptomatic carotid atherosclerosis: the role of ultrasound image analysis," *IEEE Trans Biomed Eng*, vol. 60, no. 3, pp. 652–658, 2013.
3. A. Gastounioti, S. Golemati, J. S. Stoitsis, and K. S. Nikita, "Adaptive block matching methods for carotid artery wall motion estimation from b-mode ultrasound: in silico evaluation and in vivo application," *Phys Med Biol*, vol. 58, no. 24, pp. 8647–8661, 2013.
4. A. Gastounioti, V. Koliass, S. Golemati, and et al., "Carotid - a web-based platform for optimal personalized management of atherosclerotic patients," *Comput Meth Programs Biomed*, vol. 114, no. 2, pp. 183–193, 2014.
5. S. Golemati, J. S. Stoitsis, A. Gastounioti, A. C. Dimopoulos, V. Koropouli, and K. S. Nikita, "Comparison of block-matching and differential methods for motion analysis of the carotid artery wall from ultrasound images," *IEEE Trans Inf Technol Biomed*, vol. 16, no. 5, pp. 852–858, 2012.
6. R. O. Duda, P. E. Hart, and D. H. Stork, *Pattern Classification*. Wiley Interscience, 2000.
7. R. V. Andreyo, B. Dorizzi, and J. Boudy, "Ecg signal analysis through hidden markov models," *IEEE Trans Biomed Eng*, vol. 53, no. 8, pp. 1541–1549, 2006.
8. V. Baier, M. Baumert, P. Caminal, M. Vallverdu, R. Faber, and A. Voss, "Hidden markov models based on symbolic dynamics for statistical modeling of cardiovascular control in hypertensive pregnancy disorders," *IEEE Trans Biomed Eng*, vol. 53, no. 1, pp. 140–143, 2006.
9. P. Refaeilzadeh, L. Tang, and H. Liu, *Cross-Validation. Encyclopedia of Database Systems*. Springer US, 2009.

# Towards blood flow quantification using dense flow volumes

Peter Maday, Markus Kowarschik, Stefanie Demirci, and Nassir Navab

<sup>1</sup> Chair for Computer Aided Medical Procedures (CAMP), TU Munich, Germany  
{peter.maday, stefanie.demirci, nassir.navab}@tum.de

<sup>2</sup> Siemens AG, Healthcare Sector, Angiography & Interventional X-Ray Systems,  
Forchheim, Germany {markus.kowarschik}@siemens.com

**Abstract.** We propose a method for extracting quantitative hemodynamic information, such as the time varying volumetric flow rate from image sequences in the form of 2D Digital Subtraction Angiography (DSA) acquisitions. An intermediary 3D+t image representation is created by backprojecting the 2D intensities to a working volume. Dense 3D flow field estimation adapted to the tubular vascular geometries, is then used to recover displacement fields representing fluid motion. Whereas previous related attempts performed calculation within the 2D image domain only, our proposed method quantifies blood flow directly within the 3D vascular representation, which allows constraints motivated by physical principles, to be applied for regularization. From the extracted dense 3D flow fields, quantities of clinical interest such as the volumetric flow rate are derived. Our experimental setup for validating our proposed algorithm involves synthetic and phantom datasets. Whereas the phantom data results only allows for qualitative result inspection due to missing ground truth information, for the synthetic cases, flow rate measurements are quantitatively validated.

## 1 Introduction

Cerebrovascular diseases such as aneurysms, arteriovenous malformations (AVMs), and stenoses impose significant health risks to the population. Decreased oxygen supply and an elevated risk of haemorrhage are only a couple of potential consequences induced by changes in local hemodynamics resulting from alterations in vascular morphology. To combat these adversarial effects and restore healthy flow rates, minimally invasive catheterization procedures are routinely considered. Here, endovascular tools such as guide wires and catheters, are introduced into the vascular system under continuous X-ray imaging. Further injection of radio opaque dye (contrast agent) makes translucent vessels visible and gives insight into pathological findings in more detail. This imaging technique is called X-ray angiography.

Observing the evolution of contrast agent within the vessels, experienced interventionalists are able to gain a qualitative understanding of functional information on blood flow. However, this interpretation is highly subjective. Automated extraction of quantitative information, such as volumetric flow rate,

from angiographic X-ray acquisitions would benefit decision making and improve patient care by providing accurate and reproducible measurements of relevant physiological parameters.

Digital Subtraction Angiography (DSA) provides transmittance images of only the vasculature from either a static view or a rotational trajectory of an angiographic C-arm device.

This is achieved by first acquiring a non-contrasted mask X-ray image sequence only showing background information, which is then subtracted from the frames of the subsequent contrasted angiographic sequence. 2D DSA imaging serves as a good candidate for the flow quantification problem as it is readily available in the clinics and the image intensity distribution incorporates valuable flow information due to the non-uniform mixing of blood with contrast agent. A fundamental shortcoming of 2D planar projection images, however, relates to the well-known angiography artefacts such as vessel overlaps and foreshortening, which may induce intensity values that are no longer in correspondence to flow assumptions.

A complete overview of early developments in quantifying flow behavior based on 2D DSA sequences is given in [1]. A more recent model fitting approach [2] optimizes parameters of a simplified flow model to match the observations. In order to retain tractability of the optimization process the method uses a small number of model parameters, which limits the ability to describe complex inflow patterns.

Transmittance images of fluid flows satisfy certain conservation laws similar to those associated with the brightness constancy assumption (BCA). For this reason, the application of methods that yield dense flow fields and satisfy these laws, serves as a physically plausible basis to recover flow information without enforcing artificial modeling assumptions. Recent development in flat panel detector technology enabling high speed acquisitions, has made the application of techniques capturing inter-frame displacement of fluid elements possible. Previously, a traditional optical flow approach has been pursued to yield dense 2D flow fields that are used as features for detecting flow abnormalities [3]. A more physically correct approach has been introduced in [4], where a modified data term is used in a setup estimating fluid displacement in a 1D modeling domain of the projected vessel centerline. The rationale for the reduced dimensionality is that this way, large fluid displacements can be recovered through the implicit geometrical constraint. An extension to two dimensions has been introduced in [5] employing a coordinate transformation to enable the estimation of fast flows in the original image data. A critical challenge for optical flow approaches operating in the DSA image domain is the projected nature of the data that induces information loss. Flow in complex 3D vascular structures is mapped to a planar domain, and hence, occlusion and foreshortening routinely compromise the interpretation of flow behavior at the affected sites.

4D DSA imaging is a recent development that essentially describes time-resolved 3D reconstructions of the flow volume from 2D DSA projection images. It enables the flow quantification problem to be formulated in three dimen-

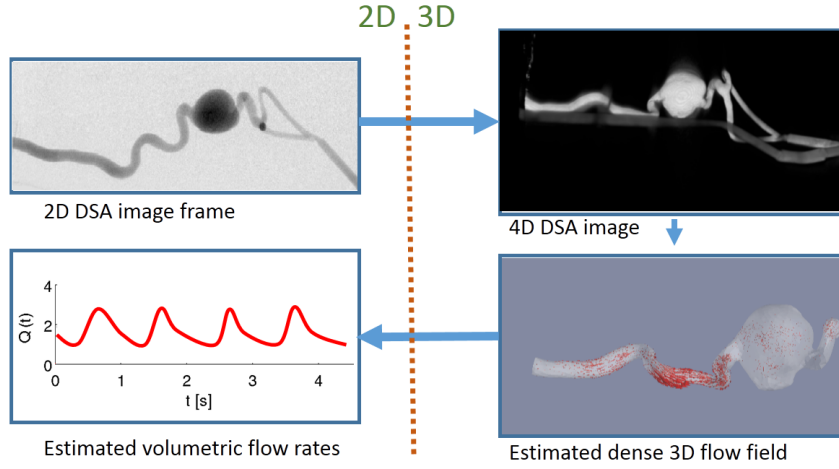


**Fig. 1.** Illustration of the data flow: First an intermediate series of backprojection volumes is created from the DSA images, dense flow fields are then estimated followed by the extraction of flow rates.

sions where the previously mentioned shortcomings of 2D DSA sequences are no longer present. In this paper, for the very first time, we propose an image-based 4D blood flow quantification algorithm yielding dense 3D flow velocity fields. We develop methods to efficiently and robustly recover fluid displacement and derive quantities of clinical interest, such as the volumetric flow rate from 3D+t velocity fields. Employing 3D geometric representation from 4D DSA datasets, our method can overcome limitations of existing 2D approaches for handling occlusions and geometric distortions while expanding the capabilities of flow quantification methods as a higher degree of regularity can be prescribed in the flow solution along the vessels in the reconstructed 3D space.

## 2 Materials and methods

The structure of our proposed image-based flow estimation method is depicted in Fig. 1. A significant contribution of our proposed method is the flow estimation within an intermediary 3D representation. First, 2D projection images showing the inflow of the contrast agent are used to reconstruct a corresponding sequence of 3D volumes (see section 2.1). In a subsequent dense flow estimation step (see section 2.2), 3D+t velocity fields of the imaged fluid are obtained. For this step a computational domain tightly encompassing the vessel tree is considered to enable the enforcement of plausible flow behavior. Finally, we extract volumetric flow rate curves from sites of interest based on the dense flow solution to quantify flow behavior (see section 2.4).

## 2.1 4D DSA

Recent advances in the processing of DSA datasets have made the reconstruction of time resolved 3D image information possible [6]. Unlike traditional static 3D reconstruction, a time varying volume is reconstructed from only one single transmittance image for each individual time instance. For this reason, reliance on strong prior knowledge is necessary to make the reconstruction problem well posed. Here, a static 3D mask of the vessel tree is reconstructed from the rotational planar acquisitions and subsequently used for spatial regularization during the backprojection step. Intensity levels for vessel interior voxels are filled with DSA projection intensities using a multiplicative projection processing step.

The reconstruction step yields volumes where intensity levels are consistent with the observed rotational acquisition of transmittance images. The values from log subtracted DSA images are distributed in space yielding volumes where intensity levels are proportional to the concentration of contrast agent in the voxels.

## 2.2 Dense 4D flow estimation

Intensity values of 2D projection images of 3D fluid flows satisfy a conservation equation of intensity values. In the more general 3D case, this observation is not valid anymore. Instead, assuming contrast agent is a massless fluid transferred by the velocity field of the fluid flow, a continuity law holds. Considering the incompressibility assumption, the conservation relationship reduces to the well known optical flow constraint relating the image  $I$  and its spatial and temporal derivatives as well as the fluid velocity  $\mathbf{v}$  due to the properties of the divergence operator:

$$\nabla \cdot (I\mathbf{v}) + I_t = \nabla I \cdot \mathbf{v} + \underbrace{I\nabla \cdot \mathbf{v}}_{\nabla \cdot \mathbf{v}=0} + I_t = 0 \quad (1)$$

Similar to [4], a physically correct dense flow estimation method can be constructed with the derived data term in Eq. (1). To allow the usage with imperfect data, instead of strict adherence to the constraint, the flow estimation problem is formulated as an energy minimization process, where the global energy depends on both the data term and a regularizer to warrant well-posedness via enforcing smoothness in the flow solutions. For the regularization, the diffusion regularizer is used. It is known that this penalizes curl in the solution, however laminar flow fields in vessels tend to be irrotational.

As described in Section 2.1, 4D DSA data is reconstructed from only one single projection per frame and hence, artifacts are expected to distort intensity values at locations where several vessels overlap. As the flow solution in our method is obtained by minimizing a global energy function, local discrepancies in the intensity values due to the artifacts can be compensated for.

Employing a diffusion regularizer, the optimization problem can be stated as

$$\mathbf{v}_{opt} = \underset{\mathbf{v}}{\operatorname{argmin}} \int_{\Omega} \|\nabla I \cdot \mathbf{v} + \partial_t I\|^2 + \lambda \|\nabla \mathbf{v}\|^2 dx \quad (2)$$

with the flow velocity field  $\mathbf{v}$  and the image  $I$  together with its spatial derivative  $\nabla I$  and temporal derivative  $\partial_t I$ .

The proper treatment of the variational problem requires the specification of boundary conditions that make the minimization problem well posed. The used boundary conditions are derived from physical insights and are defined in the following manner. Due to friction, the fluid velocity right next to the vessel walls is zero and the common no-slip boundary condition can be applied on wall segments in the form of a zero Dirichlet condition. On the other interfaces corresponding to inlets and outlets of the modeled vascular segment, Neumann type conditions are prescribed for the velocity.

### 2.3 Implementation details

**Discretization and numerical solution** For the discretization and numerical solution of the minimization problem in Equ (2), we use a finite element based approach.

To allow for the minimization problem to be solved numerically a discretization of the vessel interior needs to be conducted. First the vessels are segmented using a level-set approach based on a separate 3D rotational angiography (3DRA) reconstruction readily available together with the 4D DSA reconstruction [6]. A tetrahedral volume mesh is then constructed using an adaptive refinement strategy.

In order to represent the problem in a finite element framework the weak form of the minimization problem needs to be derived. By taking the first variation of the energy function in the direction  $\mathbf{v}^*$  and using integration by parts we obtain the following equation:

$$\int_{\Omega} (\mathbf{v} \cdot \nabla I)(\mathbf{v}^* \cdot \nabla I) - \partial_t I \mathbf{v}^* \cdot \nabla I + \lambda \nabla \mathbf{v} : \nabla \mathbf{v}^* dx = 0 \quad (3)$$

Introducing a finite basis and thereby using the finite element approach, an approximation to the solution can be obtained by solving a system of linear equations. This numerical task was solved within the finite element software framework FEniCS [7]. The optimality system was discretized using first order Lagrangian elements for the velocity field  $\mathbf{v}$  and the test function  $\mathbf{v}^*$ . A sparse iterative linear algebra solver (BiCGSTAB) was used to solve the arising linear systems.

The optical flow constraint can be regarded as a linearized version of the brightness constancy assumption, and for this reason, it only holds for small displacements. To overcome this problem, we used an iterative method [8] that accumulates displacement contributions from subsequent solutions to spatially perturbed (warped) versions of the problem.

### 2.4 Flow quantification

Even though reconstruction of the 3D+t flow velocity fields constitutes the backbone of our approach, its purpose is to arrive to a consistent flow solution, from

which quantities of clinical interest can be derived. The volumetric flow rate is an important indicator of local blood supply and is of primary interest for interventionalists. It quantifies the amount of fluid volume that is transferred through vessel cross section interfaces per time unit. It can be computed based on the fluid velocity field by integrating the dot product of the velocity vectors and the surface normal along a test surface:

$$Q(t) = \int_A \mathbf{v} \cdot \mathbf{n} \, dA \quad (4)$$

with  $A$  being a cross sectional interface of the vessel and  $\mathbf{n}$  its normals.

Volumetric flow rates can be considered to be constant along vascular segments assuming incompressibility of the fluid and inelastic vessel walls, and thus can be estimated over arbitrary test surfaces. For practical reasons, we consider the use of planar cross sections perpendicular to the 3D vessel centerlines at various points in the vascular branches.

### 3 Data and Experiments

For the assessment of the proposed flow quantification method, synthetic as well as phantom datasets were considered. Synthetic cases with known ground truth have been generated using CFD simulations with various inflow parameters. Additional flow quantification has been executed on real acquisitions of a vascular bifurcation phantom, where only qualitative assessment is possible due to lack of flow measurements.

**Synthetic cases** A digital model of a straight vascular segment of 4.8 mm diameter was created. Using an in house CFD solver, datasets corresponding to sequences of 4D-DSA intensity volumes as well as flow velocity fields were created. For the simulations, a set of contrast agent and pulsatile blood inflow curves were considered to account for different pulsatility patterns and inflow rates. The total mean inflow rate was set to values ranging from 3 to 7 ml/s in order to yield a total of 15 cases. Given the ground truth flow velocity fields, a quantitative assessment of the accuracy of the mean flow rates could be carried out. The assessment of the accuracy of the method is based on conducting hypothesis testing on the regression slope for a set of grouped cases. Regression lines are fitted to samples of measured - ground truth mean flow rate pairs using robust linear regression. Confidence intervals of 95% on the regression slope are then evaluated to contain the value 1 thus indicating the significance of the findings. Confidence intervals are obtained for 5 groups of samples with increasing max. flowrate ( $\leq 3, \leq 4, \leq 5, \leq 6, \leq 7ml/s$ ) to investigate the impact of flow rates on the accuracy.

**Phantom case** The phantom acquisition of a vascular bifurcation with an aneurysm been made with a Siemens Artis Zeego flat panel detector angiographic

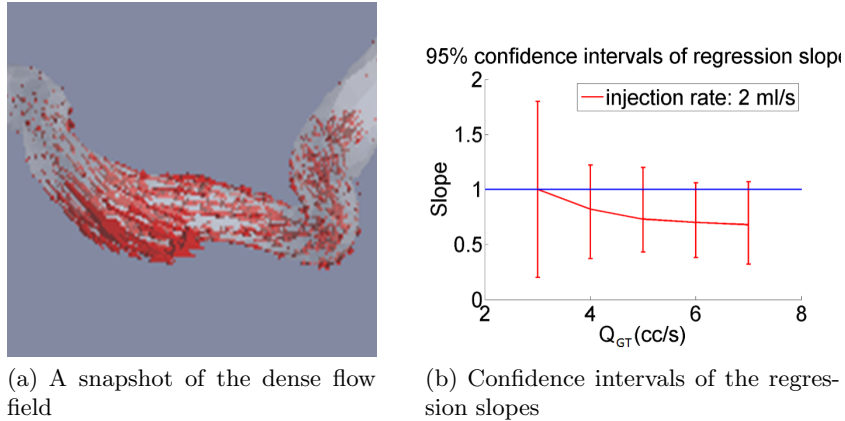


**Fig. 2.** A snapshot of the dense flow field estimated from the phantom dataset (a) Confidence intervals of the regression slopes computed for the different flow rate groups (b).

system. Rotational images for subtracted 3D reconstructions were recovered using an acquisition rate of 30 frames per second. As contrast material iohexol has been used. Due to the lack of flow measurements only qualitative findings are reported for this case.

## 4 Results

Results for the synthetic experiments are illustrated on Fig. 2(b). Confidence intervals of the regression slope for the 95% level are denoted using a box plot. The value 1 is contained in all evaluation groups thus the measured mean flow rates do not deviate from the ground truth significantly. For increasing inflow velocities a slight underestimation of the flow rates is observed.

Flow solutions from the phantom dataset are consistent with the expected flow behavior regarding consistency and orientation, for the 3D flow velocity field an example is shown on Fig 2(a).

## 5 Discussion and Conclusions

We have demonstrated the feasibility of blood flow quantification by means of dense flow estimation from intermediary 3D+t reconstructions. With the results from the synthetic experiments we have illustrated its capabilities to yield accurate flow rate measurements in simple cases using various inflow conditions. Qualitative investigation based on phantom images confirms that using the 3D modeling domain yields smooth and consistent flow solutions in more complex domains as well.

Despite the recent introduction of 4D DSA for clinical purposes, imaging of time resolved 3D fluid velocity fields in the medical context is in its infancy. With the proposal of a 4D blood flow quantification method, we hope to convince and inspire clinicians to conduct 4D DSA imaging.

Even though the purpose of compiling the observations into a time resolved series of 3D flow velocity fields is to allow efficient regularization of the solutions, this step offers more potential than just the extraction of flow rate information. For future work, we aim at providing valuable complementary information such as wall shear stress [9] and pressure [10] measurements in addition to the estimated flow rates.

## References

1. Shpilfoygel, S.D., Close, R.A., Valentino, D.J., Duckwiler, G.R.: X-ray videodensitometric methods for blood flow and velocity measurement: A critical review of literature. *Med Phys* **27**(9) (2000) 2008–2023
2. Waechter, I., Bredno, J., Hermans, R., Weese, J., Barratt, D.C., Hawkes, D.J.: Model-based blood flow quantification from rotational angiography. *Med Imag Anal* **12**(5) (2008) 586–602
3. Wu, T.H., Lin, C.J., Lin, Y.H., Guo, W.Y., Huang, T.C.: Quantitative analysis of digital subtraction angiography using optical flow method on occlusive cerebrovascular disease. *Comput Meth Prog Bio* **111**(3) (2013) 693–700
4. Bonnefous, O., Pereira, V.M., Ouared, R., Brina, O., Aerts, H., Hermans, R., Van Nijnatten, F., Stawiaski, J., Ruijters, D.: Quantification of arterial flow using digital subtraction angiography. *Med Phys* **39**(10) (2012) 6264–6275
5. Maday, P., Brosig, R., Endres, J., Kowarschik, M., Navab, N.: Blood flow quantification using optical flow methods in a body fitted coordinate system. In: *Medical Imaging 2014: Image Processing*. Volume 9034 of Proc. SPIE. (2014) 90340J
6. Davis, B., Royalty, K., Kowarschik, M., Rohkohl, C., Oberstar, E., Aagaard-Kienitz, B., Niemann, D., Ozkan, O., Strother, C., Mistretta, C.: 4d digital subtraction angiography: Implementation and demonstration of feasibility. *Am J Neuroradiol* **34**(10) (2013) 1914–1921
7. Logg, A.: Automating the finite element method. *Arch Comput Method E* **14**(2) (2007) 93–138
8. Brox, T., Bruhn, A., Papenberg, N., Weickert, J.: High accuracy optical flow estimation based on a theory for warping. In: *Computer Vision-ECCV 2004*. Volume 6315 of LNCS., Springer (2004) 25–36
9. Cheng, C.P., Parker, D., Taylor, C.A.: Quantification of wall shear stress in large blood vessels using lagrangian interpolation functions with cine phase-contrast magnetic resonance imaging. *Ann Biomed Eng* **30**(8) (2002) 1020–1032
10. Tyszka, J.M., Laidlaw, D.H., Asa, J.W., Silverman, J.M.: Three-dimensional, time-resolved (4d) relative pressure mapping using magnetic resonance imaging. *J Magn Reso* **12**(2) (2000) 321–329

# HIGHER ORDER TENSOR-BASED SEGMENTATION AND n-FURCATION MODELING OF VASCULAR STRUCTURES

Suheyla Cetin and Gozde Unal

Faculty of Engineering and Natural Sciences, Sabanci University, Turkey  
{suheylacetin,gozdeunal}@sabanciuniv.edu

**Abstract.** A new vascular structure segmentation method, which is based on a cylindrical flux-based higher order tensor (HOT), is presented. On a vessel structure, HOT naturally models branching points, which create challenges for vessel segmentation algorithms. In a general linear HOT model, embedded in 3D, one has to work with an even order tensor due to an enforced antipodal-symmetry on the unit sphere in 3D. However, in scenarios such as in a bifurcation, the antipodally-symmetric tensor models of even order will not be useful. In order to overcome that limitation, we embed the tensor in 4D and obtain a structure that can model asymmetric junction scenarios. Thus, we will demonstrate a seed-based vessel segmentation algorithm, which exploits a 3rd or 4th order tensor constructed in 4D. We validate the algorithm on both synthetic complex vascular structures as well as real coronary artery datasets of the Rotterdam Coronary Artery Algorithm Evaluation framework.

**Keywords:** vessel tree segmentation, higher order tensors (HOT), branch modeling, cylindrical flux, coronary arteries, HOT tractography

## 1 Introduction

Extraction of vascular structures such as coronary and cerebral arteries is an important step in detection and analysis of vessel anomalies and pathologies such as aneurysms, stenoses, and plaques. However, manual segmentation is an exhaustive task for the experts. As solutions to segmentation, first, image filtering and enhancement methods were proposed [1, 2]. Lately, multi-hypotheses tracking [3, 4] and data driven [5] approaches have been suggested for vessel segmentation. A broad review of these methods can be found in [6] and [7] surveys.

Minimal path techniques are another category for vessel extraction [8–10]. For instance, the vessel was modeled as a 4D curve of a centerline and radius in [10]. This approach considered isotropic measurements through a sphere fitted to a vessel. In contrast, the vessel orientation was modeled by adding cylinders to this model, in [11], where an intensity-based rank-2 tensor was fit to a vessel, which mimicked Diffusion Tensor Imaging (DTI). The anisotropic tensor inside the vessel drove the segmentation analogously to a tractography approach in DTI. Although the method in [11] provided advantages in terms of modeling vessel orientational information, for modeling the whole vessel tree, it employed a separate branch detection scheme in order to capture bifurcation points in a vessel. The latter is

due to choice of a rank-2 tensor, which becomes isotropic in bifurcation regions of vessels. Generally, for the problem of patient-specific vascular tree modeling, an initial segmentation step that produces a 3D segmented volume has to be followed by a separate branch detection scheme, which later is used in creation of a vascular tree model, and sometimes followed by an external mesh construction scheme to model n-furcated vessels for mesh editing and further modeling [12, 13].

In recent studies of Diffusion MRI, it has been shown [14, 15] that the rank-2 diffusion tensor model in DTI has limitations, the most important of which occurs when there is orientational heterogeneity of the fibers in the voxel of interest. To overcome this difficulty, [14] proposed high angular resolution diffusion imaging (HARDI), which exploited imaging with diffusion-weighting gradients applied along many directions, distributed isotropically on the unit sphere, and which can better represent the underlying fiber crossings. In addition to usage of generalized higher order tensors in HARDI methods [15, 16], more flexible approaches via orientation distribution functions (ODFs) as an alternative for modeling crossings, were presented [17–19]. However, they require relatively higher number of diffusion directions and a follow-up effort for mode extraction. [18] handles asymmetric situations only via the ODF field by considering inter-voxel information.

In analogy to fiber-crossing locations of white-matter, vascular structures include n-furcations, which are locations where n branches exit from the same vessel point, hence have to be modeled properly. Inspired by the idea of generalized linear tensors in HARDI, we model the n-furcations of the vascular structures using a Higher Order Tensor (HOT), however embedding them in 4D, which is described in § 2. Our technique brings a unified approach to the problem of whole vascular tree extraction, which includes simultaneously modeling both tubular sections and n-furcations of the vascularities. Results are presented and validated in § 3, followed by conclusions in § 4.

## 2 Method

### 2.1 Higher Order Tensor Model in 4D

In HARDI methods, the diffusivity function can be approximated by an  $m^{th}$  order Generalized Cartesian Tensor (GCT) in 3D as follows [15]:

$$S(\mathbf{g}) = \sum_{i=1}^3 \sum_{j=1}^3 \cdots \sum_{k=1}^3 \sum_{l=1}^3 g_i g_j \cdots g_k g_l D_{i,j,\dots,k,l}, \quad (1)$$

where  $g_i$  is the  $i^{th}$  component of the 3D unit vector  $\mathbf{g} \in \mathbb{S}^2$ , and  $D_{i,j,\dots,k,l}$  are the tensor coefficients. Number of indices represents the order of the tensor  $D$ . As can be observed, when  $m$  is odd:  $S(-\mathbf{g}) = -S(\mathbf{g})$ , the GCT model forces negated measurements at the antipodals of the sphere. On the other hand, when  $m$  is even:  $S(-\mathbf{g}) = S(\mathbf{g})$  can not model an antipodal asymmetric situation. For the HARDI application, this was not crucial, as the diffusion measurements are positive and symmetric on the sphere, even order tensors ( $m = 2, 4, 6$ ) were mostly utilized.

In our problem, a GCT in 3D can not model the geometry of the vessel, which is symmetric along the vessel and asymmetric at the bifurcations. In Fig. 1, the

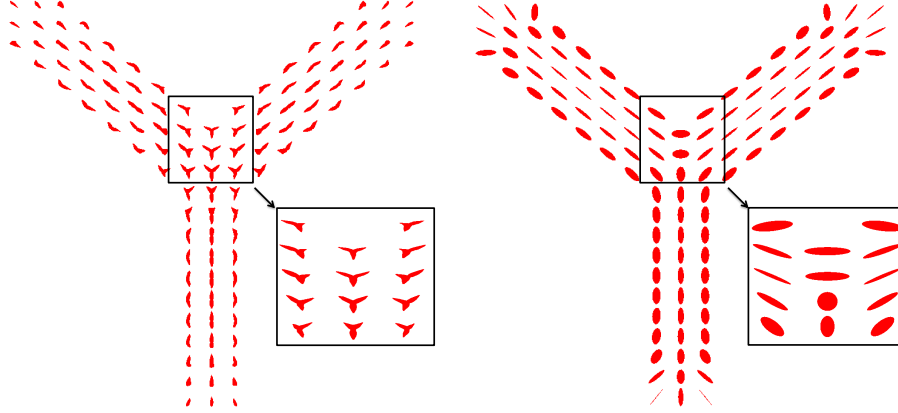


Fig. 1: A  $60 \times 60 \times 60$  synthetic Y-junction volume: Comparison between  $S(\mathbf{g})$  measurements (left) and their rank-2 tensor fit model (right).

measurements  $S(\mathbf{g})$  taken from multiple orientations (described in § 2.2) for a Y-shaped vessel are depicted on the left, and on the right are the corresponding rank-2 tensors fit to  $S(\mathbf{g})$ . As can be observed, although tubular parts of the vessel are correctly represented, rank-2 tensors are not able to model the geometry of bifurcations. Similarly, a rank-4 tensor will not represent the correct geometry of a bifurcation. Furthermore, odd-order GCT in 3D enforces negative measurements at the opposing directions, therefore, is not suitable in this case either.

We suggest a 4D third or fourth order tensor, which is able to model both antipodal asymmetry and symmetry of a vessel n-furcation, where the fourth dimension measurements along  $g_4$  will be used to suppress the components in unwanted directions such as in the opposing directions at Y-junction branches. Mathematically, our tensor model is then described as:

$$S(\mathbf{g}) = \sum_{i=1}^4 \sum_{j=1}^4 \sum_{k=1}^4 g_i g_j g_k D_{i,j,k} \quad \text{or} \quad S(\mathbf{g}) = \sum_{i=1}^4 \sum_{j=1}^4 \sum_{k=1}^4 \sum_{l=1}^4 g_i g_j g_k g_l D_{i,j,k,l}, \quad (2)$$

where  $S(\mathbf{g})$  is a measurement,  $\mathbf{g} = [g_1, g_2, g_3]$  is an orientation vector on the unit sphere  $\mathbb{S}^2$ , and  $g_4$  is defined as follows:

$$g_4(\mathbf{g}) = \frac{1}{1 + e^{(|I(r\mathbf{g} + \mathbf{x}_s) - I(\mathbf{x}_s)|)}}, \quad (3)$$

where  $I$  is the image intensity function ( $I : \mathbb{R}^3 \rightarrow \mathbb{R}$ ),  $\mathbf{x}_s$  is a center point. Note that this model in 4D lifts the limitation with symmetry of measurements, and one can have arbitrary measurements at  $\mathbf{g}$  and  $-\mathbf{g}$  directions for a third order tensor. The absolute intensity variation along the vessel and the branches is expected to be less than the variation in other directions. The function(3) is designed exactly to do that, and measures similarity of the intensity of the centerline coordinate with respect to those of given orientations. Even though the 4th-order tensor still has an antipodal symmetry, the 4th component in 4D, which

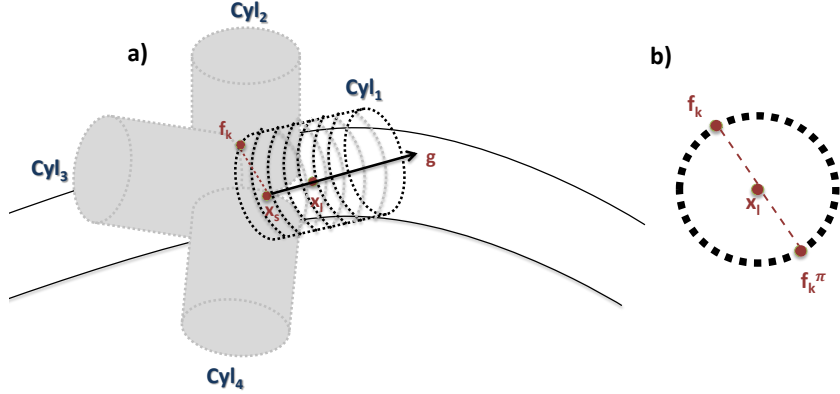


Fig. 2: Illustrations of (a) directional measurement model: each  $Cyl_i$  is characterized by the direction vector  $\mathbf{g}$ , the height  $h$ , and the circle centered at point  $\mathbf{x}_l$  with radius  $r$ ; (b) cross sectional view of the cylindrical model.

acts like a measurement filter, helps in estimation of main branch directions in an  $n$ -furcation. We describe a flux-based intensity model to create measurements  $S(\mathbf{g})$  next.

## 2.2 A Flux-based Measurement Model

A hollow cylinder along each sampled orientation  $\mathbf{g}$  is represented by a stack of circles and denoted as follows:

$$cyl = \bigcup_{l=0, \dots, h} circle(\mathbf{x}_l, r, \mathbf{g}), \quad \mathbf{x}_l = \mathbf{x}_s + \mathbf{g}l, \quad (4)$$

where  $\mathbf{x}_l \in \mathbb{R}^3$  is defined as a point along the centerline of the cylinder,  $\mathbf{g}$  also indicates the normal vector to the circle:  $circle(\mathbf{x}_l, r, \mathbf{g})$  with radius  $r$ , and  $h = 2r$  is defined as the height of the cylinder (see Fig. 2).

Circles that define the cylinder are equi-angularly discretized in polar coordinates. Next, sampling a set of orientation vectors  $\mathbf{g}_i$  over the unit sphere  $\mathbb{S}^2$ , each measurement  $S_i$  at the given direction  $\mathbf{g}_i$  is a flux-based feature, which is modeled by an accumulation of image gradient magnitudes. Mathematically, the measurements along the cylinder are calculated as follows:

$$S_i = \sum_{l=0}^h \left( \frac{2}{N} \sum_{k=1}^{N/2} \max(|\langle \nabla I(\mathbf{f}_k), \mathbf{u}_k \rangle|, |\langle \nabla I(\mathbf{f}_k^\pi), \mathbf{u}_k^\pi \rangle|) \right), \quad (5)$$

where  $\nabla I(\mathbf{f}_k)$  is the image gradient vector at the sampled point  $\mathbf{f}_k$  and  $\mathbf{u}_k = \frac{\mathbf{x}_l - \mathbf{f}_k}{|\mathbf{x}_l - \mathbf{f}_k|}$  (Fig. 2-b). To minimize the effects of the bright structures situated near the vessels, we pair diametrically opposed points as suggested in [3],  $\mathbf{f}_{\frac{N}{2}+k} = \mathbf{f}_k^\pi$ . Although the idea is similar to the original flux function [3], which calculates the

flux around a cross section, our measurements are less sensitive to noise due to the introduced cylindrical model. After the flux-based measurements  $S_i$  for each  $g_i$  are computed, a radius is estimated using the technique described in [11].

### 2.3 Higher Order Tensor Fitting and Decomposition

In this paper, we chose to exemplify  $m = 4^{th}$  order tensor estimation in 4D to be able to model up to a trifurcation. To fit a 4D fourth order tensor to the measurements: first, we stack the components of the tensor, and due to permutational symmetry ( $D_{1112} = D_{1121} = D_{1211} = D_{2111}$ ), there exists 35 components in total:

$$\mathbf{d} = [D_{1111} \ D_{2222} \ D_{3333} \ D_{4444} \ D_{1112} \ D_{1113} \ D_{1114} \ D_{2221} \ D_{2223} \ \cdots \ D_{1234}]^T. \quad (6)$$

We re-arrange Eq. (2) to get

$$S_i = \mathbf{G}_i \mathbf{d}, \quad (7)$$

where  $\mathbf{G}_i$  is the  $i^{th}$  row of the matrix, which is constructed as follows:

$$\mathbf{G}_i = [g_{i1}^4 \ g_{i2}^4 \ g_{i3}^4 \ g_{i4}^4 \ 4g_{i1}^3 g_{i2} \ 4g_{i1}^3 g_{i3} \ 4g_{i1}^3 g_{i4} \ 4g_{i2}^3 g_{i1} \ 4g_{i2}^3 g_{i3} \ \cdots \ 24g_{i1} g_{i2} g_{i3} g_{i4}]. \quad (8)$$

Applying least squares fitting, the tensor components are estimated.

Now, we have a  $D_{4 \times 4 \times 4 \times 4}$  tensor, which models the vessel in 4D. After going one high up in dimensions, in order to come back to the vessel physical space, we decompose the tensor to find its principal directions using a Higher Order Tensor Decomposition method [20]. We utilize one of the higher-order extensions of the matrix singular value decomposition: Tucker decomposition that computes the orthonormal spaces associated with the different axes (or modes) of a tensor [21]. The Tucker decomposition of an  $M \times N \times P \times Q$  (for our case,  $M = N = P = Q = 4$ ) tensor  $\mathbf{D}$  of order 4 is given by:

$$\mathbf{D} = \sum_{I=1}^M \sum_{J=1}^N \sum_{K=1}^P \sum_{L=1}^Q \mathbf{A}_{IJKL} \mathbf{U}_{iI} \otimes \mathbf{V}_{jJ} \otimes \mathbf{W}_{kK} \otimes \mathbf{Z}_{lL}, \quad (9)$$

where  $\otimes$  denotes the tensor (or outer) product:  $\mathbf{x} \otimes \mathbf{y} \triangleq \mathbf{x} \mathbf{y}^T$ . The matrices  $\mathbf{U}$ ,  $\mathbf{V}$ ,  $\mathbf{W}$ , and  $\mathbf{Z}$  are orthogonal;  $\mathbf{U}$  keeps the modes of the tensor, and  $\mathbf{A}$  keeps the eigenvalues. Matrix slices of  $\mathbf{A}$  along any mode are chosen to be mutually orthogonal with a decreasing Frobenius norm. In this case, the Tucker decomposition is called the Higher Order Singular Value Decomposition (HOSVD), which can be viewed as a generalization of the classical SVD for tensors.

### 2.4 Implementation Details

The algorithm starts from a user selected seed point preferably chosen from high contrast regions over a vessel. For the specific application of coronary arteries, to cover the typical radius range, values are selected from  $r_{min} = 0.25mm$  to  $r_{max} = 5.0mm$  with a fixed step of  $0.25mm$  in radius estimation as in [11]. 64 unit directions on  $\mathbb{S}^2$  are used in tensor fitting. To estimate the number of branches at a centerline point, we calculate the eigenvalues of the matrix  $\mathbf{A}$  in (9). The ratio of the eigenvalues to the largest eigenvalue is monitored, and a threshold

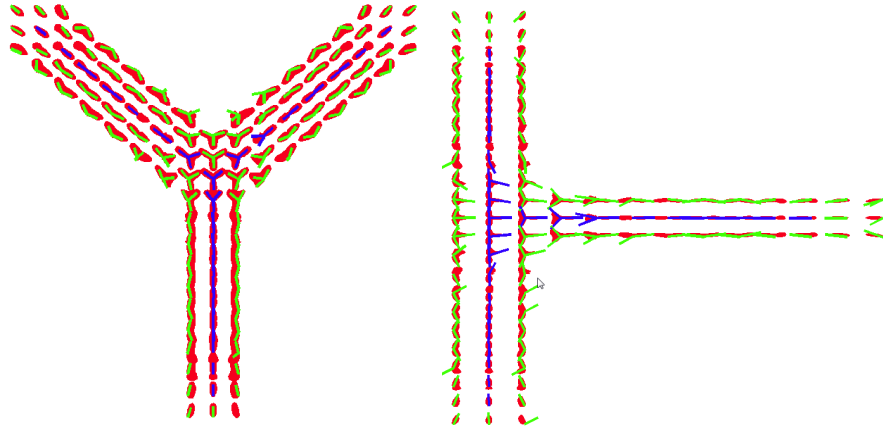


Fig. 3: Estimated modes (green) of the higher order tensors (red) are shown on synthetic Y-junction and T-junction volumes. Modes of the tensors along the centerline are depicted by blue.

value of 0.7 is selected in this work to determine the number of vessel orientations. To detect the vessel centerline directions, we extract the orientation vectors from corresponding columns of  $\mathbf{U}$ . Using those, HOT tractography technique is utilized to trace the vessel centerline [22]. Fig.3 depicts the detected eigen directions (green) of the higher order tensors (red) on synthetic Y and T junction volumes. Modes of the tensors along the centerline are depicted by blue. Although the tensors become perturbed along the edges, they correctly represent the expected geometry along the centerline of the vessel.

### 3 Results

We first evaluate our method on synthetic vascular images with known ground truth. The synthetic data simulate volumetric images of vascular trees with varying contrast [23]. Dice overlap (OM) is computed to evaluate the performance. Fig. 4(a) depicts a sample vascular synthetic volume. After selecting a single seed on one of the branches, our algorithm extracts the entire tree automatically. Extracted vessel tree with its thickness is also rendered on the right (green surface). On average, 95% OM ratio is obtained over five synthetic vasculature.

We performed quantitative validation on the database provided as part of the Rotterdam Coronary Artery Algorithm Evaluation Framework [24]. This facilitates standardized evaluations of centerline extraction methods over the same datasets with ground truth and with standard performance measures. So far, the results of 24 methods are evaluated in this framework. The proposed method was applied to all 32 datasets (including the 8 training and 24 testing data sets), and the results were evaluated by organizers. We ranked the first in the semi-automatic algorithms Category #2, in general, our average ranking is 10.20th (See Table 1). In fact our algorithm is nearly automatic: we selected only a single seed for each tree. The two automatic algorithms just above ours have the rankings 10.09 and 10.13. We rank the first among Category #1 (automatic) and #2

(semi-automatic) in the Overlap (OV) measure by 97.3% overlap<sup>1</sup>. Fig. 4 depicts a sample result from Rotterdam training database. Violet represents the reference centerline and radius that surrounds centerline. Our result is shown by orange; it takes less than 30 seconds to create the whole vessel tree in these experiments.

Table 1: Summary of Rotterdam Results

Measure	% / mm			score			rank		
	min.	max.	avg.	min.	max.	avg.	min.	max.	avg.
OV	81.8%	100.0%	97.3%	41.4	100.0	72.9	1	20	5.68
OF	7.1%	100.0%	77.4%	4.9	100.0	63.2	1	22	7.06
OT	83.0%	100.0%	97.7%	44.8	100.0	75.4	1	18	5.30
AI	0.15 mm	0.55 mm	0.34 mm	18.3	59.3	32.0	4	23	14.40
<b>Total</b>							<b>1</b>	<b>23</b>	<b>10.20</b>

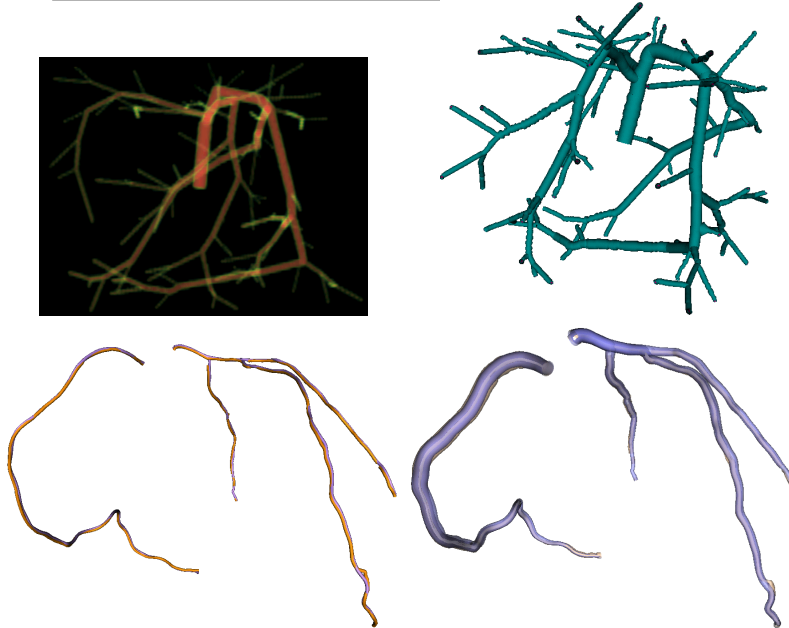


Fig. 4: Top Left-Top Right-Bottom Left-Bottom Right: (a) Synthetic vascular data with varying contrast; (b) Extracted vessel tree from synthetic data; (c) Extracted centerline (orange) and reference centerline (violet) from dataset 6 of Rotterdam database; (d) Extracted radius (orange) and reference radius (violet) is shown around centerline.

## 4 Conclusions

We presented a new method for extracting a whole vessel tree using an HOT flux-based tractography idea, which was inspired by HARDI techniques. One advantage of the proposed method is the seamless modeling of the n-furcations jointly with tubular sections within the same mathematical model. We achieved this by embedding a general cartesian tensor into a 4D space so that antipodal asymmetries in Y-junction-like situations, which are abundant in vascular trees, could be modelled. Although in this paper, we showed the results with a 4th order tensor, a 3rd order tensor is equally able to model a vessel tree with bifurcations only. Once an HOT is estimated, projecting the constructed tensor using an HOSVD, the main orientations of the vessel tree at a centerline point

<sup>1</sup> Please check the url to see our results at: <http://coronary.bigr.nl/preview/R68TKM>

are naturally extracted and traced. The radius of the vessel is also estimated by using a simple maximum norm criterion of a rank-2 tensor fit over a range of radii. We demonstrated the performance of the method by quantitative analysis of synthetic volumes and Rotterdam Coronary Artery Evaluation Framework. Our future work includes working on more complex vasculature with n-furcations.

## References

1. Frangi, R., et al.: Multiscale vessel enhancement filtering. MICCAI (1998) 130–137
2. Krissian, K.: Flux-based anisotropic diffusion applied to enhancement of 3-d angiogram. IEEE TMI **21**(11) (2002) 1440–1442
3. Lesage, D., et al.: Bayesian maximal paths for coronary artery segmentation from 3d CT angiograms. MICCAI (2009) 222–229
4. Friman, O., et al.: Multiple hypothesis template tracking of small 3D vessel structures. MIA **14**(2) (2010) 160–171
5. Zheng, Y., et al.: Robust and accurate coronary artery centerline extraction in CTA by combining model-driven and data-driven approaches. In: MICCAI. (2013) 74–81
6. Kirbas, C., et al.: A review of vessel extraction techniques and algorithms. ACM Comput. Surv. **36** (June 2004) 81–121
7. Lesage, D., et al.: A review of 3D vessel lumen segmentation techniques. MIA **13**(6) (2009) 819–845
8. Deschamps, T., et al.: Fast extraction of minimal paths in 3d images and applications to virtual endoscopy. MIA **5**(4) (2001) 281 – 299
9. Cohen, L., et al.: Global minimum for active contour models: A minimal path approach. International Journal of Computer Vision **24** (1997) 57–78
10. Li, H., et al.: Vessels as 4-d curves: Global minimal 4-d paths to extract 3-d tubular surfaces and centerlines. IEEE TMI **26**(9) (2007) 1213–1223
11. Cetin, S., et al.: Vessel tractography using an intensity based tensor model with branch detection. IEEE TMI **32**(2) (2013) 348–363
12. Yuan, F., et al.: Modeling n-furcated liver vessels from a 3d segmented volume using hole-making and subdivision methods. IEEE Trans Biomed Eng. **59** (2012) 552–561
13. Bogunovic, H., et al.: Anatomical labeling of the circle of willis using maximum a posteriori probability estimation. IEEE TMI **32**(9) (2013) 1587–99
14. Tuch, D.S., et al.: High Angular Resolution Diffusion Imaging of the Human Brain. In: The International Society for Magnetic Resonance in Medicine. (1999)
15. Ozarslan, E., et al.: Generalized diffusion tensor imaging and analytical relationships between diffusion tensor imaging and hardi. Magn Reson Med **50**(5) (2003) 955–965
16. Barmpoutis, A., et al.: Symmetric positive 4th order tensors & their estimation from dw-mri. In: IPMI. (2007) 308–19
17. Tuch, D.: Q-ball imaging. Magn. Reson. Med. **52**(6) (2004) 1358–72
18. Barmpoutis, A., et al.: Extracting tractosemas from a displacement probability field for tractography in dw-mri. In: MICCAI. (2008) 9–16
19. Tristan-Vega, A., et al.: Estimation of fiber orientation probability density functions in high angular resolution diffusion imaging. Neuroimage **47**(2) (2009) 638–50
20. Kolda, T.: Tensor decompositions and applications. SIAM Review **51** (2009) 455–00
21. Bergqvist, G., et al.: The higher-order singular value decomposition theory and an application. IEEE signal processing magazine **27**(3) (2010) 151–154
22. Descoteaux, M., et al.: Deterministic and Probabilistic Tractography Based on Complex Fibre Orientation Distributions. IEEE TMI **28**(2) (2009) 269–286
23. Hamarneh, G., et al.: Vascusynth: Simulating vascular trees for generating volumetric image data with ground-truth segmentation. CMIG **34**(8) (2010) 605–16
24. Schaap, M., et al.: Standardized evaluation methodology and reference database for evaluating coronary artery centerline extraction algorithms. MIA **13** (2009) 701–714

This proceedings has been generated to reflect the original papers accepted to the workshop CVII-STENT arranged together with the conference MICCAI 2014.